Flows through s-shaped annular, inter-turbine diffusers

Glyn Norris

Flows Through S-Shaped Annular, Inter-Turbine Diffusers

by

Glyn Norris

A Thesis submitted for the degree of

Doctor of Philosophy

School of Engineering

University of Durham

1997

Declaration

The work contained in this thesis has not been submitted elsewhere for any other degree or qualification and unless otherwise referenced it is the author's own work.

Acknowledgements

I am most grateful to my supervisor Dr. Robert Dominy whose guidance, support and encouragement have been invaluable throughout this project.

I would also like to thank the various members of staff within the School of Engineering who have provided me with assistance during my period as a research student. In particular thanks must go to Mr. Ray Mand, Mr. Brian Blackburn, Mr. Ian Glassford, Mr. Roger Little and not forgetting the late Mr. Mick Page.

Thanks must be extended to the School of Engineering and Rolls-Royce Plc whose financial support is gratefully acknowledged. The help of Mr. Andrew Smith and other members of Rolls-Royce Plc in their assistance of running the various CFD software is also much appreciated.

Finally I should like to recognise the numerous contributions of my fellow research students whose skills, expertise and support have at times been called upon.

This thesis is dedicated to my
grandfather Percy Teversham and to
lab technician Mick Page

Flows through S-Shaped Annular, Inter-Turbine Diffusers

Glyn Norris

Abstract

Inter-turbine diffusers or swan neck ducts (SND's) provide flow continuity between the H.P. and L.P. turbine, which with diffusing of the flow allow greater stage efficiencies to be achieved as a consequence of reducing both the stage loading and flow coefficient of the L.P. turbine.

This thesis presents an experimental and computational investigation into the local flow development and overall performance of two different severity diffusing annular s-shaped ducts, with the same overall diffusion ratio of 1.5, in order to validate the CFD code M.E.F.P.

The first less severe diffusing duct was used to investigate the effects of inlet swirl on the duct performance. It was found that at an optimum swirl angle of 15 degrees, the duct total pressure loss coefficient was approximately half the value at 0 or 30 degrees swirl.

The second more severely diffusing duct had simple symmetrical aerofoil struts added, which simulated struts required in real inter-turbine diffusers to support inner shafts and supply vital engine services. The total pressure loss developed by the 30% shorter duct was 15% greater that of the longer duct, and when struts were added to the second duct the loss almost doubled. These increases were attributed to gradually worsening casing surface flow separations which also acted to reduce the overall static pressure recovery of the ducts as their losses increased.

The computational investigations were made on the more severe duct with and without struts. The code, Moore's Elliptic Flow Solver (M.E.F.P) which used a mixing length model, predicted flow separation in the strutted duct case albeit in slightly the wrong position, however, it failed to predict any secondary flow for the unstrutted case and hence correlated worse with the measured results. This was also true of the results predicted by a version of Dawes BTOB3D.

List of Contents

List of Figures

List of Tables

Nomenclature

a	Perforated plate hole pitch
A	Area
b	Perforated plate web diameter
c	Perforated plate hole diameter
Cax	Strut axial chord
Cp	Coefficient of static pressure
Cpo	Coefficient of total pressure
d	Cylinder diameter
f	Frequency
h	Inlet passage height
H	Specific enthalpy
H	Boundary layer shape factor (δ^*/θ)
H.P.	High pressure
IGV	Inlet guide vane (swirl vane)
I.P.	Intermediate pressure
L.P.	Low pressure
m	Mass flow
OGV	Outlet guide vane
p	Static pressure
Po	Stagnation/total pressure
r	Radius
R	Overall engine pressure ratio
R	Stage Reaction
Re.	Reynolds number
SND	Swan neck duct
Tu	Turbulence intensity
U	Blade speed
V	Velocity
Vj	Jet velocity relative to engine
Vo	Relative velocity of air entering the engine
Vw	Whirl velocity

x	Axial distance from datum
y	Perpendicular distance from surface
δ	Boundary layer thickness
δ^*	Displacement thickness
ε	Effectiveness
γ	Ratio of specific heats
η	Efficiency
φ	Divergence angle
θ	Momentum Thickness
ρ	Density
ω	Rotational Speed

Suffixes

a	Axial
e	Exit
i	Inlet
l	Local

Chapter 1

Introduction

This thesis aims to investigate the flow through diffusing s-shaped annular ducts using experimental measurements taken on two different severity ducts. These experimental results, which are presented in chapter 4, are discussed in chapter 5 and are then used to validate the CFD predictions which are presented in chapter 6. The experimental results and CFD predictions are then compared in chapter 7. Chapter 8 proposes a new strut design (the struts are located within the s-shaped duct and provide inner shaft bearing support in a real engine) based upon CFD predictions. Chapter 9 concludes the main findings of the thesis and suggestions for future work follow in chapter 10. Chapter 2 defines the various terms used in the later chapters and reviews the previous research carried out in the field of diffusers. Chapter 3 describes the apparatus used to obtain the experimental results.
This chapter introduces the thesis by discussing the present and future requirements for inter-turbine diffusers.

Inter-turbine diffusers are used in gas turbines to provide flow continuity between either the high pressure (H.P.) or intermediate pressure (I.P.) turbine stages and the usually larger diameter low pressure (L.P.) stage. As the demand for higher thrust and lower specific fuel consumption continues to increase, the bypass ratio and hence engine diameters have also increased. This is because higher bypass ratio engines have a greater flow capacity which reduces the required exit velocity for a given thrust duty, and hence, greater propulsive efficiencies are achieved, (see equation 1.5 and explanation later). The turbine provides the power necessary to drive the compressor stages plus any engine ancillaries such as pumps, alternators, etc., and depending on the type of gas turbine, e.g. turboprop, turbofan, turbojet, it will usually provide extra shaft power or indirect thrust. In the drive for increased thermal efficiency, the pressure ratio of gas turbines have correspondingly increased as can be shown by equations 1.1 to 1.4 and refering to the Joule cycle T-s diagram shown in figure 1.1.

$$\eta_{thermal} = \text{Useful 'work' / Heat Input} \qquad \{1.1\}$$

$$\text{Useful 'work'} = Cp.(T_3-T_2)\left(1-\frac{T_1}{T_2}\right) \qquad \{1.2\}$$

$$\text{Heat Input} = Cp.(T_3 - T_2) \qquad \{1.3\}$$

where T_1 is the temperature before compression, T_2 the temperature after compression and T_3 the temperature after heat energy is added. Substituting 1.2 and 1.3 into 1.1, it can be shown that:

$$\eta_{thermal} = 1 - \left[\frac{1}{R^{\left(\frac{\gamma-1}{\gamma}\right)}} \right] \qquad \{1.4\}$$

where R = engine pressure ratio

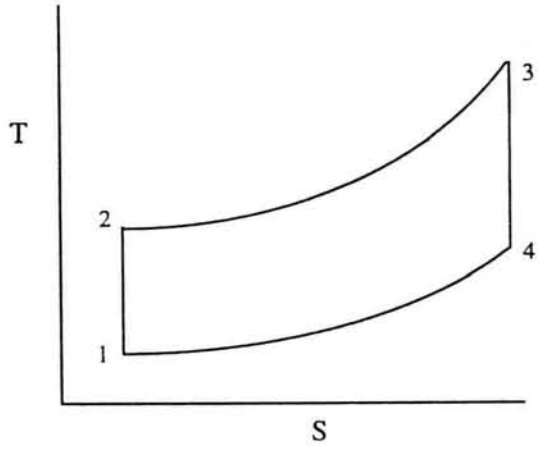

Figure 1.1 - Joule Cycle T-s Diagram

Increasing the compressor pressure ratio on a single shaft beyond about 8:1 causes the front stages of the compressor to run into what is known as 'stall' since the value of Va/U or angle of attack differs for these stages. Va is the axial velocity of the flow and U is the blade speed. Conversely, the rear stages start to choke as they are caused to run far from their optimum design point. Compressor stall should be avoided at all costs since this flow phenomena can be extremely destructive and hence dangerous and therefore some form of surge alleviation is necessary. The three main forms of surge alleviation used are:

- Compressor bleeds
- Variable inlet guide vanes and variable compressor stators

- Multiple shafting

Any one or more of these three methods have been employed on gas turbines past and present. Multiple shafting progressed from single to double spool as pressure ratios increased, to the present day where triple spool machines with pressure ratios of 34:1 have been reached in production engines, e.g. RB211-524L. Each shaft employs a number of compressor stages and usually a fan, driven directly by its corresponding turbine stages, hence the compressor and turbine stages on each shaft have the same rotational speed. Each shaft is mechanically independent of the other one or two (neglecting bearing friction due to them being concentric), and therefore allows each shaft to rotate at its optimum rotational speed.

The H.P. turbine is subjected to extreme conditions including peak gas temperatures of 1700 °C and local gas velocities of up to 750 m/s. For peak efficiency the turbine blade tip speeds may be in excess of 450 m/s. In order to produce the immense power absorbed by the compressor (30 MW, ~ 40,000 horse power in the case of the Rolls Royce RB211 fan), the turbine may require more than one stage consisting of stationary stator rows alternating with moving turbine rows. The number of turbine stages will depend upon its rotational speed (governed by the compressor it is driving), the turbine diameter and its duty.

Smith's [Smith (1966)] empirical correlation (figure 1.2) shows that a higher turbine stage efficiency is obtained by having a low stage loading coefficient ($\Delta H/U^2 = \Delta Vw/U = \Delta Vw/\omega r$), and to a lesser degree, a low flow coefficient (Va/U); where ΔH is the specific enthalpy, U the blade speed, ω the rotational speed, r the radius and ΔVw is the change in whirl velocity (see figure 1.3). Smith's correlation incorporates the results of 69 cold flow tests of model turbines with up to 4 stages. He plotted the results of these 69 tests onto a graph of stage loading coefficient vs flow coefficient and drew lines through points of equal efficiency. Smith's charts have proved very useful in turbine design and in general, compressor turbines are generally designed to efficiencies greater than 90%. The best turbines are designed in the following ranges.

$$1.0 < (\Delta H/U^2)\text{mean} < 2.5$$

$$0.6 < (Va/U)\text{mean} < 0.8$$

Although the best efficiency can be obtained from having $\Delta H/U^2 = 1$ and $Va/U = 0.6$, this would give a turbine which produced low power since $\Delta Vw = U$, and hence one is generally compelled to higher power output and therefore lower efficiency. The line of best efficiency therefore has the equation shown by 1.5.

$$\left(\frac{\Delta H}{U^2}\right)_{\eta_{best}} = 6.7\left(\frac{Va}{U}\right) - 2.9 \qquad \{1.5\}$$

Both $\Delta H/U^2$ and Va/U can be reduced in magnitude by increasing blade speed U, but the turbines rotational speed ω is fixed by the compressor rotational speed which in turn is governed by the maximum compressor blade tip speed. This is usually designed for a maximum relative blade tip Mach. No. of 1.15 to avoid unacceptable shock losses. The rotational speed is also constrained by turbine disc stress which is proportional to rotational speed squared and therefore the disc thickens and becomes disproportionately heavier as r.p.m. increases.

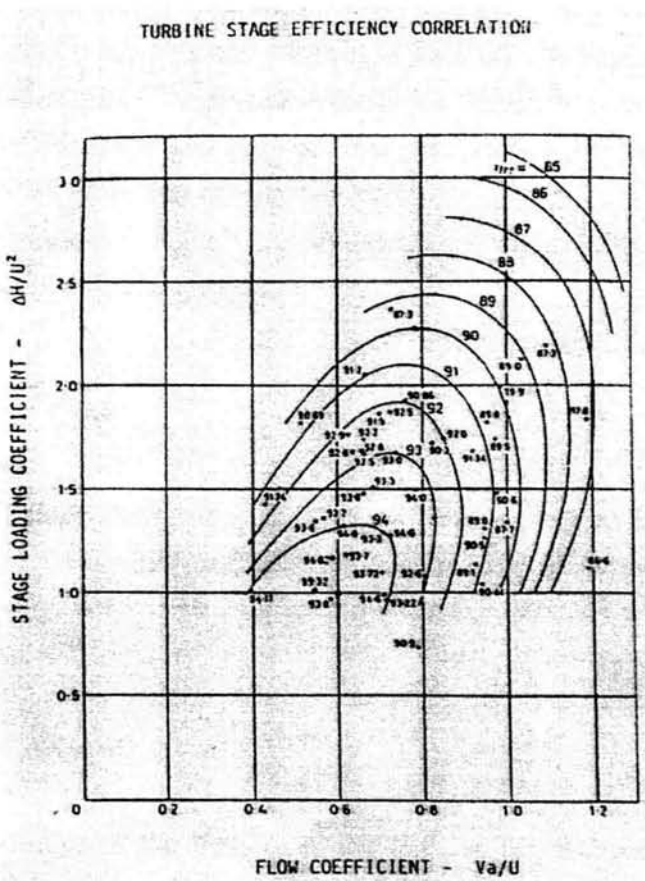

Figure 1.2 - Smith's Correlation for Turbine Stage Efficiency [Smith (1966)]

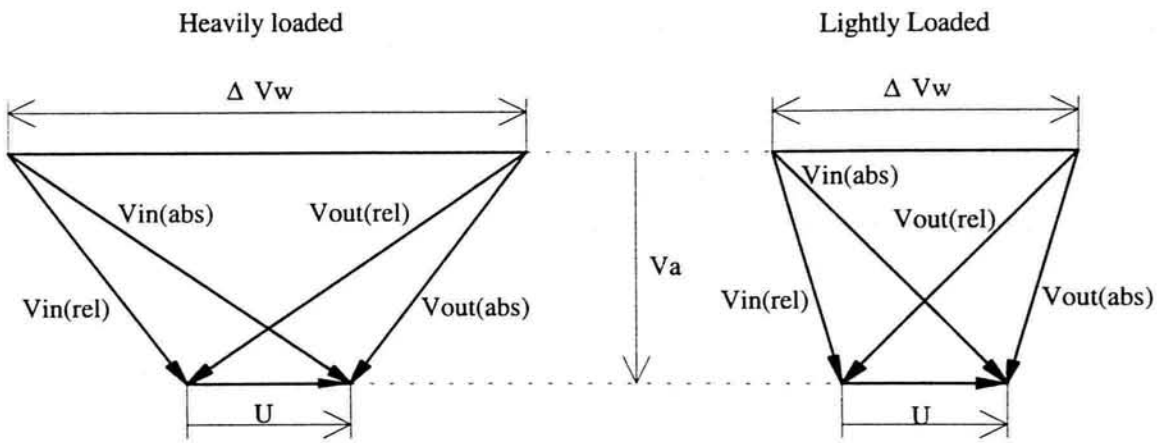

Figure 1.3 - Turbine Velocity Triangles

An alternative way of increasing stage efficiency is to reduce the amount of turning achieved by each blade row (ΔVw), however, since the duty on each shaft is set by the compressor it is driving plus the residual power needed for thrust, this would increase the number of stages required and therefore incur weight penalties. Figure 1.3 shows the velocity triangles for an highly loaded H.P. turbine blade row and a lightly loaded L.P. turbine blade row. Note, they both have the same blade speed U and axial velocity Va. Vin(abs) is the absolute velocity of the gas entering the turbine rotor and (rel) denotes the gas velocity relative to the moving blade. Vout is the velocity of the gas exiting the rotor.
Note, the velocity triangles in figure 1.3 are symmetrical, making them 50% reaction turbines. Stage reaction is defined by equation 1.6

$$R = \frac{\Delta H_{rotor}}{\Delta H_{stage}} \qquad \{1.6\}$$

The only remaining independent variable is the turbine radius r. Increasing r not only reduces the stage loading and flow coefficients by increasing blade speed U which in turn increases stage efficiency, but it also increases the 'power per unit mass flow' or 'specific enthalpy' (ΔH), equation 1.7.

$$\Delta H = \omega.r.\Delta Vw \qquad \{1.7\}$$

In addition to these benefits, if the flow from the H.P. or I.P. turbine is diffused before it enters the L.P. turbine, a corresponding rise in static pressure and fall in axial velocity (Va)

occur, which will further contribute to reducing the flow coefficient (Va/U) and hence increase turbine stage efficiency.

Although swan neck ducts are often used as inter-compressor ducts, in order to connect the larger radius L.P. or I.P. compressor to the smaller radius H.P. compressor where the area is reducing, they are rarely seen in the form of inter-turbine diffusers for a number of reasons. Firstly, it is clear that the flow behaviour in a contracting duct (compressor stage) is likely to be more predictable than a flow in a diffusing swan neck duct, where the pressure gradient is generally adverse and hence flow separation is more likely to occur.

Secondly the overall length and weight of the engine tends to increase if swan neck ducts are employed, and it may also require extra bearings to support the longer shafts. These reasons plus a lack of knowledge and experience of SND's employed as inter-turbine diffusers, together, may explain their rarity.
However, figure 1.4 shows an example of a SND currently used as an inter-turbine diffuser in General Electric's CF6-50 range of engines. The swan neck duct is situated between the high pressure and low pressure turbine. Note that this engine is of a two shaft design and consequently employs six rows of variable stators in the fourteen stage H.P. compressor to alleviate surge; it's driven by a two stage H.P. turbine.
The four stage L.P. turbine is required to drive the three 'core booster' stages and the fan which itself may contribute up to 80% of the engine's total thrust. The engine also employs a swan neck duct in between the L.P. and H.P. compressors.

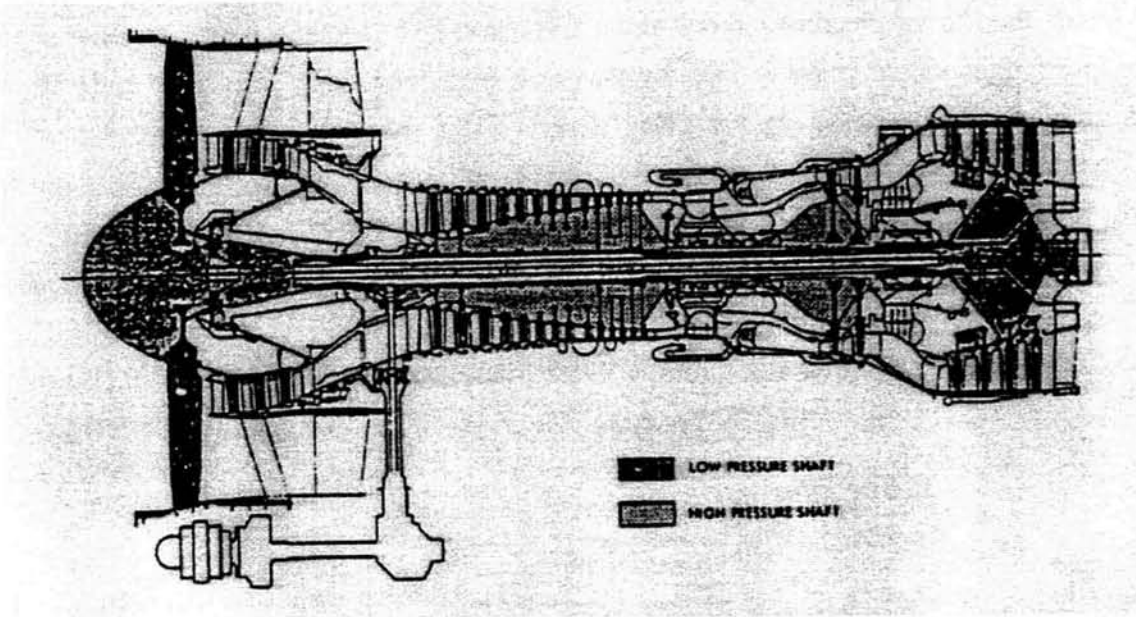

Figure 1.4 - General Electric CF6-50 [C.I.T. (1993)]

Rolls Royce on the other hand, have adopted the triple spool strategy which requires fewer compressor and turbine stages and hence produce an overall shorter engine. This may be seen in figure 1.5 which compares two equivalent engines, the Rolls Royce Trent 800 and General Electric's GE90.

The general move to using larger diameter and hence higher bypass ratio turbofans, whos' requirement for SNDs is greatest, is driven by a number of factors. Market forces constantly demand engines with greater thrust and efficiency (lower s.f.c.), in order to power the next generation of 'super' carrying aircraft such as the Boeing 777.

Controls on pollutant emissions such as unburned hydrocarbons, carbon monoxide, nitrogen oxide and smoke have tightened recently as concerns for the environment have been raised. High bypass turbofans by their nature only burn a fraction of the air consumed for thrust and along with new combustor technology, together, make these new engines more environmentally friendly.

Noise pollution in areas surrounding airports is another important factor since the population of these areas is increasing, whilst new runways are being planned and built near these areas

to cope with increased demand. The perceived noise levels produced by aircraft mainly at take off when their load, thrust and hence noise are greatest, is being increasingly monitored and the allowable levels reduced. High bypass turbofans go some way to helping this problem since noise is proportional to (velocity)^a, where a≈7. Therefore the higher the bypass ratio, the lower is the mean exit velocity and hence noise produced, for a given thrust.

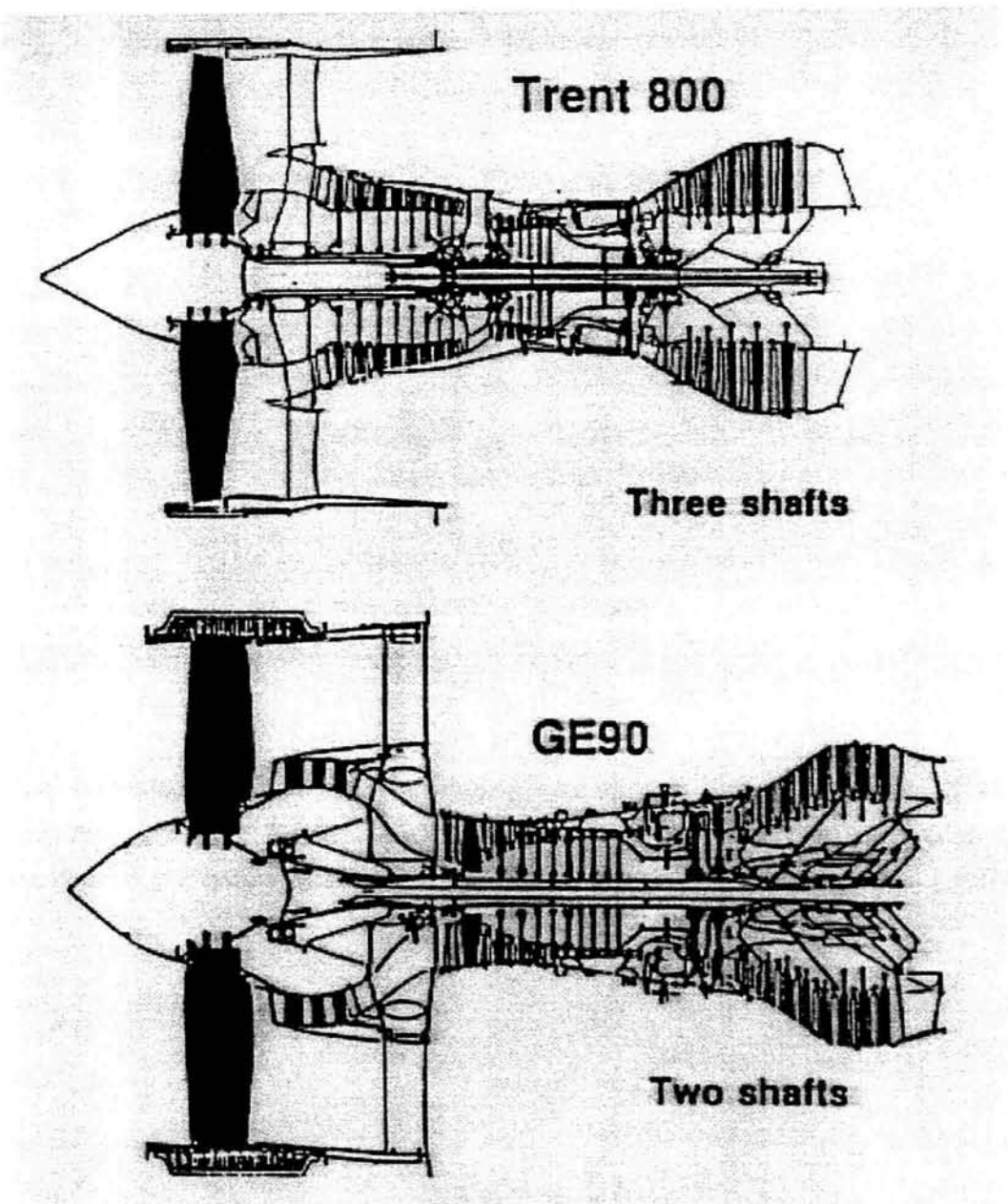

Figure 1.5 - The Rolls Royce Trent 800 and General Electric GE90

Another advantage of the high bypass turbofan compared to an equivalent turbojet is its higher propulsive efficiency. Equation 1.8 defines the basic equation for propulsive efficiency and equation 1.9 can then be simplified to equation 1.10. Equation 1.10 shows that as bypass ratio increases, exhaust jet velocity (V_j) decreases and therefore propulsive efficiency increases.

$\eta_{propulsive}$ = thrust power / (thrust power + jet kinetic power) {1.8}

$$\eta_{propulsive} = \frac{(V_j - V_o)V_o}{(V_j - V_o)V_o + \frac{1}{2}(V_j - V_o)^2} \quad \{1.9\}$$

$$\eta_{propulsive} = \left[\frac{2}{1 + \frac{V_j}{V_o}}\right] \quad \{1.10\}$$

where V_j = exhaust jet velocity relative to the engine
V_o = Forward flight velocity

Figure 1.6 shows schematically that turbofans have slightly higher propulsive efficiencies than equivalent turbojets for the Mach numbers at which aircraft utilising high bypass turbofans operate, i.e. below Mach 1.

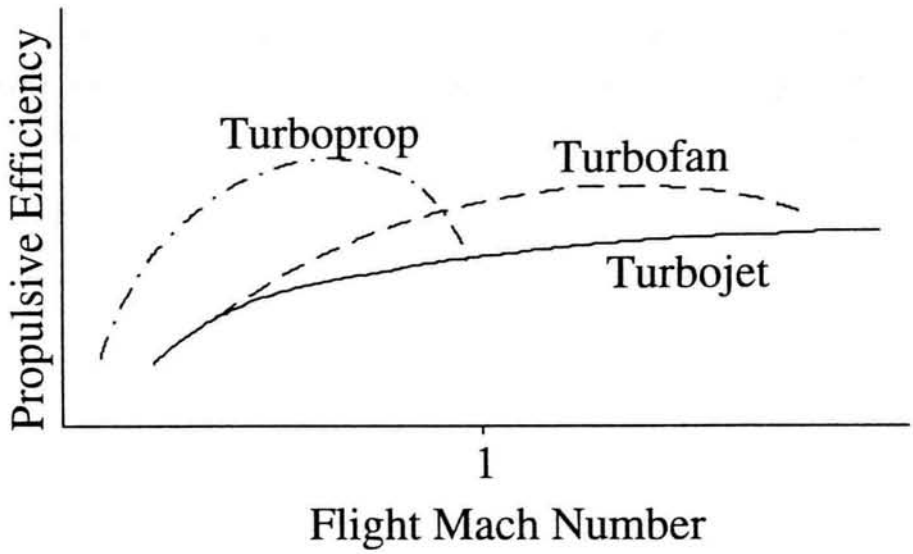

Figure 1.6 - Schematic of Propulsive Efficiency vs Flight Mach Number [C.I.T. (1993)]

As mentioned earlier, SNDs in the form of inter-turbine diffusers are not a common feature in gas turbines and instead, 'hade' is usually used. Hade is where an angle exists between the annulus walls of the turbine passage and the axial flow direction. In a gas turbine this usually implies an increasing casing diameter and a hub diameter which may either rise, remain constant or fall, but always has the overall effect of increasing the annulus area. This produces an H.P. or I.P. turbine who's mean exit radius is similar to that of the L.P.'s mean inlet radius. This is shown in diagrammatic form in figure 1.7.

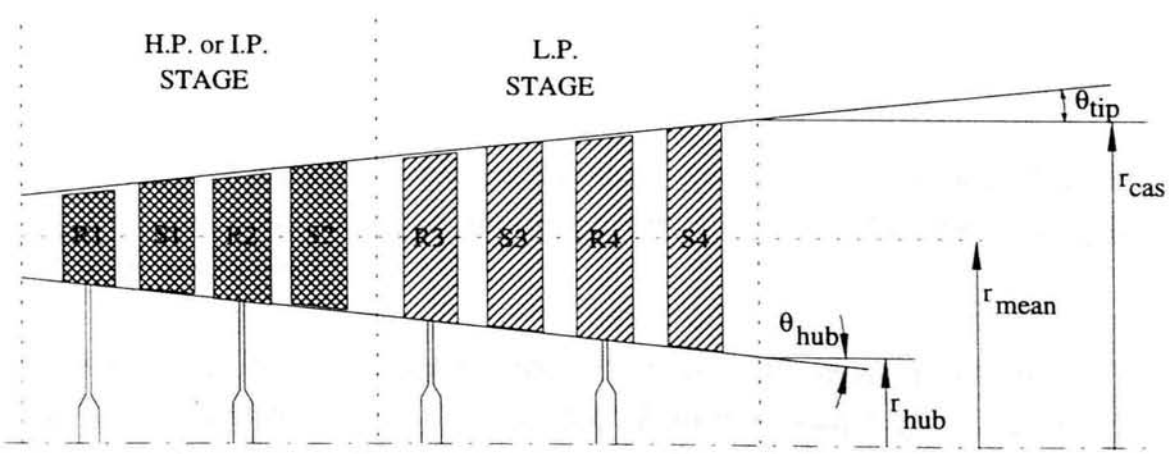

Figure 1.7 - A Haded Turbine Passage

A good example of hade is illustrated in the L.P. turbine stages of the Trent 800 shown in figure 1.4. Note how the hub diameter remains constant but the casing diameter increases, and hence both the mean radius and area are increasing, which go some way to achieving the objectives of a SND.

Hade is also shown in figure 1.4 in the General Electric CF6-50 L.P. turbine. However, in this example, increasing area is achieved by decreasing the hub diameter and keeping the casing diameter constant, i.e. mean radius decreasing.

Although hading avoids the need for an additional inter-turbine diffuser and has the advantage of relatively simple geometry, it compromises the rotational speeds of the separate shafts and therefore does not allow the full benefits of a high speed low diameter shaft and low speed high diameter shaft to be achieved.
With reference to figure 1.7 and [C.I.T. (1993)], the general guidelines for hade are:

$$\theta_{tip} < 25°$$

$$\theta_{hub} < 20°$$

and included angle $\theta_h < 35°$

In order to maximise these benefits, there is a need to achieve most of the diffusion between turbine stages rather than through them.

In Summary:

- The drive for cleaner, quieter gas turbines with greater thrust and efficiency has continued to result in higher and higher bypass ratio turbofans being designed and brought into service.

- The higher the bypass ratio and hence fan diameter, the greater is the requirement for swan neck ducts in the form of inter-turbine diffusers in order to provide flow continuity between the H.P. and I.P. or L.P. turbines of substantially different diameter and to increase turbine stage efficiency.

Chapter 2

Overview of Diffuser Flows

2.1 Introduction

The definition of a diffuser is a duct along which the mean static pressure of a flowing fluid increases as a result of decreasing kinetic energy of the flow *without* any external energy input, e.g. *without* the premature removal of potentially separating boundary layers or re-energisation of low energy boundary layers using external energy input. For sub-sonic flow this usually implies a duct with increasing area in the direction of flow, although an increase in static pressure can also be achieved in other duct geometries, such as parallel pipes, when a distorted velocity profile settles to a more uniform condition. There are many different types of ducts which satisfy the criterion of a diffuser. However, the specific application often dictates the particular type required. e.g. a gas turbine inter-turbine diffuser would probably be of the annular type because of the connecting centre shaft. The final design of an aero gas turbine diffuser will also depend upon factors such as the role of the aircraft. For example in the case of a pre-combustor dump diffuser in say a military interceptor aircraft where flying time is relatively short, factors such as efficiency and total pressure loss are outweighed by compactness and lightness. The same type of diffuser designed for use in a commercial long range aircraft where s.f.c. becomes the important parameter will be designed to minimise total pressure loss. Diffusers are not only used in aircraft applications and do not only use incompressible gases as their working fluids. For example hydraulic pumps use incompressible liquids such as water or oil and have diffusers called volutes to recover static pressure. Compressibility effects which are found in some applications, e.g. aircraft intakes (M>0.3) and centrifugal compressors, will act to increase the ideal static pressure recovery of a diffuser, since the reduction in density of the fluid beyond this Mach number starts to become significant. The Durham swan neck duct has flow Mach. numbers below 0.3 throughout and therefore assumes incompressible flow. This chapter firstly describes some of the basic types of diffusers used such as conical and annular. It then defines the various parameters and coefficients used to describe their performance before explaining how the static pressure can vary through a duct

depending on factors such as duct curvature and swirling flows. Finally it focuses on a review of work carried out specifically on curved walled annular diffusers.

2.2 Diffuser Types

Figure 2.1 shows 4 basic types of diffuser from which other special combinations such as the swan neck duct can be made. A review of simple primary flows in conical and annular diffusers are documented by Cockerell *et al* (1963) and ESDU (1976).

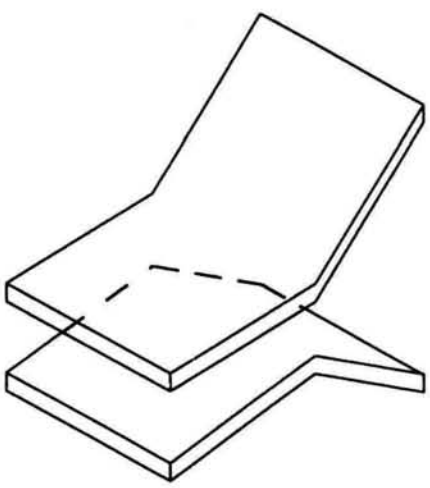

A) Straight Walled 2-D Diffuser

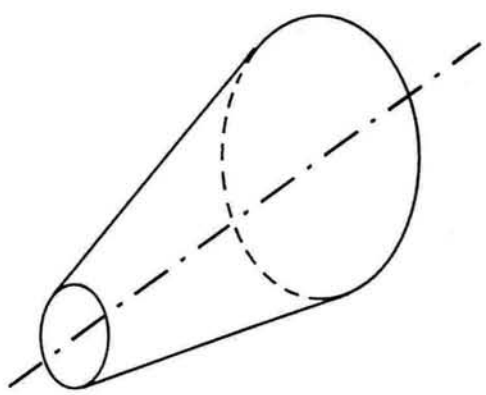

B) Straight Walled Conical Diffuser

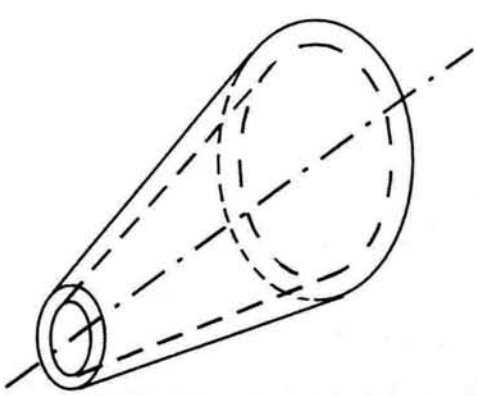

C) Straight Walled Annular Diffuser

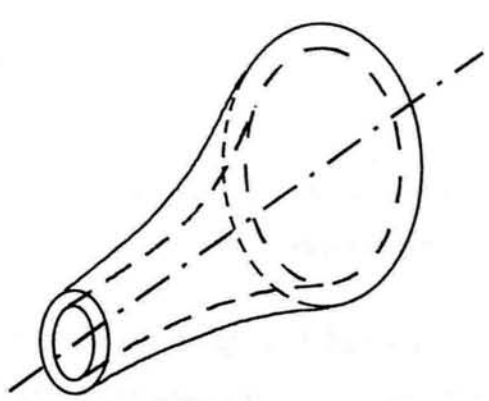

D) Curved Walled Annular Diffuser

Figure 2.1 - Basic Diffuser Geometries

2.3 Diffuser Performance Parameters

Diffuser performance is usually expressed in terms of the static pressure rise across the diffuser with, less often, information about the total pressure loss and outflow conditions.

This section defines some of the various parameters used and the reasons for them.

2.3.1 Static Pressure Rise Coefficient Cp

One definition traditionally used for the performance of both axisymmetric and non-axisymmetric diffusers is known as the 'coefficient of static pressure rise' (Cp) shown by equation 2.1. This term is frequently abbreviated to Δp/D, pronounced 'delta pee on dee' , the D referring to the initial or inlet dynamic head. This is a suitable term to non-dimensionalise by when quoting compressor or diffuser performance because the inlet dynamic head is usually larger than the exit, hence producing a larger number. Also the inlet conditions are likely to be more uniform than the exit, giving a more reliable reference value. Turbine Cp's are traditionally non-dimensionalised by exit dynamic head since here the flow has a larger exit velocity therefore giving a larger dynamic head.

The magnitude of Δp/D is a measure of the proportion of the inlet dynamic head, D, converted into pressure rise Δp.

$$Cp = \left[\frac{\overline{p}_e - \overline{p}_i}{\frac{1}{2}\rho\overline{v}_i^2}\right] = \left[\frac{\overline{p}_e - \overline{p}_i}{\overline{P}o_i - \overline{p}_i}\right] \qquad \{2.1\}$$

Suffix 'e' denotes the exit and 'i' the inlet planes respectively. For a local static pressure rise coefficient anywhere within the duct, simply replace the exit static pressure 'p_e' with the local value p_l.

Note. $\overline{p}$ and $\overline{v}$ refer to AREA averaged static pressure and velocity and therefore C_p is an AREA averaged static pressure coefficient. This means that it cannot be combined with equation 2.5 which is MASS averaged coefficient.

An alternative parameter used to measure diffusion is the velocity ratio itself, V_e/V_i. This is known as the 'de Haller Number' and is traditionally applied to non-axisymmetric diffusers only, for example turbomachinery components.

2.3.2 Ideal Static Pressure Rise Coefficient Cp_{ideal}

If the flow through a diffuser was frictionless and the inlet and exit flows completely uniform then the total pressure at inlet would equal that at exit. (Po_i=Po_e)
Applying the continuity equation 2.2 to equation 2.1 and assuming incompressible flow i.e. Mach No. ≤ 0.3 and therefore $\rho_i = \rho_e$, we can rearrange equation 2.1 to get 2.3 in which the static pressure recovery coefficient may be expressed purely in terms of area ratio. This equation is known as the *ideal* static pressure recovery, i.e. the maximum possible diffusion that could occur if the flow were diffused isentropically to the boundary conditions given.

$$\left(\rho_i \bar{v}_i A_i\right) = \left(\rho_e \bar{v}_e A_e\right) \qquad \{2.2\}$$

$$Cp_{Ideal} = 1 - \left(\frac{A_i}{A_e}\right)^2 \qquad \{2.3\}$$

Cp_{ideal} assumes no total pressure loss, i.e. Bernoulli applies, and is in affect an area averaged coefficient.

The value of Cp_{ideal} therefore follows a law of diminishing returns as the area ratio is increased, as shown graphically in figure 2.2.

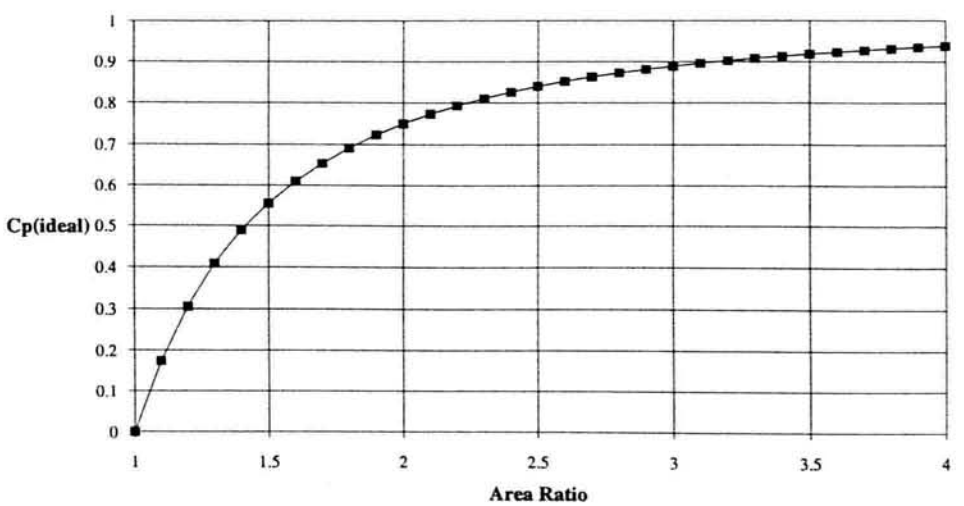

Figure 2.2 - Variation of Cp_{ideal} with Area Ratio

2.3.3 Diffuser Effectiveness ε

In practice factors such as wall friction, turbulence generation in the mainstream and flow separation in the most severe case, together mean that the ideal recovery will never be achieved. The ratio of actual static pressure coefficient obtained (Cp) to the *ideal* pressure rise coefficient (Cp_{ideal}) which could be achieved with the same inlet conditions and duct geometry given frictionless flow and uniform exit conditions is termed the effectiveness, ε, (equation 2.4).

$$\varepsilon = \frac{Cp}{Cp_{ideal}} \qquad \{2.4\}$$

A well designed, conventional diffuser (i.e. without boundary layer removal etc.) will typically recover 85% of the ideal Cp; external energy input such as premature boundary layer removal is necessary to achieve higher values.

2.3.4 Stagnation Pressure Loss Coefficient Cpo

The stagnation pressure loss coefficient is defined by equation 2.5.

$$Cp_0 = \frac{\overline{P}o_i - \overline{P}o_e}{\frac{1}{2}\rho\overline{v}_i^2} \qquad \{2.5\}$$

It is a measure of how much total pressure is lost as a proportion of the mean inlet dynamic head due to viscous forces and turbulent mixing. Typical values for aerodynamic diffusers are between 0.1 and 0.2. The mean total pressure is taken as the mass averaged value given by equation 2.6.

$$\overline{P}o = \frac{1}{m}\int_A Po.dm \qquad \{2.6\}$$

2.4 Static Pressure Distribution

The static pressure distribution through a duct depends on a number factors including the following.

- Diffusion due to area change along the duct axis
- Diffusion due to duct curvature along the duct axis
- Effective duct curvature due to boundary layers
- Boundary layer blockage
- Inlet swirl
- Turbulence
- Flow regime
- Reynolds Number
- Inlet flow conditions
- Mach number

These will be studied in turn.

2.4.1 Diffusion Due to Area Change Along the Duct Axis

Diffusion due to area change arises as a direct consequence of the continuity equation {2.2}. For an incompressible and ideal flow (inviscid) the diffusion or reduction in velocity is directly proportional to the area increase for a straight walled duct. Figure 2.3, which is for an ideal flow in a straight walled, conical diffuser, shows that a greater diffusion rate is achieved in the early part of the duct, where the flow has greatest velocity and hence dynamic head, which is transferred into static pressure. In order to attain a maximum overall recovery of 1, the figure shows that the area ratio needs to be infinitely large so that the exit velocity approaches zero. This is clearly not possible in practice and hence a measure of diffuser effectiveness, ε, defined in section 2.3.3 is often useful.

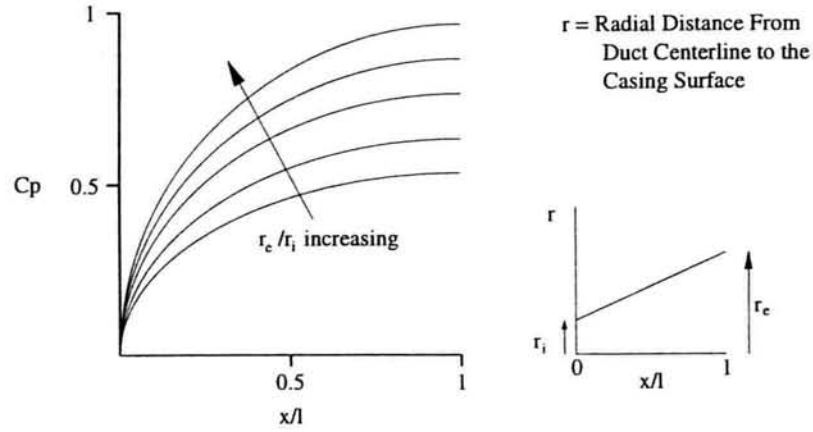

Figure 2.3 - Idealised Cp Curves for Straight Walled Diffusers

As in turbine design, much diffuser design is still based upon empirical correlations of experimental data. Data from many experiments on diffusers has been correlated in the form of diffuser charts, a typical one is shown in figure 2.4. In this chart, contours of Cp are plotted on a log area ratio verses log non-dimensional length. The chart shows that a particular value of static pressure coefficient, Cp, can be achieved from numerous combinations of area ratio and length, taken from the relevant isobaric contour. For conical diffusers the length is non-dimensionalised against inlet diameter but for annular diffusers either the inlet duct height, h, or mean hydraulic diameter, D_h, are used where the latter is defined by equation 2.7.

$$D_h = (4. \text{ cross sectional area }) / \text{ wetted perimeter} \qquad \{2.7\}$$

Two curves, important for design purposes, are also inserted. The Cp* curve running through the vertical tangents of the lines of constant Cp, indicates a family of diffusers optimised to produce the maximum pressure recovery within a given length. This curve is particularly important when designing for aeronautical applications where length and weight are paramount. This is particularly important for gas turbine engines where it is important to minimise shaft length to avoid shaft whirling.

The Cp* family of diffusers are characterised by the phenomena of transitory stall, which is described later in this chapter. This can however produce a certain level of pressure fluctuation from the intermittently separating boundary layer flow.

In general, it's advisable to design below the Cp* curve since designing above this line would lead to poor performance due to high levels of flow instability.

The second curve indicated by Cp**, signifies a family of diffusers optimised to produce the maximum pressure recovery within a limited area ratio. Their flow is characterised by it's smoothness and would be important for industrial gas turbines where weight and space are less important than flow stability. In practice these engines would compromise the design and their diffusers would be taken from the zone between the Cp* and Cp** lines.

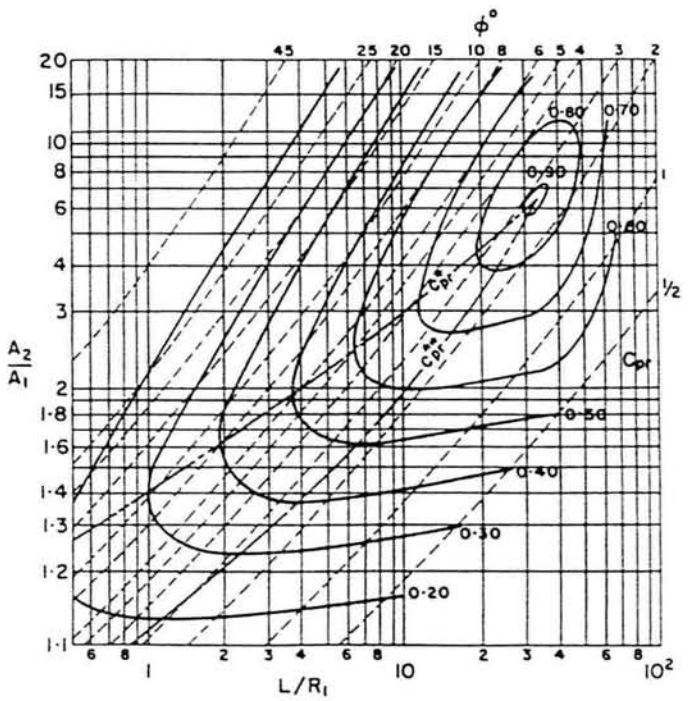

Figure 2.4 - Typical Diffuser Chart [ESDU, 1976]

2.4.2 Diffusion Due to Duct Curvature Along the Duct Axis

As a flow develops along the length of a curved wall diffuser it becomes more susceptible to flow separation due to thicker boundary layers if it encounters a radial or axial pressure gradient formed by streamline curvature. Streamline curvature occurs if the flow is forced to change its direction from the diffuser axis as in the case of a bend or curved wall. The flow on the convex curve accelerates therefore lowering the local static pressure and vice versa on the concave surface forming a pressure gradient.

Curving walls therefore alter the pressure gradient distribution and hence the boundary layer development. Figure 2.5 shows schematically the velocity development through a curved duct or bend. Initially the pressure gradient is favourable on the convex bend: it counteracts the 'slowing down' effect of the boundary on the fluid, i.e. the static pressure falls in the direction of flow. At the separation point the sign of pressure gradient changes and beyond this point the pressure gradient is said to be adverse, or opposing the flow direction. From this point onwards flow separation is likely.

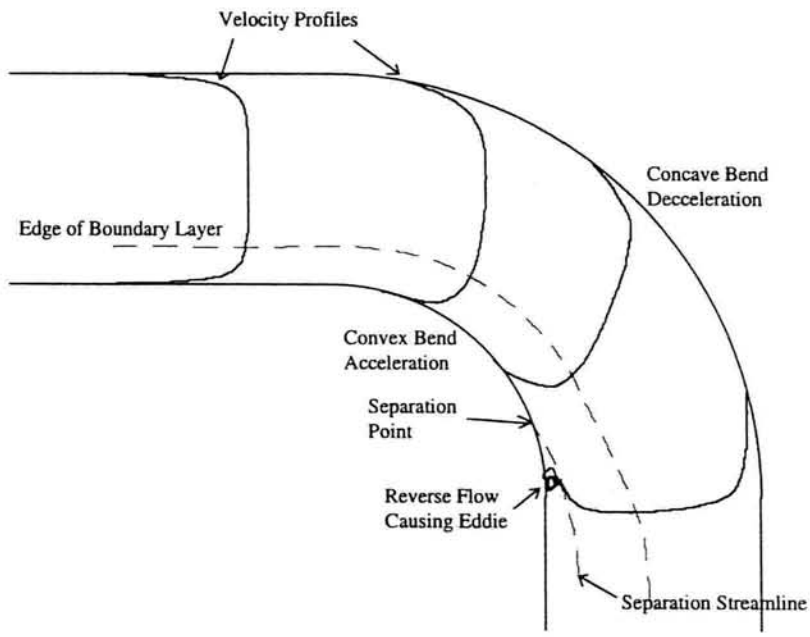

Figure 2.5 - Velocity Profiles on Curved Bends

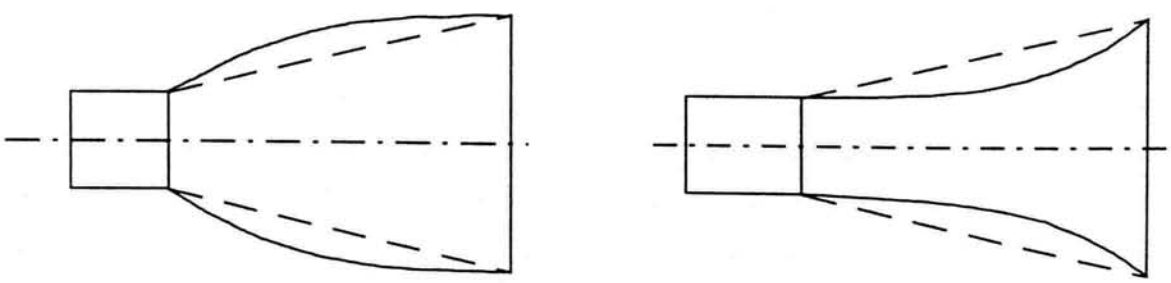

A) Bell-Shaped Diffuser

B) Trumpet-Shaped Diffuser

Figure 2.6 - Curved Walled Diffusers

Figure 2.6 shows two examples of simple curved walled diffusers. Figure 2.6a, the bell shaped diffuser, increases the axial pressure gradient near the entry point where the flow is able to resist a higher pressure gradient without separating because of thinner boundary layers. The axial pressure gradient is then decreased further along the duct to prevent or reduce separation where the boundary layers are likely to be thicker and more prone to separation. This type of diffuser is likely to give better performance than the equivalent straight walled diffuser if the former had flow separation present and the latter would operate with little or no separation.

Typically in the design of diffusers, Rolls-Royce impose a lower skin friction coefficient of 0.001, in order to avoid the risk of flow separation. However, numerical calculations on the severe phase 2 duct (see fig. 3.5) predict a minimum casing value of 0.0002 immediately after the first bend, Smith (1991). Other guidelines are also used in diffuser design such as area ratio. However on its own, this is not enough to ensure that the flow remains attached since other factors, e.g. wall profile, will also determine the duct performance.

The trumpet-shaped diffuser shown in figure 2.6b is designed to delay separation by reducing the pressure gradient in the early stage of the diffuser but the increase in wall curvature later in the diffuser may cause separation in this region. This makes this type of diffuser suitable for situations where the flow would separate early in an equivalent straight walled diffuser, for example in diffusers operating with inlet Mach numbers in excess of 0.6 where compressibility effects would cause an increased adverse pressure gradient and hence flow separation. Because of the initial slow area increase, the initial boundary layer growth may cause a reduction in effective area although a minimum wall angle of 2° to 3° with rounded entry corners avoids this problem, E.S.D.U. (1976). Gibson (1911) tested different trumpet wall shapes and found that the most effective was one giving potentially a linear increase in static pressure along the diffuser length. Gibson (1911) and Henderson (1959) showed that increases in overall static pressure recovery of 30% could be achieved when a trumpet shaped diffuser is substituted for a straight walled diffuser if the flow is either almost or fully separated.

A development from the basic trumpet shape diffuser which has problems of flow separation in the latter part where the wall angle becomes too great, is the inflected wall

diffuser shown in figure 2.7. When the wall angle becomes too great, Gibson (1911) suggests no more than 17° to 18°, the wall is turned back to an axial direction by means of a concave surface. This shape is basically the casing surface of the swan necked duct which is designed for near axial inlet and exit flows for optimum turbine conditions.

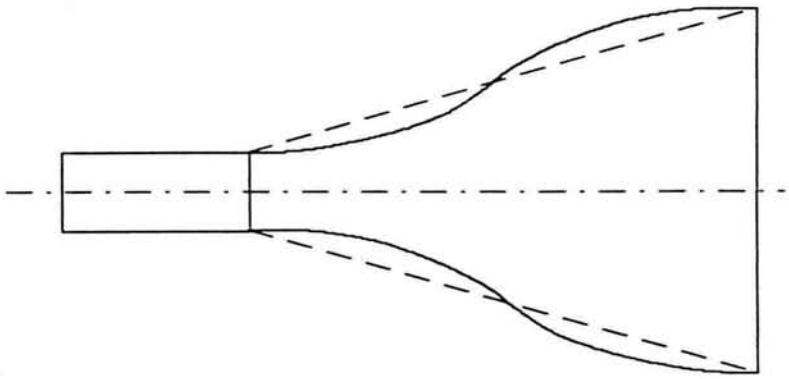

Figure 2.7 - Inflected Wall Diffuser

Another often effective means of recovering static pressure in diffusers which are either close to separation or fully separated and which have downstream passages is the dump diffuser. A sudden enlargement as shown in figure 2.8 (ABCD) can often improve the performance of a straight wall diffuser (AED) as long as a downstream section (tailpipe) is present, otherwise any potential pressure recovery due to the sudden enlargement is lost. The truncation or sudden enlargement stabilises the separation vortex which can also help guide the flow smoothly over a sudden step, Adkins (1983). An added advantage can often be an improvement in flow symmetry downstream of the diffuser since the separation is stabilised all round the diffuser at the truncation.

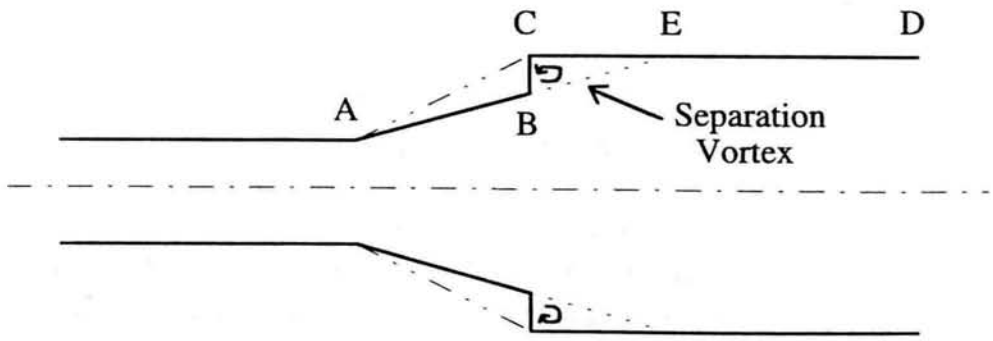

Figure 2.8 - Truncated Diffuser

2.4.3 Effective Duct Curvature due to Boundary Layers

The effective duct curvature on a curved surface differs from the geometric curvature of the duct due to the growth or thinning of boundary layers. Flow on a concave bend increases the boundary layer thickness and vise versa on a convex surface. The increased boundary layer thickness on a concave surface reduces the effective radius of curvature and hence the velocity is greater than if the flow were inviscid. On a convex surface, although the boundary layer thickness reduces as the flow accelerates, the boundary layer still effectively increases the radius of curvature and hence reduces the peak velocity compared to that of an ideal flow. This variation in velocity across the passage manifests as a static pressure variation which in turn effects the local surface flow diffusion rates.

Parsons *et al* (1973) studied experimentally and computationally the effects of curvature on two-dimensional flow. Testing three different geometries of diffusing ducts, each with different amount of turning, they concluded that the streamline curvature had a substantial affect on flow development, especially on boundary layer development. They found considerable discrepancies between the designed and measured wall pressure distributions, especially for the short curved diffuser. In particular they found that the errors in predicted boundary layer growth using the two dimensional turbulent boundary layer Moses method [Kline *et al* (1968)], which ignores the effect of curvature, were greatest for the shorter curved duct. They also suggest that the effects of wall curvature on boundary layer development is due to turbulent shear stress modification rather than due to the effect of normal pressure gradient. This was concluded from investigations which modified Moses method to correct for shear stress. It was found that the modification of the boundary layer calculations due to the normal pressure gradient term was negligible for the three diffusers.

Gillis *et al* (1983) examined the turbulent structure of two-dimensional boundary layers as they flowed around a 90° convex bend. They concluded that as the flow accelerated around the convex bend, the turbulent length scale is reduced along with the boundary layer thickness, through the action of the normal pressure gradient $\rho U^2/R$. i.e. the boundary layer is compressed and hence turbulence suppressed by the normal pressure gradient. Muck *et al* (1985) and Hoffmann *et al* (1985) studied the effect of convex and concave surfaces respectively, on turbulent boundary layers. Their investigations focused on the detailed structure of the turbulent boundary layers, i.e. large and small scale eddies and longitudinal and spanwise turbulence, however, they concluded that the effect of a concave surface was to de-stabilise the boundary layer, and a convex curvature to stabilise. This agrees with the findings of Gillis *et al* (1983). Barlow *et al*

(1988) who also studied the structure of turbulent boundary layers on concave surfaces using flow visualisation and laser Doppler anemometry. They concluded that the primary effect of concave curvature is to amplify large scale eddies and also that mixing across the boundary layer is enhanced causing a significant increase in skin friction coefficient.

What can be concluded from these studies is that the turbulence structure, boundary layer thickness and normal pressure gradient are all inter-related, so that a change in say normal pressure gradient as a result of streamline curvature, will have an affect on both the boundary layer thickness and the turbulence structure of the flow.

2.4.4 Boundary Layer Blockage

As surface boundary layers grow thicker along a duct, the effective area of the duct reduces, hence reducing the actual static pressure recovery.
As described in the previous section, flow on a curved surface can alter the thickness of the boundary layer depending on whether the curved surface is either concave or convex.
This blocked area due to boundary layers can be defined in terms of the boundary layer displacement thicknesses, δ^*, which in the case of the Durham swan neck duct are suffixed hub and casing. Equation 2.8 defines the blocked area.

$$A_{block} = \pi\left[\left(r_{cas}\right)^2 - \left(r_{cas} - \delta^*_{cas}\right)^2\right] + \pi\left[\left(r_{hub} + \delta^*_{hub}\right)^2 - \left(r_{hub}\right)^2\right] \qquad \{2.8\}$$

where boundary layer thickness, δ^*, is defined by equation 2.9

$$\delta^* = \frac{1}{Vm}\int_0^\infty (Vm - V)dy \qquad \{2.9\}$$

where Vm is the free stream velocity and y is the perpendicular distance from the surface.

2.4.5 Swirling Flows

In many circumstances swirling flows within a diffuser occur either as a result of incomplete straightening of the flow as turbines are run progressively off design, or for specific requirements of downstream components. An extensive amount of research has been carried out on swirling flows in ducts and how they effect the structure of turbulent

boundary layers and static pressure recovery. Bradshaw (1973) demonstrated that centrifugal and Coriolis body forces alter the turbulent structure of the flow. For swirling flow in an annular passage, the production of turbulent energy is suppressed in the vicinity of the hub wall where the radial pressure gradient of angular momentum is positive and enhanced near the casing wall where this gradient is negative. These gradients arise because the swirling flow sets up a centrifugal force which must be balanced by an equal and opposite radial pressure gradient. The difference in turbulent energy production implies variation in the rate of growth of the surface boundary layers and their ability to sustain stream wise pressure gradients without separation. Increased turbulent production near the casing enhances its ability to remain attached whereas on the hub the opposite is true. Here, the turbulence is suppressed and the flow has a reduced capacity to sustain motion against an adverse axial pressure gradient. This would suggest that for axial flows in annular diffusers, inlet swirl would stabilise the flow on the casing surface and de-stabilise the hub surface flow ultimately leading to separation on the hub surface at too high swirl angles. This problem of the hub flow separation is amplified since, angular momentum is conserved, as demonstrated by Lohmann (1979), at least in the inviscid part of the flow. Therefore the tangential component of flow on both the hub and casing surfaces reduces as their radii increase, as the flow passes through the duct. Lohmann (1979) reported that the presence of swirl, alters the structure of turbulence in the diffuser causing premature separation from the inner wall. Hoadley *et al* (1969) showed that separation in a parallel-cored annular diffuser, (see figure 2.9) may be completely suppressed or moved from the normal outer wall position to the inner core depending on the amount of swirl present. Figure 2.9 defines the inner and outer divergence angles for conical and annular diffuser types.

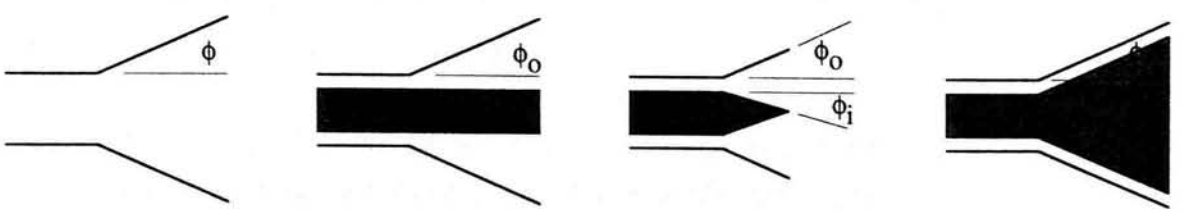

Figure 2.9 - Conical and Annular Diffusers

McDonald *et al* (1971) reported that the static pressure coefficient for diffusers operating in the attached or slightly separated flow regime with a purely axial inlet flow, was little affected by swirl. The report goes on to say that, for diffusers which were moderately or badly separated for axial inlet flow, swirling inlet flow caused large performance increases based on total kinetic energy. The data generally suggest that the swirl is optimum when the mean swirl angle is equal to the total divergence angle (2ϕ for conical diffusers, to $2\phi_O$ for parallel core annular diffusers), to the flow passage divergence angle (ϕ_O-ϕ_i for symmetrical annular diffusers (ϕ_i is negative) and to the outer wall angle ϕ_O for annular diffusers where ϕ_O=ϕ_i). An increase in static pressure coefficient of 15% can be achieved for these conditions.
Lohmann *et al* (1979) showed that for a diffusing, swirling flow, the static pressure coefficient at some axial location x, is given by equation 2.10, for inviscid flow.

$$Cp_x = \left(1 - \frac{\rho_i A_i^{\,2}}{\rho_x A_x^{\,2}}\right) + \tan^2 \alpha_i \left(1 - \frac{\rho_i \bar{r}_i^{\,2}}{\rho_x \bar{r}_x^{\,2}}\right) \qquad \{2.10\}$$

The first diffusion term is due to geometric area change and the second results from the change in mean radius of the flow. Note that even for a constant area duct, a change in mean radius leads to a change in static pressure if the inlet swirl angle is non-zero.

Lohmann (1979) discovered that the axial and tangential (circumferential) components of the flow were independent of each other. He found that for a well behaved flow (no separation) the diffusion produced by a change in radius was almost equal to the ideal recovery, defined by the second term in equation 2.10. The recovery of the axial component was found to depend strongly on both the swirl and cant angle, cant angle being the inclination from the axial plane.

Coladipietro *et al* (1975) and Kumar *et al* (1980) reported that for unstalled, straight walled annular diffusers the static pressure rise coefficient increased with increasing swirl. Kumar *et al* (1980) also reported that as the swirl angle increased, a peak in the static pressure recovery was reached, beyond which the static pressure recovery fell. This was attributed to the increased path length giving rise to increased rotational kinetic losses through skin friction.

Dovzhik *et al* (1975) investigated the affect of swirl on a constant area, straight walled annular pipe. They found that at small swirl angles the distribution of the circumferential velocity and swirl angle were close to constant. At higher swirl angles the flow in accordance with radial equilibrium moved towards the hub surface, but at high values of inlet swirl a significant decrease in the circumferential velocity and total pressure at the hub wall towards the exit of the pipe was noted. This was caused by displacement of the flow from the hub at large swirl angles.

It can be concluded from all the reports in this section that modest amounts of swirl within annular diffusers can be advantageous to the casing flow and overall duct performance, if it is partially or fully separated with no swirl present. With high angles of swirl and small cant angles, the hub flow is at risk of separation causing losses which outweigh any benefits realised by the casing flow. Also at high angles of swirl, the path length is greatly increased causing significant skin friction losses which add to this deficit.

Turbulence

The subject of turbulence has been briefly mentioned in the previous section. Bradshaw (1973) in particular gives a very comprehensive insight into the effects of streamline curvature on turbulent flow.

Turbulence plays an important part in the performance of diffusers since an increase in the level of free stream turbulence at entry to the diffuser can increase the static pressure recovered due to the suppression of otherwise separating boundary layers. This is often accompanied by an improved outlet velocity profile, but also an increase in total pressure loss coefficient due to energetic mixing within the flow. Changes in inlet turbulence levels are frequently accompanied by changes in inlet boundary layer profiles which probably dominate any changes in duct performance which could be adverse or beneficial. Also, high levels of turbulence intensity are only achieved close to the object producing them; ESDU (1976) suggests that significant increases are only realised up to 10 hydraulic diameters (4 x inlet cross sectional area of duct / cross-sectional perimeter) downstream.

Baines *et al* (1951) conducted a series of tests on biplane lattices with air as the working fluid and measured the turbulence intensity from immediately downstream of the grid to approximately 2000 bar diameters downstream. He then plotted log turbulence intensity against log non-dimensional length and arrived at an empirical relationship for the decay rate of turbulence intensity which was valid from approximately 10 bar diameters downstream of the grid, equation 2.11. x is the distance downstream from the bars and b is the bar diameter. Below a value of 10 bar diameters where the flow is not homogeneous the turbulence level increases in the region where turbulence is initially generated. These large scale eddies then gradually decay into smaller eddies and turbulence intensity decreases.

$$Tu\% = 1.12\left(\frac{x}{b}\right)^{-5/7} \qquad \{2.11\}$$

A comparable relationship is expected for perforated plate screens however, this data displayed too great a scatter for definite conclusions to be drawn

Turbulence can have a large effect on the static pressure recovered in a diffuser, not only due to suppression of potentially or actually separating boundary layers. For example, if a diffuser is followed by a parallel duct, the static pressure recovery will continue to rise as the velocity distribution changes due to turbulent mixing, Cockrell *et al* (1963).
Fully developed turbulent flow in annuli was investigated by Brighton *et al* (1964) by measuring friction factors, mean velocities and the distributions of the three components of turbulence intensity and Reynolds stress.

Azad *et al* (1989) investigated turbulent flow in a conical diffuser. Their aim was to understand the effects of perturbations caused by an adverse pressure gradient, divergence, and streamline curvature on turbulence structure, similar to the investigations by Bradshaw (1973).
It was found that the degree of anisotropy of the three components of the r.m.s. relative turbulence intensities decreased from the wall to the diffuser axis. The axial and circumferential components peaked at the duct wall. The radial component reached a maximum away from the wall, approximately at the edge of the boundary layer. This peak gradually shifted away from the wall with distance in the stream wise direction.

Stevens *et al* (1980) found a marked improvement in the stability of the outlet flow and gains in pressure recovery of up to 20%, with only small increases in total pressure loss. The free stream turbulence level at exit from the combustor is naturally high since it is one of the aims of a combustor to provide high rates of mixing between the hot combustion gases and cooling compressor air to try and achieve a maximum temperature distortion variation at entry to the H.P. stage of 10%. Because of this, typical free stream turbulence levels at exit from the H.P. turbine stage and hence entry to the inter-turbine diffuser are between 4 and 6 percent which will improve the diffuser performance due to turbulent boundary layers remaining attached.

2.4.7 Flow Regimes

Flow regimes have been studied in two-dimensional straight walled diffusers by Kline *et al* (1959) and in two-dimensional curved walled diffusers by Fox *et al* (1962). Fox *et al* found that when holding inlet flow conditions, wall length, and throat width constant, four main flow regimes were observed as the divergence angle increased from zero degrees. These are described below and illustrated in figure 2.10. Note the grey areas represent boundary layers or flow boundaries such as the boundary between the jet flow and re circulatory zone in figure 2.10D.

A) A regime of well behaved, apparently unstalled flow.

B) A regime of large transitory stall in which the separation varies in position, size, and intensity with time. This is a regime of highly pulsating flows.

C) A region of fully developed stall in which the major portion of the diffuser is filled with a large triangular shaped recirculation region extending from the diffuser exit to a position close to the diffuser throat. The main flow follows along one wall continuously, and is relatively steady.

D) A jet flow regime in which the main flow is separated from both walls, and does not reattach until well downstream of the diffuser. This occurs only at quite high angles of divergence.

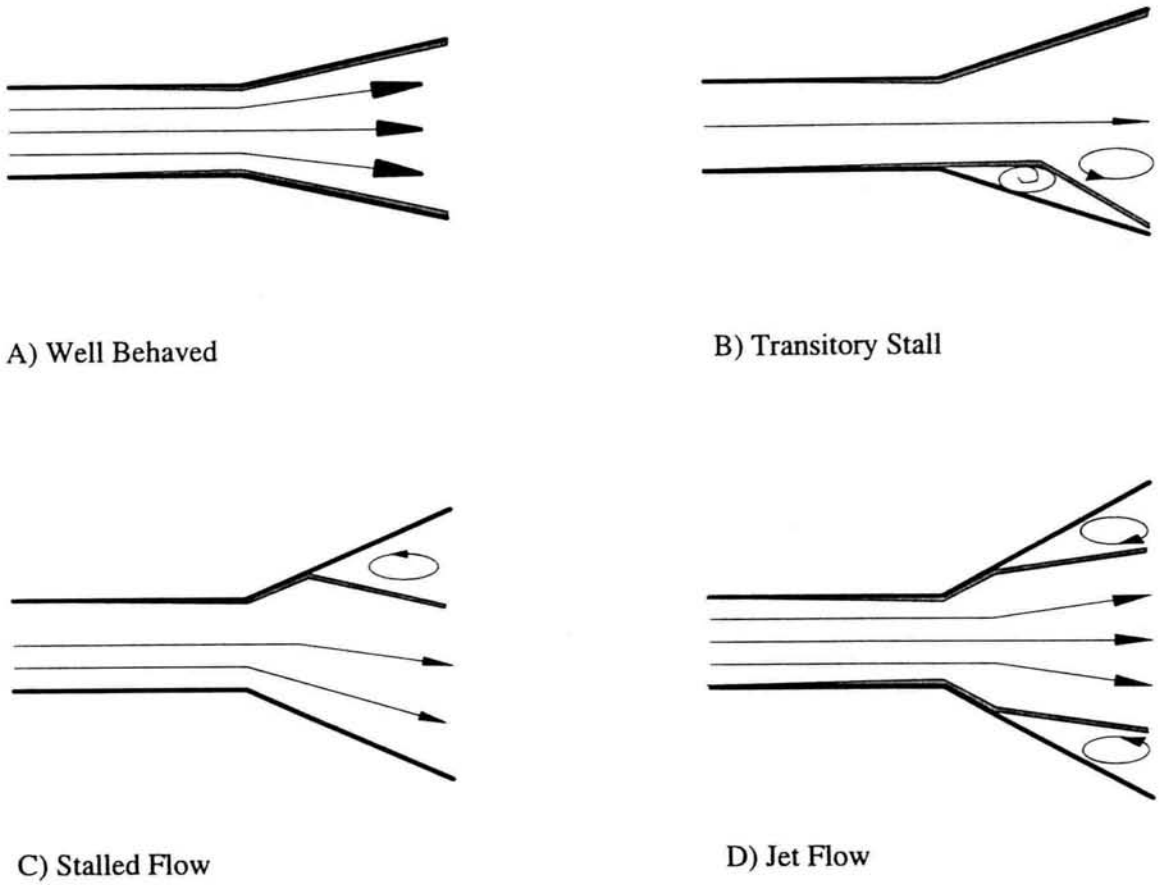

Figure 2.10 - Diffuser Flow Regimes

Even though it is convenient to divide flow patterns into these distinct regimes, in practice they represent an essentially continuous spectrum, with lower axial pressure gradients and shorter diffusers giving less stall. The subject of the paper by Kline *et al* (1959) was the prediction of optimum performance and flow regime for various diffuser geometryies. The information was based upon empirical correlations between experimental data gathered from two-dimensional, conical and annular straight walled diffusers. They found that optimum recovery for a constant length occurs on the flow regime border between no appreciable stall and large transitory stall. From a design point of view however, this would not be a good choice since this represents a region of highly pulsating and unsteady flows. A larger divergence angle producing a more steady but fully separated flow may be a better choice if length needs to be kept as short as possible.

In a study performed by McDonald *et al* (1966) it was found that the flow condition steadily deteriorated as either diffuser length or diffuser angle was increased. Truly steady flow was attainable in the diffuser only for very moderate opening angles and lengths. For moderate divergence angles, the main flow was steady but the pattern of stall near the wall was not. Only for the most severe diffuser configuration tested (2φ =32.6°, figure 2.9 for definition) was the stall pattern almost completely stationary. The flow regime or stall patterns progressed from steady flow to local fixed stall via intermittent transitory stall, local transitory stall and intermittent fixed stall. Their results also showed that the line of maximum performance fell below the line of first appreciable stall and go on to say that conical diffusers designed for maximum performance will be free from any stall which affects the flow significantly. This finding was contrary to those found by Kline *et al* (1959) who found that the line of optimum recovery of straight walled diffusers lay between the lines of no appreciable stall and large transitory stall. It would seem that flow separation would be delayed in a conical diffuser since there are no corners present, and separation in plane walled two-dimensional diffusers is known to begin in the corners Kline *et al* (1959). McDonald *et al* postulates that this argument would tend to explain the direction of the shift in the line of appreciable stall, but it would not necessarily account for the magnitude of the change.

2.4.8 Reynolds Number

Reynolds number is defined by equation 2.12.

$$\mathrm{Re} = \frac{\rho v x}{\mu} \qquad \{2.12\}$$

where x is taken as the inlet passage height = 63.02mm.

Reynolds number affects diffuser flows in two ways. Firstly for a given diffuser geometry, variation in Reynolds number will affect the inlet boundary layer thickness and hence the diffuser loss. Secondly it will affect the growth of the boundary layer within the diffuser.

For Reynolds numbers greater than 5 x 10^4 the bulk of the data available suggests that the pressure recovery is independent of inlet Reynolds number. McDonald *et al* (1966) tested a number of conical diffusers with water as the working fluid and found that for a particular diffuser geometry, there was significant low Reynolds number effect on performance (Re. no. < 7 x 10^4). They also found that for Reynolds numbers greater than this, the pressure recovery remained constant. They attributed the drop in performance with decreasing Reynolds number to a laminar separation immediately downstream of the diffuser throat. For the higher Reynolds number flows, the flow was completely turbulent at the throat and no variation in performance as a function of Reynolds number was found for any of the geometries tested for Re. no. > 75,000.
Cockrell *et al* (1963) found that for the range of inlet Reynolds numbers tested ($3.5x10^4$ to $5.2x10^5$) there was no detectable trend with Reynolds number. Gibson (1911) tested his water filled pipes with divergent boundaries with inlet Reynolds number in the range $5x10^4$ to $2.5x10^5$ and also found no appreciable variation with Re.

2.4.9 Inlet Flow Conditions

It has long been recognised that diffuser performance depends not only on the physical shape of the duct but also upon the type of inflow conditions. In 1957 Winternitz *et al* conducted experiments to investigate the effect of inlet conditions on the performance of conical diffusers with 4:1 area ratio and 5 and 10 degrees total angle of expansion. They found that as inlet momentum thickness increased, the static pressure recovery coefficient decreased, more so in the 10 degree case. This decrease was also found to occur with increasing cant angle. They also found that both the momentum thickness and shape factor at the exit of the diffuser depended heavily on the inlet momentum thickness suggesting that it is an important parameter in controlling diffuser performance.

In most turbomachinery diffusers, low energy wakes created from upstream stages exist which decay in intensity with distance. In diffusing ducts, the decay of these wakes will be strongly influenced by radial and axial pressure gradients. Bragg *et al* (1971) investigated both experimentally and computationally the effects of an axially directed adverse pressure gradient on turbulent wakes created by an upstream row of parallel cylinders. The results show that a larger decay rate of the free stream velocity

immediately downstream of the rods is observed for a greater adverse pressure gradient. This only applied for a downstream distance of approximately 36 rod diameters; beyond this, the decay rates were the same for the two different adverse pressure gradients. They were able to model the flow reasonably accurately with their simplified momentum superposition theory, Bragg *et al* (1971), but for the more extreme case, the flow was better predicted using Patankar *et al's* (1967) finite difference method.

Hill *et al* (1963) provide a clearer picture of the effect of adverse pressure gradients on wake growth/decay rates. They measured the profile of a wake generated by a rectangular aluminium bar with a rounded leading edge, at 5 axial locations in a variable geometry diffuser. They measured the wake at all locations for 4 different positive axial pressure gradients varying from a nearly constant pressure wake flow to an extreme diffusion where the flow in the central portion of the diffuser may stagnate. Their results clearly show that in a nearly constant axial pressure gradient, the wake decays very rapidly as it mixes with the free stream due to large shear stresses. When under the influence of a positive pressure gradient the relative wake size tended to decrease much less rapidly. Finally they showed that if the rate of pressure rise in a diffuser is sufficiently rapid, the relative wake size may actually grow rather than decay and its growth may lead to stagnant flow in the central portion of the diffuser. They found unsteady measurements in the latter stations within the diffuser but total pressure measurements failed to reveal any significant back flow.

Adenubi (1976) investigated experimentally the performance and flow regime of annular diffusers with axial flow inlet conditions. His measurements were made on straight walled annular diffusers preceded by an axial compressor. As expected he found that the measured mean axial turbulence intensities (5 to 7 percent) were higher than would be found in an equivalent ducted flow (2 to 3 percent), and hence it is apparent that blade induced turbulence constitutes a significant fraction of the overall turbulence level in the flow leaving the compressor.

Hoffmann *et al* (1984) tested a two-dimensional curved wall diffuser and found that with high intensity inlet turbulence, the pressure recovery coefficient of the diffuser was increased by 10 percent at 2ϕ=9 degrees and by 22 percent in the transitory stall flow regime with 2ϕ=20 degrees. They attributed this increase to the increased turbulence

acting within the diffuser to reduce distortion and delay separation, thereby causing an entirely different flow regime to occur.

Zierer's (1993) investigation of the flow in a diffuser behind an axial flow compressor concluded that considerably higher pressure recovery could be achieved compared to a ducted flow case due to increased turbulent mixing delaying the onset of separation.

Distorted inlet velocity profiles can be both beneficial and detrimental to a diffusers performance, depending upon the velocity profile and the geometry of the diffuser. For example, peaky profiles (figure 2.11) with a high V_{max}/V_{mean}, tend to give poor performance since the static pressure recovery is to some extent, limited by the maximum velocity reduction allowable near the walls. Conversely, profiles which have a lower center-line velocity than V_{mean} tend to give better performance even than near uniform flows, ESDU (1976). Such profiles occur downstream of obstacles in a duct (wake-type profiles), or as the result of a bell mouth entry. If the flow on a wall where separation is likely can be predicted, separation can be delayed if higher velocities of an asymmetric profile are biased towards that wall, figure 2.11.

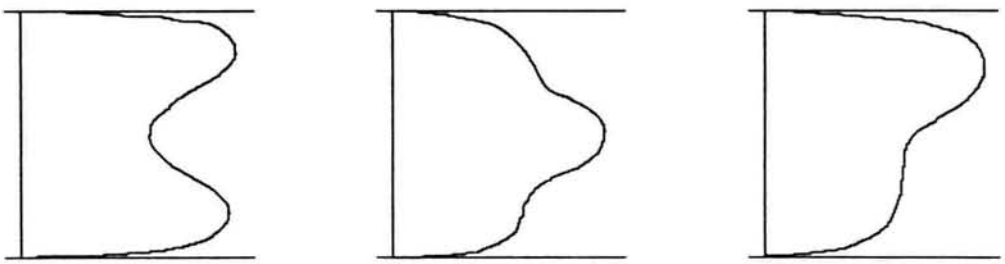

Figure 2.11 - Velocity Profile Shapes

2.4.10 Mach Number

From continuity of mass flow it can be shown that:

$$V = \frac{m}{\rho . A} \qquad \{2.13\}$$

With compressible flow, both area, A, and density, ρ, increase with passage down the diffuser so that the reduction in velocity, V, will be greater than in the case for incompressible flow where only cross sectional area increases, Adkins *et al* (1990). It therefore follows that the static pressure recovery should be greater for the compressible case. This is however a detrimental effect on recovery since if the flow is slowed down more quickly in compressible flow, there will be a greater likelihood of flow separation.

Adkins *et al* (1990) used a new method using the so called 'G' parameter to calculate the effects of compressibility on static pressure recovery. They found that the rate of increase in values of Cp is not rapid until Mach numbers of 0.6 are exceeded, and then the effect is most pronounced when area ratios are low. They concluded that if a diffuser inlet Mach number is to exceed 0.6, then the wall angle must be reduced in order to counteract the effects of compressibility in increasing the adverse pressure gradient. Diffusers taking into account this effect would therefore adopt a trumpet shape where the adverse pressure gradients are reduced in the early part of the diffuser and increased in the latter part where the flow is likely to be diffused to a lower Mach number.

ESDU (1976) suggests that the effect of compressibility for Mach numbers up to values of 0.5 to 0.6 are probably less than about 10% on Cp, being greatest for thicker inlet boundary layers and larger wall angles, Tyler *et al* (1967). For higher Mach numbers the effects become more significant culminating in a sudden drop in Cp when choking of the flow occurs.

2.5 S-Shaped Annular Ducts

Although considerable research has been carried out on simple 2D diffusers as described in this chapter up until now, very few publications exist on fully three dimensional curved walled annular diffusers, especially when employed as inter-turbine diffusers.
S-shaped annular ducts can be used in gas turbines for a variety of applications. Perhaps most common is to connect the often large diameter fan with the smaller diameter multi-stage I.P. or H.P. compressor, where it is called an inter compressor swan neck duct, shown in figure 2.12. In this application there is usually little or no overall diffusion however, for very short ducts local diffusion rates can be high enough to cause flow separation.

S-shaped annular diffusers are used to connect H.P. and L.P. turbines on concentric shafts shown in figure 2.12 which will be referred to as 'inter-turbine diffusers'. They can also connect totally separate turbines on so called 'free power shafts' which will be termed 'inter-stage diffusers'. Finally, although drawn as a straight walled diffuser in figure 2.12, swan neck ducts can be employed as exhaust diffusers for particular applications which will be discussed shortly.

Circular s-shaped ducts as opposed to annular are used on aircraft intakes and hence encounter similar problems such as flow separation and secondary flows.

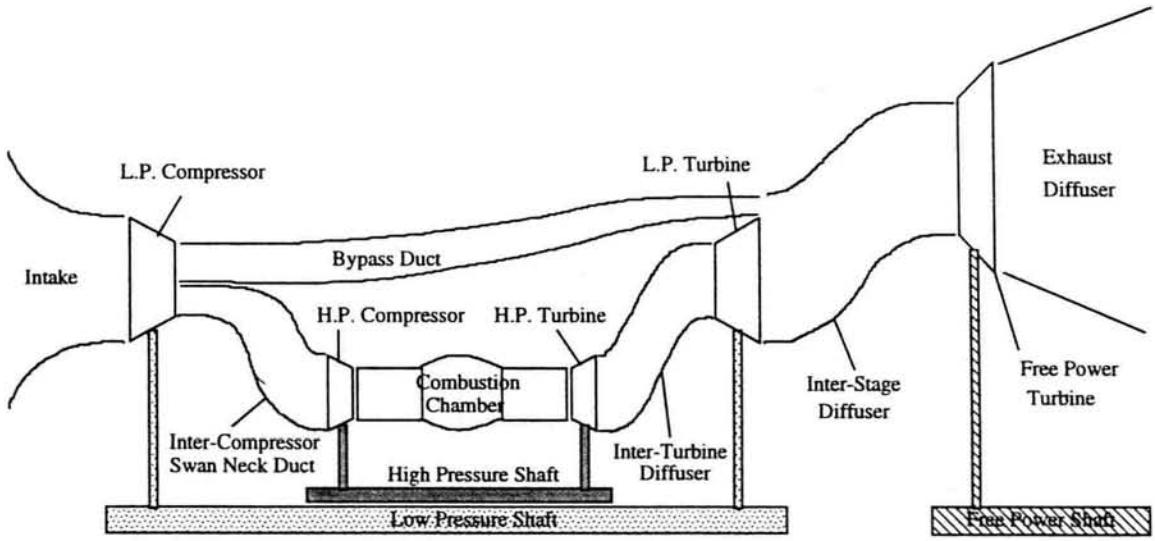

Figure 2.12 - Gas Turbine Schematic

Diffusers are not all designed to achieve the same objectives, i.e. maximum pressure recovery in a short as distance as possible with little or no total pressure loss, with the same aims.

In a power turbine exhaust diffuser (figure 2.12) the flow is decelerated to effect an increase in static pressure. Since the diffuser exit pressure is determined by the engine exhaust conditions, a static pressure rise in the power turbine exhaust diffuser is manifested as a static pressure fall at the exit of the power turbine. This potentially allows a greater engine output power due to a greater available pressure drop across the power turbine.

In an inter-turbine or inter-stage diffuser, the flow is decelerated because the downstream turbine requires a much lower velocity flow compared to the significantly

higher through flow velocity of the upstream stage. In this role, it is the diffusers primary aim to reduce the velocity of the flow and increase mean radius with minimal energy loss.

Amann *et al* (1971) investigated the deleterious effects of turbine exit flow non-uniformity on diffuser behaviour. They tested two curved wall annular diffusers with the same area ratio of 1 : 1.85 but one being three times the length of the other. The longer diffuser was designed have a near optimum dimensionless length of 5.55 and would therefore be expected to be free of significant flow separation. The dimensionless length was defined as being the average wall length of the diffuser divided by the annulus radial height at the diffuser inlet. In contrast the shorter diffuser, having a dimensionless length of 1.95 should experience severe separation. Both diffusers were tested with the presence of an upstream turbine and for two cases, with and without a downstream nozzle stage. Without a downstream stage present they found that both diffusers experienced flow separation from their outer walls with the shorter diffuser giving more extensive separation. The addition of a downstream stage significantly altered the flow in the separated regions. Flow uniformity at the exits of the diffusers was radically improved over that existing in the absence of the nozzle. The downstream nozzle therefore had an advantageous upstream effect on the flow in the diffuser. They concluded that, although the pressure loss coefficient and blockage at the power turbine nozzle exit were lower with the longer diffuser than the short, the flow improvement effected by the nozzle was sufficient, to make tolerable for some applications, an inter-stage diffuser about one-third as long as the optimum suggested by diffuser rig tests.

Thayer (1971) investigated the performance of curved wall annular exhaust diffusers with the motive being to suppress infrared signals emitted by the hot turbine which can be used to guide heat-seeking missiles. In this application a curved wall diffuser is required to eliminate any downstream line-of-sight with the hot radiation emitting turbine. A number of diffuser configurations were tested, some with and without the addition of 6 elliptical section struts, which are used to support the inner shaft and supply cooling air which is also injected into the exhaust to reduce infrared emissions. Although the area ratios of the diffusers tested were greater than that of the Durham swan neck ducts, 1.8 to 3.67 compared to 1.5 for the Durham ducts, Thayer's diffusers were significantly longer than the Durham ducts and hence lower diffusion rates reduced

the likelihood of flow separation. His results show that when struts were installed into the ducts, the static pressure recovery coefficient reduced by an average of 7.9% with the worst case being 14.8%. This corresponded to an average reduction in effectiveness of 8.3% with the worst case being 14.9%. He also varied the amount of inlet swirl and found that without struts a slight rise in performance from 0 to 20 degrees swirl occurred but then a rapid decrease in Cp of about 15% between 20 and 32 degrees. Also changing inlet mach number from 0.25 to 0.45 had a negligible effect on Cp at all three swirl angles. With struts installed, increasing swirl from 0 to 20 degrees resulted in 5 to 20 percent loss in Cp whilst drastic losses occurred at 32 degrees swirl. Increasing inlet mach number from 0.25 to 0.45 caused relatively small losses at 20 and 32 degrees, indicating that small increases in blockage or size of strut wakes occurs as Mach number is increased.

Wellborn *et al* (1994) investigated experimentally the flow in a diffusing inlet s-duct. The inlet Mach number was 0.6, Reynolds no. 2.6×10^6 and a nominal inlet turbulence intensity of 0.65%. The duct was circular in cross section and had an area ratio of 1.52 (approximately the same as the Durham diffusers). Using surface oil-flow visualisation techniques and full area traversing with aerodynamic probes they found that a large region of stream wise separation occurred within the duct. Duct curvature induced strong pressure driven secondary flows, which evolved into counter rotating vortices. These vortices convected low momentum fluid of the boundary layer to the free stream, degrading both the uniformity and the magnitude of the total pressure profile.
Harloff *et al* (1993) and Anderson *et al* (1994) attempted to model this flow using O and H grids with full and reduced Navier Stokes models. They found that their models generally predicted the flow reasonably well however, they consistently predicted flow separation further downstream in the inlet S-Duct than was indicated by measuremental data.

Britchford *et al* (1993, 1994) and Bailey *et al* (1996, 1997) investigated the performance of an inter-compressor swan neck duct. The difference between this duct and the Durham diffusers is that their duct is of constant area and therefore no diffusion occurs due to an area increase occurs. Diffusion will occur locally within the duct due to streamline curvature as discussed earlier in this chapter, however the magnitude due to the absence of an additional area increased diffusion will be less than in the Durham

SND making the flow better behaved and hence easier to predict numerically. Their duct has an upstream rotor stage to produce representative inlet wakes to the duct and outlet vanes to remove any swirl. Bailey *et al's* (1997) paper introduces a single NACA 65 profile symmetrical strut with 12 percent thickness/chord ratio, into the 'S' section of the duct which is similar in many ways to the Durham case. Their strut is instrumented with static pressure tappings at 10%, 50% and 90% of strut span. They found that the duct stagnation pressure loss coefficient increased from 0.020 to 0.035 when the rotor was added. They attributed this additional loss to mixing of the OGV wakes within the duct. When the struts were added to the duct they found no significant regions of flow separation and that the influence of a single strut on overall performance is relatively small. For the clean inlet case, the loss coefficient increased from 0.040 to 0.042 when a single strut was incorporated, with corresponding values of 0.035 and 0.038 with the upstream compressor present. The single strut in this case could be a source of two possible errors. Firstly that of circumferential periodicity, especially if the flow is insufficiently straightened, and secondly, the number of struts in a real duct would cause sufficient blockage as to affect the curved wall surface flow; i.e. the actual duct loss with the struts in situ could be greater than the sum of the isolated strut and duct losses.

Sonada *et al* (1997) investigated the flow within an annular s-shaped duct which although intended for an inter-compressor application, nevertheless had some area increase (Ae/Ai=1.2). Their inlet mach number was 0.386 and the duct contained 6 NACA 0021 profile struts which were instrumented at 11%, 44% and 89% span. Their results showed that a region of total pressure loss near to the hub (which corresponds to the casing flow in the Durham SND) was due to instability of the flow. The results for the Durham SND will show that the same flow feature was observed due to even larger diffusion rates caused by an area ratio of 1.5.

Finally Dominy *et al* (1994, 95 & 96) and Norris *et al* (1997) have published the results of various investigations carried out on the Durham swan neck duct which has a diffusion ratio of 1.5. Dominy *et al's* (1994) paper examines the effect of inlet wakes to an annular diffuser with moderate diffusion rates. It shows that the flow is strongly influenced by the presence of simple inlet wakes which provide a mechanism for strong secondary flows to develop which lead to total pressure distortions at the exit of the duct. Their second paper (1995) investigates the effect of swirl on the flow in the same

annular duct and demonstrates that swirl can alleviate the peak suction on the first casing bend. They also show that the mean radius increase creates a differential increase of swirl angle through the duct which leads to a pronounced skewing of the flow giving rise to greater merging of the wakes and casing boundary layer than occurs for axial flow. Dominy *et al's* (1996) paper presents and compares results from a comparable Rolls-Royce model turbine rig which has an upstream turbine stage to produce wakes in the scaled model diffusing duct. It also introduces some CFD predictions made with the Rolls-Royce solver M.E.F.P. The results showed that the Durham swan neck duct which gives a much simplified inlet flow compared to the model turbine rig, provides a means for better understanding of the flow development through the diffuser. The CFD predictions showed reasonable agreement with the experimental measurements.

Norris *et al's* (1997) paper which contains data extracted from this thesis, examines both experimentally and computationally, the effects of diffusion rates and inlet blade wakes on the flow in diffusing swan neck ducts. It achieves this by introducing a second 70% shorter duct with the same overall area ratio as the original which produces more extreme local diffusion rates within the duct. Both the experimental and computational results showed the same percentage decrease in static pressure recovery when comparing the more extreme duct with the original. The same results also showed that the intensity of the inlet wakes strongly influenced the magnitude of the secondary flows which developed within the two ducts.

Chapter 3

Experimental Apparatus and Instrumentation

3.1 Introduction

This chapter describes the apparatus and instrumentation used to obtain the experimental data presented in this thesis.

3.2 The Durham Annular Test Rig

The test rig shown in a sectional view in figure 3.1 and in a photograph, figure 3.2, is supported by means of a purpose built square section mobile frame, allowing the whole rig to be separated from the fan which draws air through it. The test rig which consists of concentric inner and outer sections, hub and casing sections respectively, is designed to allow quick and easy access to the working section. The inner hub section is firmly bolted to the rear of the frame and is designed to be rigid and stationary whilst the outer casing section is suspended from above on rollers and is allowed to move forwards and backwards in the axial direction. In this way, by releasing a few bolts which usually keep the casing section located firmly in place for the duration of a test, the working section can be quickly accessed which is required for the installation of various instrumentation, e.g. different probes. This also allows access to a ring of aerodynamic struts which are mounted around the inner hub by means of two radial pins per strut and which are held firmly in place once the outer casing section is bolted in the closed position. The struts are discussed in more detail in section 3.3.3.

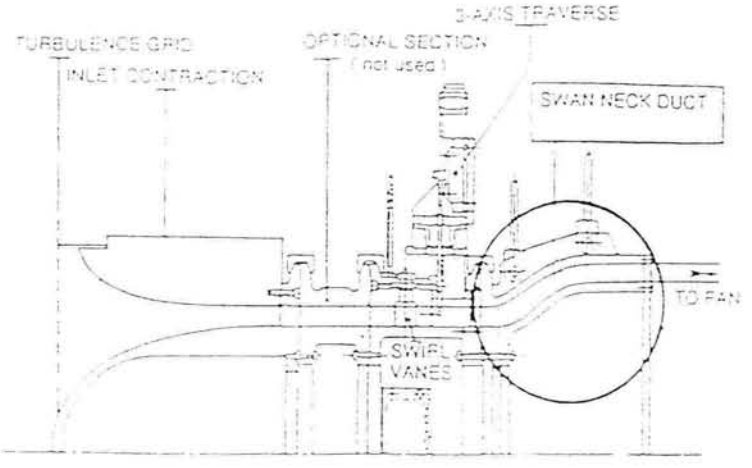

Figure 3.1 - Sectional Diagram of the Test Rig

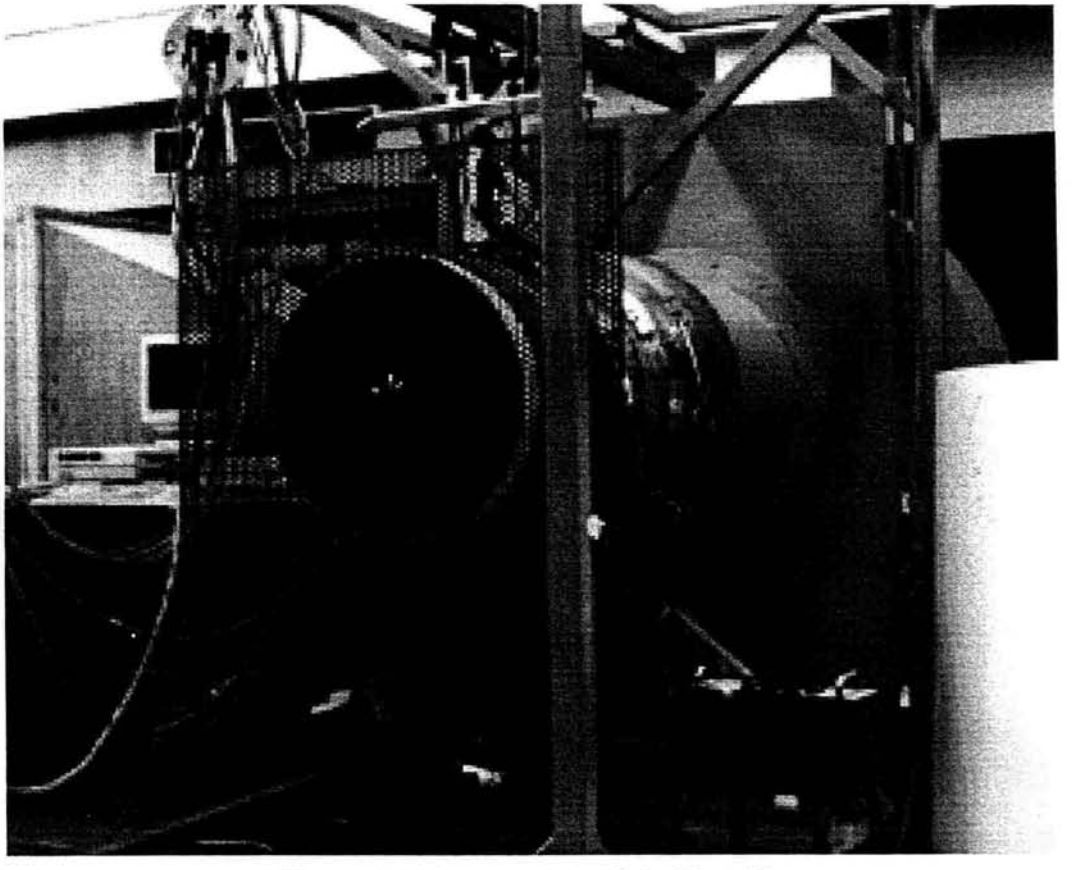

Figure 3.2 - Photograph of the Test Rig

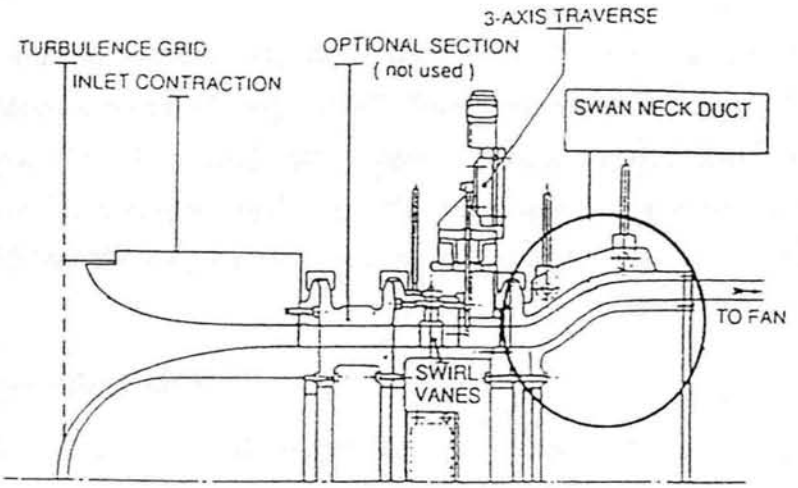

Figure 3.1 - Sectional Diagram of the Test Rig

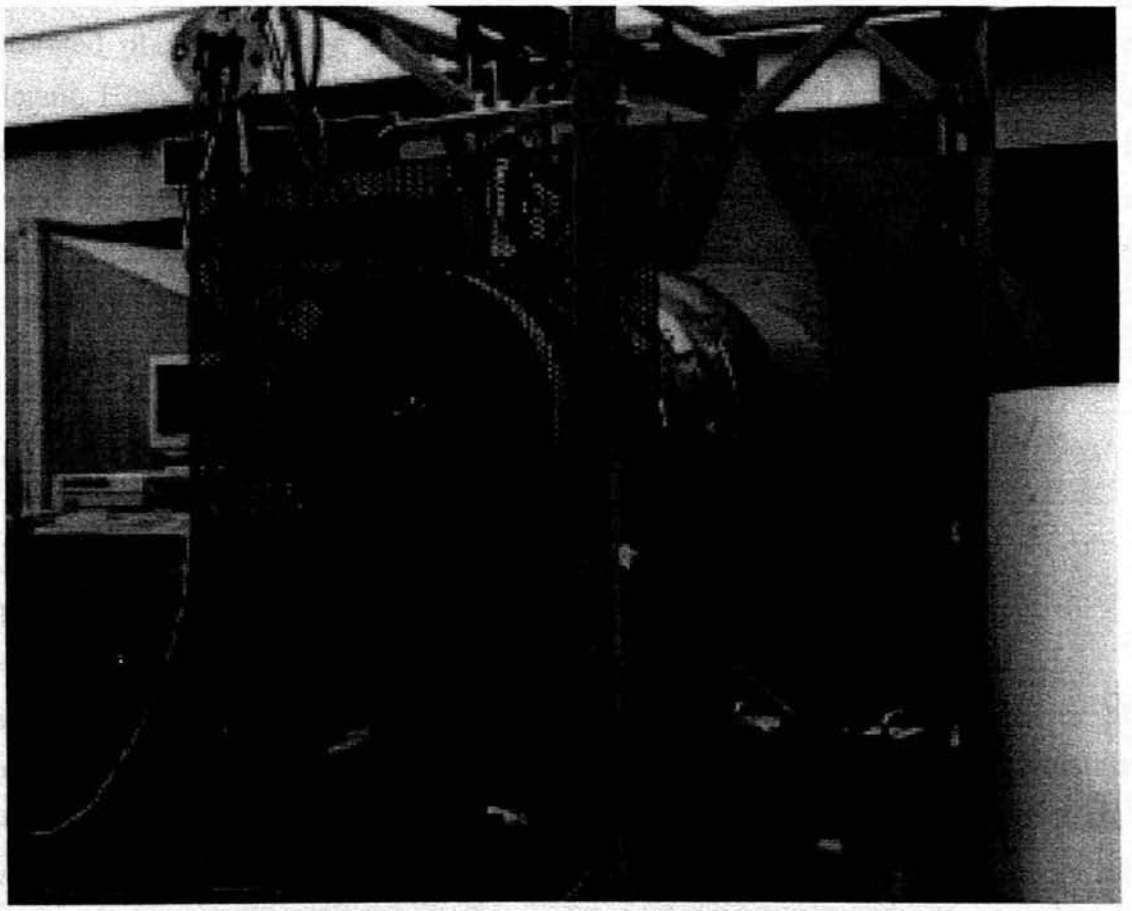

Figure 3.2 - Photograph of the Test Rig

3.2.1 The Air Supply

The test rig is sub-atmospheric and air is drawn into the annular cascade by a 55kW three-phase induction motor driving a Keith Blackman series 28 centrifugal fan, (model number 900/287/1/1). An ABB Stromburg frequency controller (ACS503-061-3-00P200000) provides a continuously variable drive speed to the fan up to a maximum air velocity of 85 m/s (Mach No. ≈ 0.23) at entry to the working section, figure 3.1.

3.2.2 Turbulence Generating Grid

The air, which is drawn in from atmosphere, passes through a perforated plate turbulence grid in order to produce conditions more akin to those experienced in a real inter-turbine diffuser, although these would be much more complex due to upstream stages. The main factor in producing large levels of turbulence is the bar size (if using a lattice grid) or the web size (if using a perforated plate). Baines *et al* (1951) showed that the total pressure loss through a lattice type grid was lower than that through a perforated plate generating the same level of turbulence, hence making them more efficient. However, lattice type grids with large diameter bars are not readily available which makes them expensive and hence a readily available perforated plate which produced similar turbulence levels to that of a large bar diameter lattice was chosen. From the dimensions given in figure 3.3 and using equation 3.1, the percentage blockage of the grid due to geometric considerations is 53.7%.

$$Blockage\% = \left[1 - \left(\frac{\sqrt{3}\pi c^2}{6a^2}\right)\right] \times 100\% \qquad \{3.1\}$$

Where a is the hole pitch and c the hole diameter.

Or in words, Blockage = Blocked Area / Total Area

The total pressure loss through the grid is proportional to the velocity squared of the flow passing through it. Since it is desirable to have a near uniform total pressure and velocity distribution from hub to casing at inlet to the swan neck duct test section, it is therefore necessary to situate the turbulence grid in a similar flow regime to ensure equal loss across it. For this reason the position of the grid was optimised which meant

employing a plastic tube interface (shown in figure 3.4) between the grid and the casing which also serves to stabilise the casing boundary layer. A central hole of 100 mm diameter was then needed in the perforated sheet to allow the nose of the inner wooden bullet which forms the hub surface of the inlet contraction to protrude out. These features may be seen in figure 3.4. The grid produced a nominal free stream turbulence intensity of 2% measured at the inlet plane (plane -1, fig. 3.14), which is lower than the 4-6% representative of a real inter-turbine diffuser inlet.

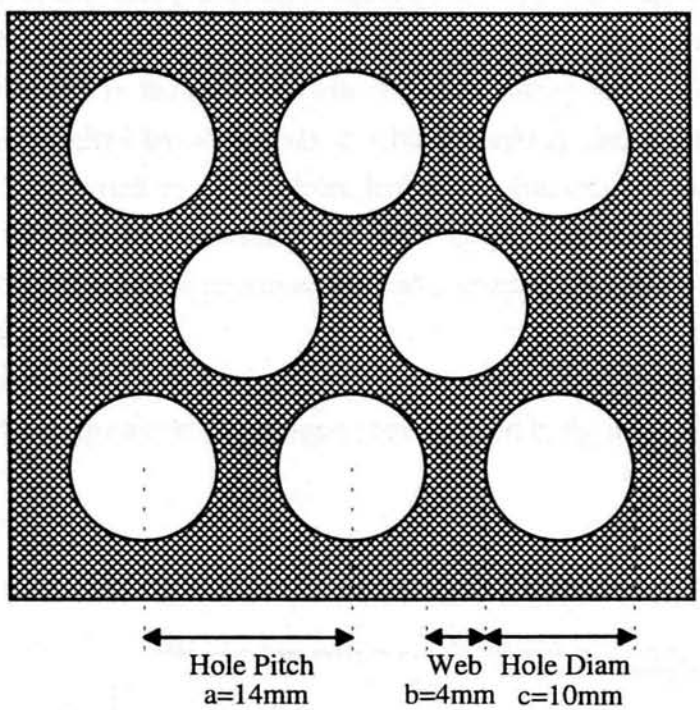

Figure 3.3 - Perforated Plate Geometry

3.2.3 New Inlet Contraction

A new inlet contraction was designed for the test rig in order to eliminate the non-uniform inlet total pressure and velocity variations from hub to casing which existed with the previous inlet. A further problem of the previous inlet was that it produced a relatively thick and unsteady casing boundary layer which was undesirable, particularly as the casing flow is subjected to extreme accelerations around the first bend. This unsteadiness and non-uniform radial inlet pressure profile was first measured by Kirkham (1993). He partially solved the problem by adding a tube to the inlet casing

which improved the unsteadiness measured with boundary layer probes in the casing boundary layer downstream of the first bend. The new inlet contraction was designed to solve both problems, the non-uniform radial total pressure profile and the casing unsteadiness. The new inlet was analysed using the commercially available CFD software package PHOENICS. The code and grid were first validated by modelling the original inlet and compared with the experimental results. A good correlation between these results provided confidence in its use as a design tool for the new inlet. The original inner hub of the inlet consisted of a turned wooden laminated bullet which was elliptical in shape and henced caused no unsteadiness or flow separation. It was therefore left unchanged in the new inlet and the outer casing duct was designed around the geomery of the original bullet in order to obtain a steady and radially uniform flow. The outer casing was turned on a lathe from laminated wood and hence the outer radius was limited by the size of the lathe. The new casing contraction had a smoother elliptical shape compared to the previous and had a contraction ratio of 3.7:1, unlike the original design by Kirkham.

The final optimised casing and tube, which note is shorter than the protruding bullet in order to achieve the desired inlet conditions, may be seen in figure 3.4.

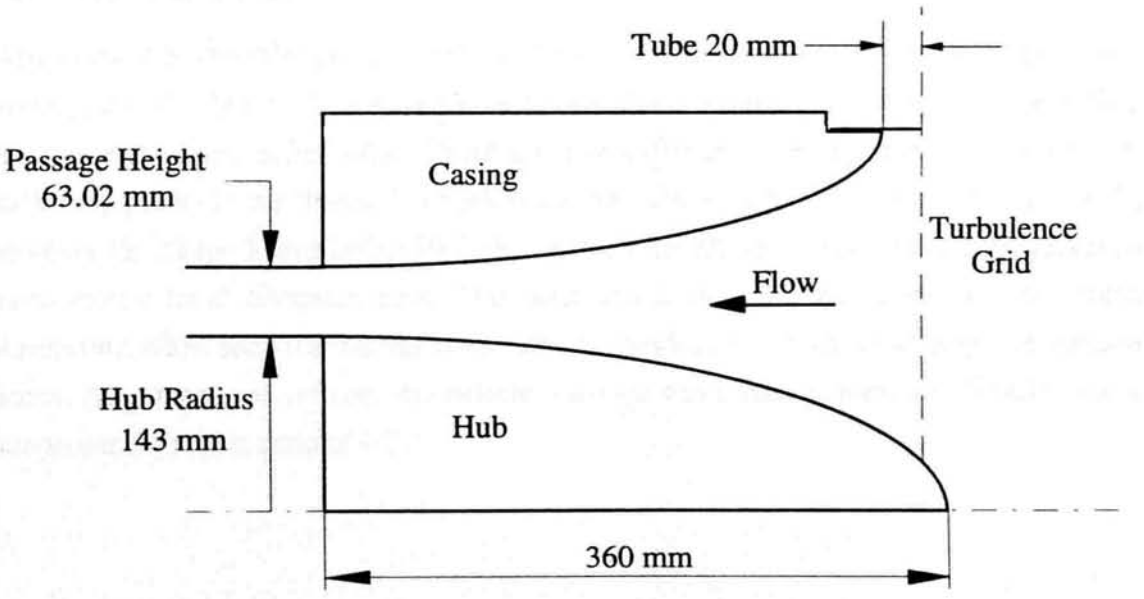

Figure 3.4 - The Inlet Contraction

3.2.4 Inlet Swirl

Immediately downstream of the inlet contraction a row of 34 symmetrical fixed swirl vanes are used to provide the working section with both swirling inlet flow, and inlet wakes, i.e. conditions akin to those found at the inlet to a real diffuser. The vanes were originally introduced to produce swirl only and were therefore situated far upstream of the first bend in order for the wakes to decay and mix out before entering the duct. Area traverse results shown in chapter 4 show evidence of the inlet wakes even after the first bend, especially at high incidence angles due to severe flow separation on the IGV leading edge.

The vanes have a 32mm chord, are of a flat plate design of 1.5mm thickness with circular leading edge and 30° trailing edge. These can be set either at zero degrees where they simulate engine design conditions i.e. purely axial flow with simulated upstream turbine wakes, or, they can be used to simulate off design conditions by providing swirling flow into the duct. Two fixed vane angles, 15 and 30 degrees have been tested, since these angles cover the range of swirl angles found in real engines at various off design conditions, e.g. Idle through to full power take off.

3.2.5 The Swan Neck Ducts

Downstream of the inlet guide vanes the flow passes through the inlet measuring station (inlet plane -1, figures 3.14 & 3.16) and then flows through a parallel section before entering the swan necked duct. There are two different 'working sections' or annular diffusers, 'phase 1' and 'phase 2' which have the same exit to inlet ratios ($A_e/A_i = 1.5$), however the phase 2 duct being 70% shorter than the phase 1, (see figure 3.5), achieves more severe local diffusion rates. The hubs and casings of both ducts are cast from aluminium alloy and then turned on a lathe to produce the final geometry and surface finish. At entry to the diffuser the parallel passage has a hub diameter of 286mm and a hub to casing radius ratio of 0.7.

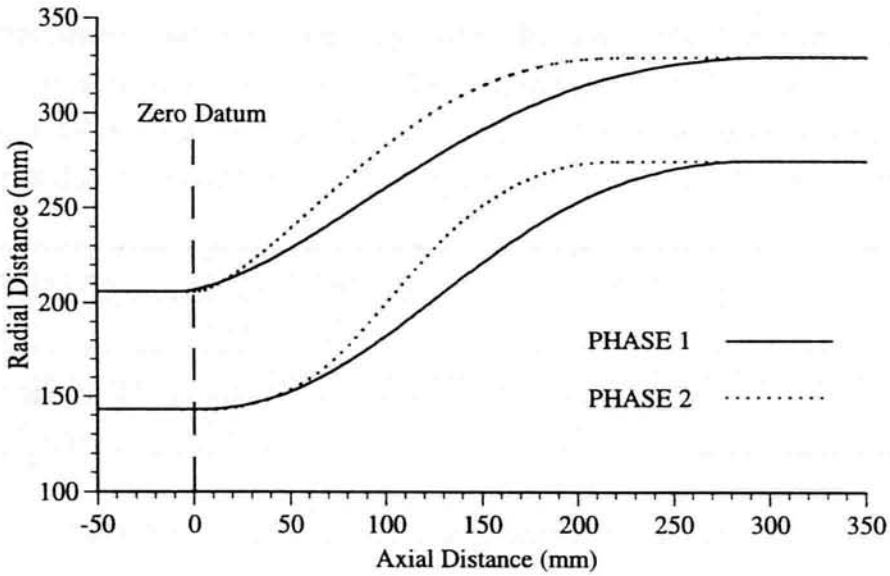

Figure 3.5 - Diagram Comparing Phase 1 and Phase 2 Ducts

3.3 Instrumentation

In order to measure the aerodynamic performance of the duct a significant amount of instrumentation (mainly using pressure transducers) had to be implemented. Some of this instrumentation such as traverses and probes already existed but the rest has been specified and modified accordingly. The majority of the pressure results taken were time averaged so to a certain degree the frequency response of the system was not of prime importance. These pressures which included 3 & 5 hole probe and surface static pressures were connected to a scanivalve which allowed up to 48 ports to be stepped through and converted to voltages via the scanivalve's own pressure transducer.

For the unsteady investigations where frequency response was paramount, factors such as tube length and selection of pressure transducer had to be carefully chosen, hence the scanivalve was not used.

3.3.1 Pressure Transducers

Selection and Specification

For the bulk of the aerodynamic results which included boundary layer traverses, area traverses, duct static pressure development and strut surface static pressure distributions, the scanivalve pressure transducers were used. For these measurements a fast reacting

pressure transducer was not necessary since the data collected was usually time averaged over a number of seconds. The specifications of the scanivalve pressure transducers may be seen in table 3.1. The bulk of the measurements used the more sensitive transducer although the ±1.75 bar transducer's resolution was still reasonable.

Manufacturer	Druck Limited	Druck Limited
Type	PDCR 22	PDCR 22
Pressure Range	± 35,000 Pa (± 350 mbar)	± 175,000 Pa (± 1.75 bar)
D.C. Supply	12V	12V

Table 3.1 - Scanivalve Pressure Transducers' Specifications

For measuring the unsteady components of pressure accurately, a fast response transducer with minimum hypodermic tube length was necessary. For these measurements a single differential pressure transducer was situated directly next to the particular static pressure tapping being used. The reference side of the pressure transducer was connected to an inlet static pressure tapping whose pressure was known to be steady and close to that of the one being measured so that the transducer was kept within its range yet maintaining very good sensitivity. This pressure transducer's specifications are shown in table 3.2.

Manufacturer	Sensor Technics
Type	143SC01D-PCB
Pressure Range	± 6895 Pa (± 1 psi)
Typical Response Time	0.1 ms
D.C. Supply	12V
Output Range	1-6V
Zero Pressure Offset	3.5V

Table 3.2 - Unsteady Pressure Transducer's Specifications

The tube was 85mm long and had an internal diameter of 0.5mm. Its transfer function was first tested using a simple piece of experimental apparatus consisting of a loud

speaker driven by a varying frequency sinusoid from a signal generator, developed by Sims-Williams *et al* (1998). The signal measured by the transducer connected to the 85mm length of tubing and connectors was compared using fourier analysis against the 'true' signal as measured by another reference pressure transducer at the source. The magnitude of the signal measured at the end of the tube divided by the magnitude of the signal measured at the source is known as as the tube transfer function and is shown in figure 3.6. For clarity the range 0 - 100 Hz has been plotted although the system was tested from 6 Hz upto 300 Hz with a 250 Hz second order analogue cut-off filter to remove any unwanted high order interefence.

A surprising result shown by Sims-Williams *et al* (1998) is that the speed of sound and hence resonance frequency are significantly reduced in thin tubes due to viscous effects. In this particular tube system, the tube resonance dominates any viscous effects for all the frequencies tested. The expected resonant frequency for an 85mm open ended tube is approximately 1 kHz although in practice this number is likely to be 500 Hz as a result of viscous affects. At 100 Hz the signal is amplified by 4% and at 250 Hz the value is approximately 30%.

As the frequency to be measured was due to large scale flow separations and not high frequency turbulence, the tube length was considered suitable, i.e. 0-100Hz range is adequate. The phase shift of the signal was not of any interest as it was only the frequency of the dominant aerodynamic unsteadiness which was being investigated.

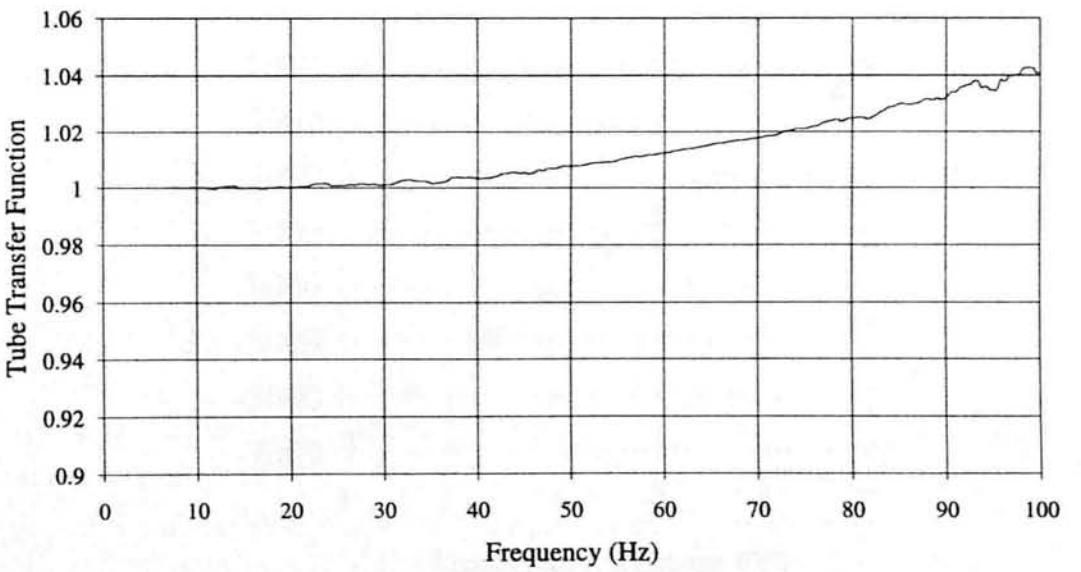

Figure 3.6 - Transfer Function of Unsteady Pressure Transducer Tube

Calibration

The transducers were calibrated using a simple system shown in figure 3.7. A known pressure by sucking or blowing measured using a sensitive oil filled micro manometer was held constant using a valve and the output voltage of the pressure transducer noted. This was applied to a variety of positive and negative gauge pressures (the reference hole of the pressure transducer was left open to atmosphere). A typical calibration graph is shown in figure 3.8. The transducer is shown to be very linear within its range.

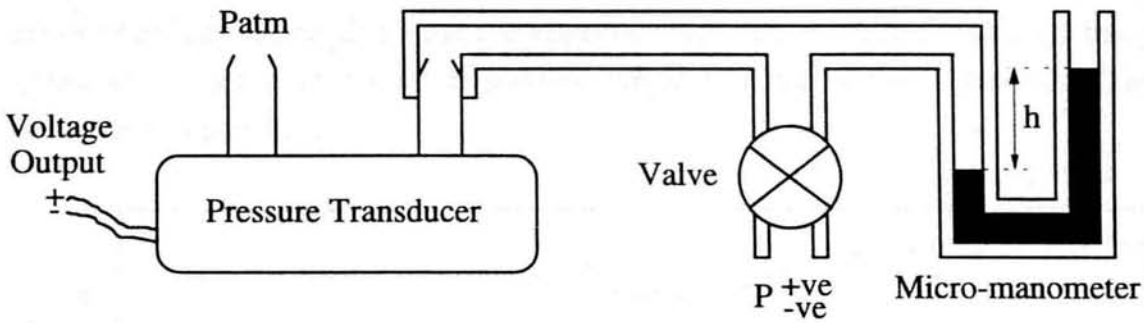

Figure 3.7 - Schematic Diagram of Transducer Calibration System

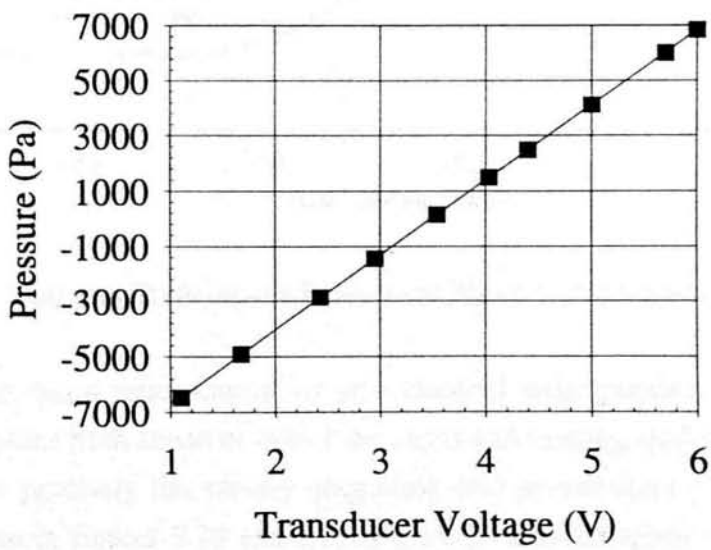

Figure 3.8 - Typical Pressure Transducer Calibration

.3.2 Static Pressure Tappings

Both phase 1 and phase 2 ducts have static pressure tappings on their hub and casing surfaces along their lengths. In the phase 1 duct these pressure tappings lie at the same circumferential angle as viewed from the front of the duct which meant only one boundary layer could be traversed at a time since the probe's wake interfered with the downstream boundary layer. In the phase 2 duct the pressure tappings were arranged at different circumferential positions around the duct to avoid the problems of the phase 1 duct. They were also arranged in pairs so that the boundary layer probe could traverse up to the surface between them and the local static pressure could be interpolated between the two tappings, hence giving more confidence in the measurements. Figure 3.9 below shows the positions of the static pressure tappings in the phase 1 duct which are tabulated in appendix A.

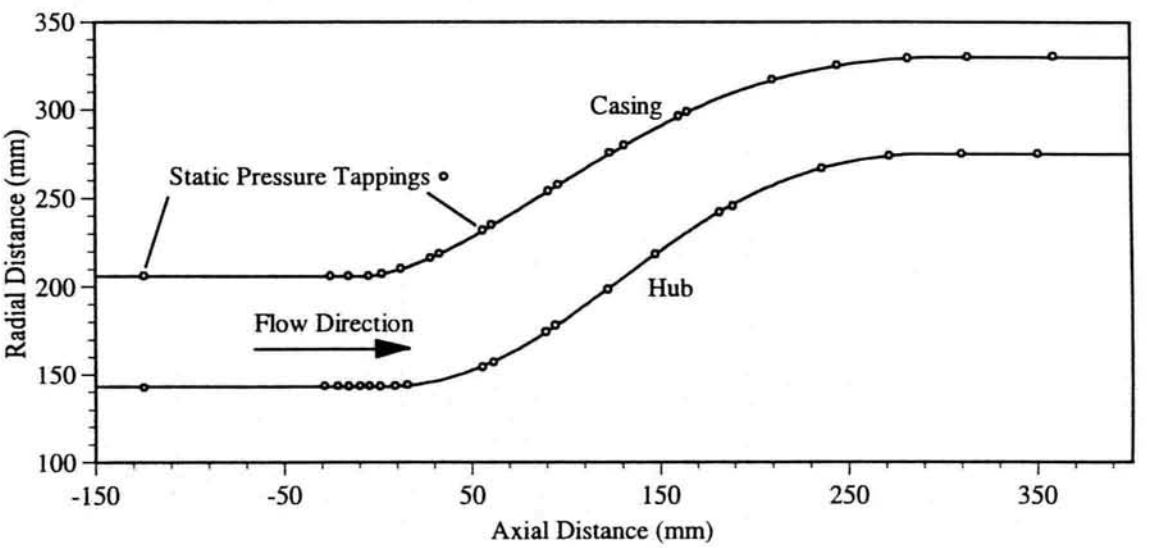

Figure 3.9 - Diagram Showing the Position of Phase 1 Static Pressure Tappings

The phase 2 duct has a concentration of 16 additional static pressure tappings situated on the casing surface both ahead of one of the struts and running mid-strut pitch in order to capture more precisely the rapidly stagnating and accelerating flows respectively. This may be seen in figures 3.10 and 3.11. Figure 3.11 is a diagram of what would be seen if looking perpendicular to the casing surface.

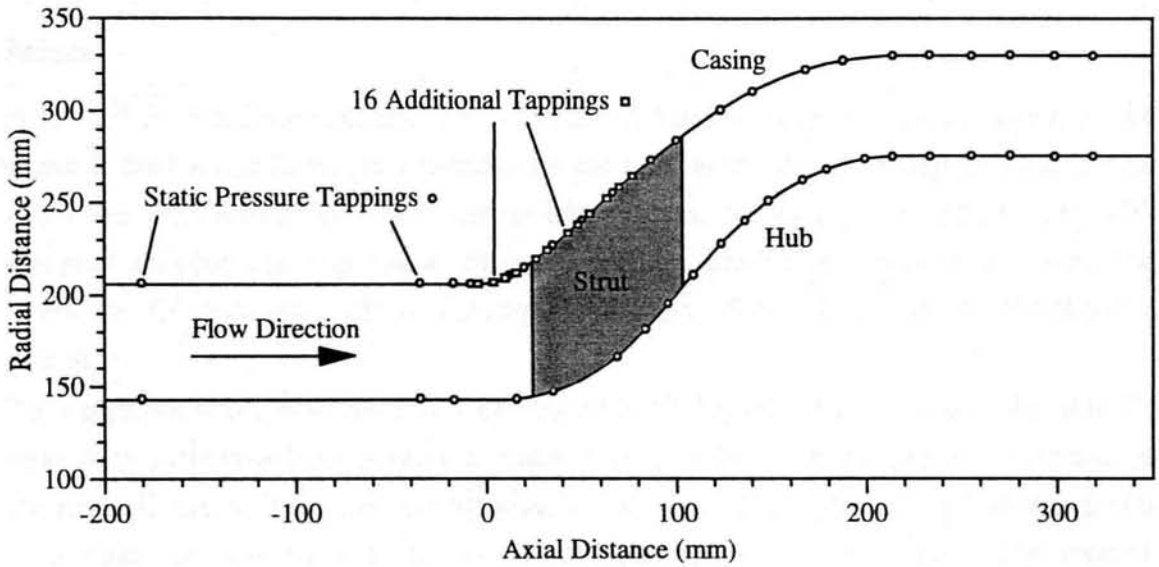

Figure 3.10 - Diagram Showing the Position of Phase 2 Static Pressure Tappings

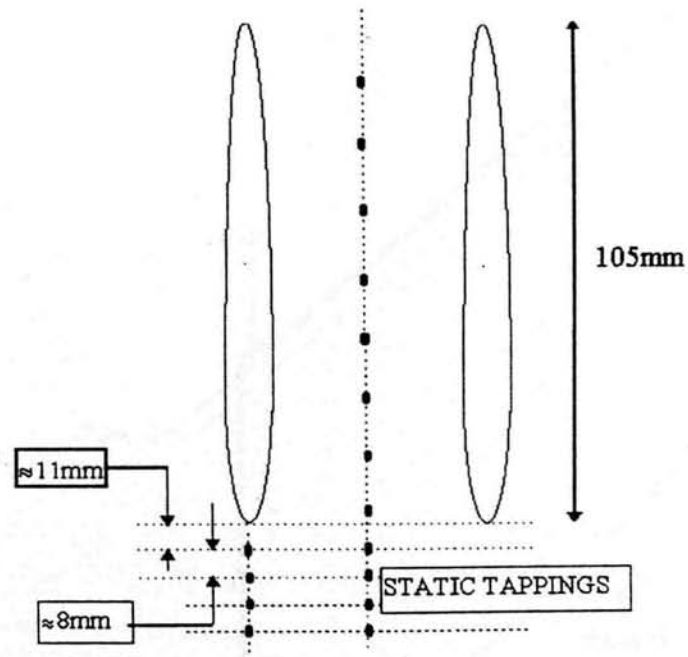

Figure 3.11 - 16 Additional Strut Casing Static Pressure Tappings

3.3.3 Struts

A row of 26 fixed symmetrical C4 aerofoils referred to as *struts* can be added to the phase 2 duct immediately downstream of the first bend, shown in figure 3.10. These struts are required in the real inter-turbine diffuser to supply the engine core with essential cooling and lubrication fluids as well as providing structural support. The struts are C4 aerofoils with a maximum thickness of 12.5% of the chord (chord = 80mm).

Two adjacent struts positioned at approximately 80 degrees from the top of the annulus have their respective facing surfaces instrumented with 180 static pressure tappings as shown in figure 3.12. Instrumenting adjacent faces (or a strut passage) allow the affects of a wake (or two) passing through a strut passage to be investigated. The relative position of the inlet guide vanes and struts can be altered to allow the affects of an igv wake incident on the strut to be investigated, as would occur in the real diffuser. Tables of exact co-ordinates of the tapping positions may be found in appendix B.

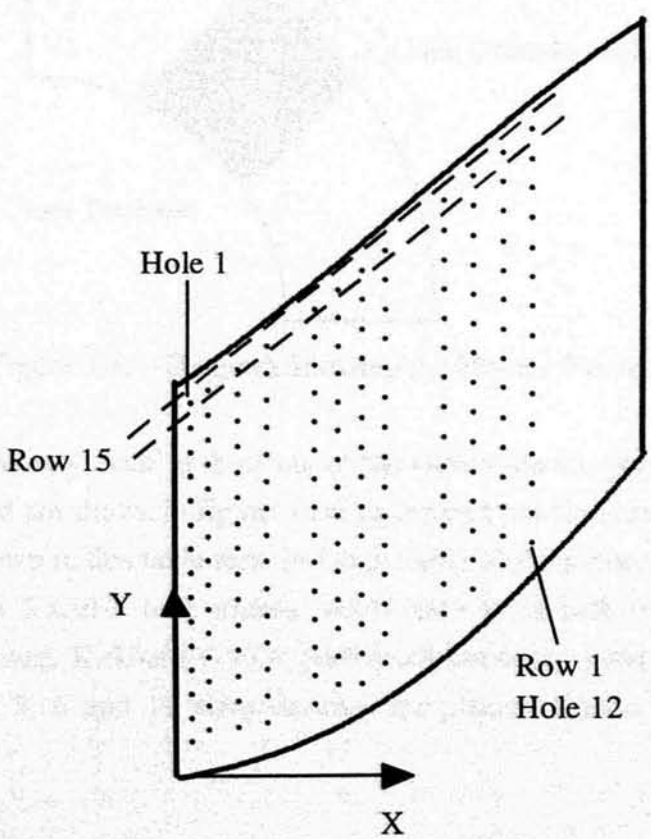

Figure 3.12 - Strut Static Pressure Tapping Positions and Notation

3.3.4 Traverses

Phase1 Duct

The phase 1 duct has 11 traverse planes along its length which allow area traversing with 3 and 5 hole probes etc, by means of radial and linear circumferential traverses as shown in figure 3.13. The linear circumferential traverse does not allow true circumferential traversing since it uses x-y coordinates, however, it is possible using x-y coordinates to traverse a true single passage of the annulus. The results contained in this thesis used existing logging software which traversed the area shown in figure 3.13. The range of the phase 1 traverse only allows one inlet guide vane pitch to be measured.

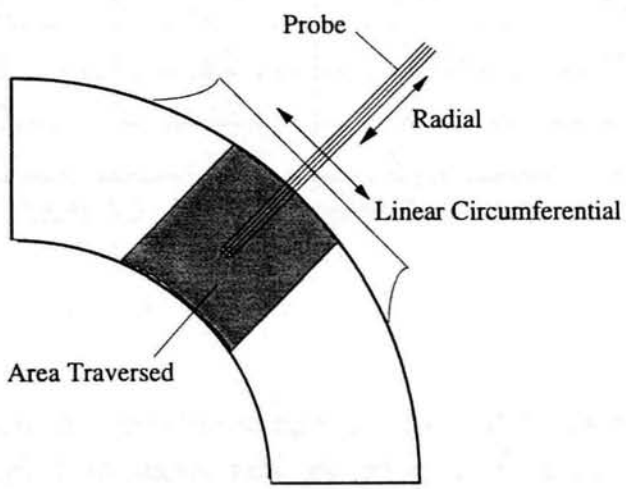

Figure 3.13 - Diagram Showing the Phase 1 Traverse

Area traverses were only made at three out of the eleven planes, plane 3, 6 and 11 (plus the inlet plane), and are shown in figure 3.14; their exact positions are listed in table 3.3. The x/h values shown in this table refer to the position of the probe tip. To area traverse all 11 planes with 3 and 5 hole probes would have been both time consuming and unnecessary, however, Kirkham (1993) performed boundary layer traverses at all 11 planes. Planes -1, 3, 6 and 11 were deemed the planes of most interest and hence traversed.

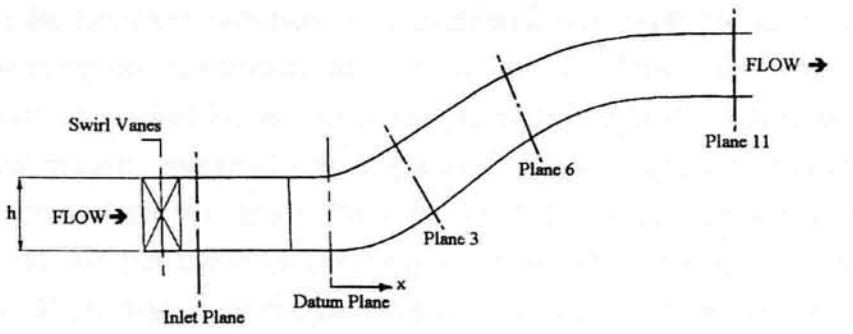

Figure 3.14 - Diagram Showing the Traverse Planes on the Phase 1 Duct

Traverse Plane	x/h (Hub)	x/h (Nominal)	x/h (Casing)
Inlet -1	-1.977	-1.977	-1.977
3	1.450	1.169	0.889
6	2.816	2.617	2.940
11	5.565	5.565	5.565

Table 3.3 - Phase1 Traverse Plane Locations

Phase 2 Duct

The phase 2 duct allows true area traversing at 5 axial positions along its length, plus the inlet plane -1. Figure 3.15 shows how the phase 2 achieves true circumferential traversing as opposed to the pseudo circumferential traversing of the phase 1 duct. The phase 2 duct was originally designed without struts and hence has slot 1 (shown in figure 3.16) which traverses immediately after the first bend. This slot has the same nominal non-dimensional axial position (x/h) as plane 3 in the phase 1, which allows direct comparison of the two ducts. It also has slot 2 in the parallel exit section which is equivalent to plane 11 in the phase 1. Note that all the planes in the phase 1 duct and slots 1 and 2 in the phase 2 duct traverse the duct in a direction nominally perpendicular to the streamlines. The phase 2 allows traversing at slots 1 and 2 over two inlet guide vane or strut pitches which is useful for checking circumferential periodicity. The duct was subsequently modified to include a row of struts which were situated such that the existing slot 1 was no longer usable because the probes would hit the struts when

traversed in the pitchwise direction. Two additional slots were added (Slots A and B) which allow traversing in between and just downstream of the struts. These slots allow traversing in a radial direction as opposed to perpendicular to the streamlines as in slots 1 and 2. Total pressure probes of various geometries were employed for slots A and B to traverse in and around the struts. The notation of the plane numbers were therefore termed A1, B1 and B2; the letter denoting which slot the probe used and the number, which plane. These planes are shown in figure 3.17. Table 3.4 lists the hub, casing and nominal axial locations of the probe tips accessed from all phase 2 duct traverse planes. Note that per cent Cax shown for Planes A1, B1 and B2 refers to the axial distance downstream from the strut leading edge as a percentage of the strut axial chord (80mm).

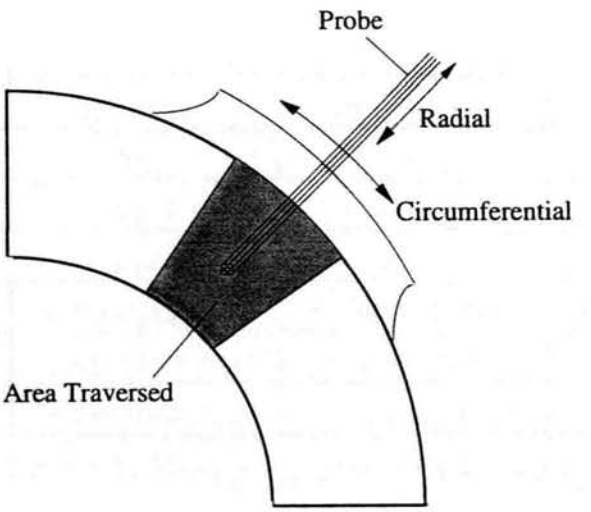

Figure 3.15 - Diagram Showing the Phase 2 Traverse

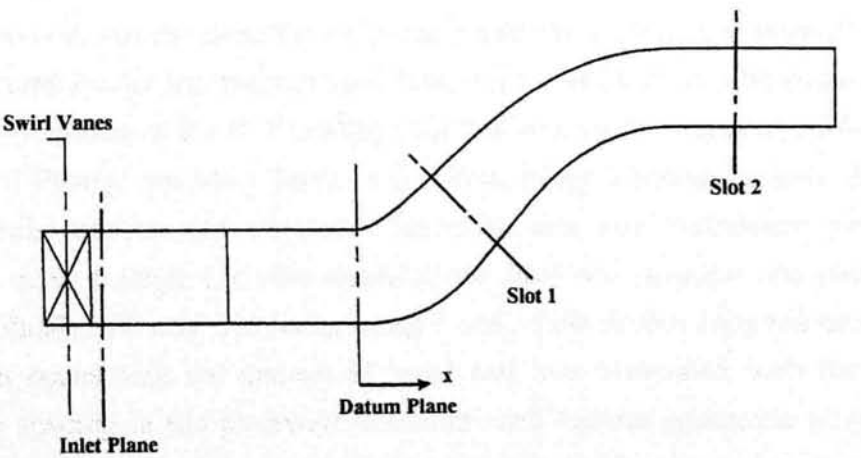

Figure 3.16 - Diagram Showing Slots 1 and 2 on the Phase 2 Duct

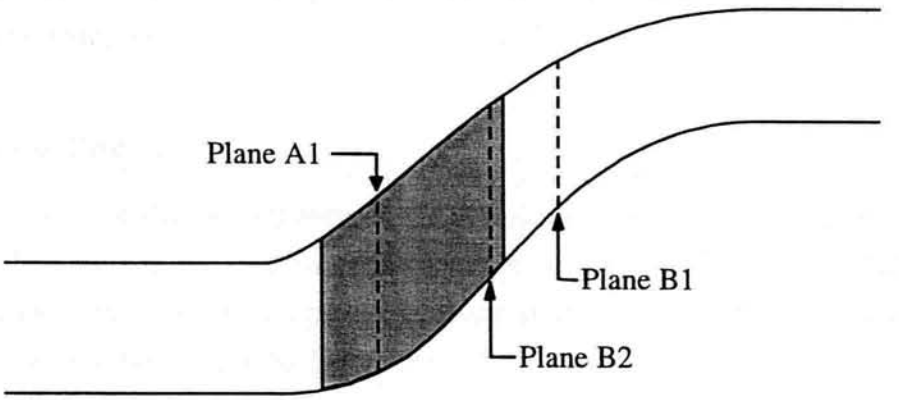

Figure 3.17 - Diagram Showing Planes A1, B1 and B2 on the Phase 2 Duct

Traverse Plane	x/h (Hub)	x/h (Nominal)	x/h (Casing)
Inlet -1	-2.856	-2.856	-2.856
Slot 1	1.511	1.149	0.788
Slot 2	4.062	4.062	4.062
Plane A1	0.778 (30% Cax)	0.778 (30% Cax)	0.778 (30% Cax)
Plane B1	2.088 (133% Cax)	2.088 (133% Cax)	2.088 (133% Cax)
Plane B2	1.590 (94% Cax)	1.590 (94% Cax)	1.590 (94% Cax)

Table 3.4 - Phase 2 Traverse Plane Locations

Inlet Traverse

The inlet traverse was the same for the phase 1 and phase 2 ducts. It consists of a 3-axis (radial, circumferential and yaw) traverse which is located half an inlet guide vane chord (15 mm) downstream of the IGV trailing edge and was used to obtain the following inlet information. Firstly, boundary layer information using a boundary layer probe using only the radial traverse was obtained. Secondly, area inlet turbulence measurements were made using a single hot wire assuming the flow was isotropic and purely axial in direction. Finally, full area traversing using 3 and 5 hole probes supplied necessary inlet information concerning the amount of swirl and loss associated with the inlet swirl vanes. The spacing in the pitchwise direction used various geometric progressions to accurately capture the relatively thin inlet wake depending upon the amount of inlet

swirl. This information was used to provide the computational predictions with the actual inlet conditions.

Aerodynamic Probes

In order to measure the performance of the two ducts it was necessary to measure data including the total and static pressure from which velocity can be calculated along with flow direction. For 3-D measurements, pressure probes were perfectly adequate. They were more robust and provided better resolution than multi-axis hot wires. This was because with the complex duct geometry, pressure probes could measure closer to the duct walls where a significant proportion of the duct loss is concentrated.

Probe Design Requirements

The overall probe diameter needed to be as small as possible to achieve the resolution within the duct which at exit is 55mm high in the radial direction. However using too small a tube size can lead to excess probe vibration and also makes the hypodermic tubes more susceptible to blockage by dust/debris in the air supply which is drawn unfiltered from atmosphere. It is also desirable to have the overall probe diameter as small as possible due to wall proximity effects. Dominy *et al* (1992) showed that when a nulled probe was brought into the vicinity of a wall, the flow acceleration between the probe and the wall caused a fall in static pressure of hole nearest to the wall.

As well as the size of probe, the type of probe needs to be decided upon. Probes can be split into two main types, namely probes with either conical or pyramidal shaped heads and probes with forward facing or perpendicular holes. Dominy *et al* (1992) tested various probe configurations and discussed their relative merits.

The effect of Reynolds number on the dynamic pressure coefficient was found to be less significant for a probe with perpendicular facing holes compared to one with forward facing holes. For low Reynolds number it was found that a leading edge separation bubble existed at incidence on the perpendicular cone probe. It was recommended that where possible, probes with perpendicular facing holes should be used in preference to those with forward facing holes. No difference was observed between the performance of equivalent conical and pyramidal probes when they were tested, nulled over a range of Reynolds numbers. From an aerodynamic point of view, the best choice would be the

perpendicular pyramidal probe shown in figure 3.18, however, this type of probe has to be manufactured from a solid block by turning and drilling which is difficult especially for small probes. For this reason the forward facing perpendicular type probe shown in figure 3.19 was used. It is manufactured from 5 hyperdermic tubes which are bundled together and ground to form the head with forward facing tappings. Finally, solder was run along the joints to give a smoother aerodynamic finish. The geometry of the 5 hole probe is shown in figure 3.20.

The 5-hole probe described was used to investigate the bulk flow, however, due to wall effects previously mentioned two 3-hole probes were required to measure the hub and casing wall regions. These were manufactured in the same way as the 5-hole probes and their geometries are shown in figure 3.21.

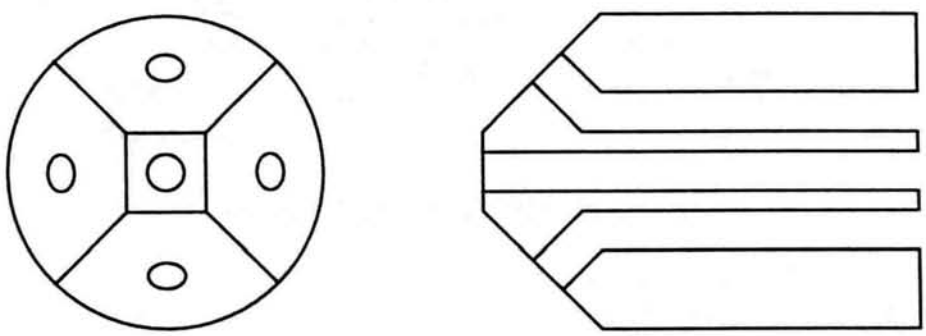

Figure 3.18 - Perpendicular Pyramid 5-Hole Probe

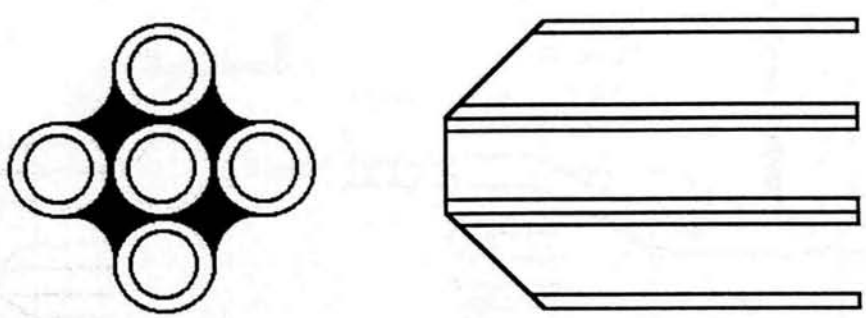

Figure 3.19 - Forward facing Pyramid 5-Hole Probe

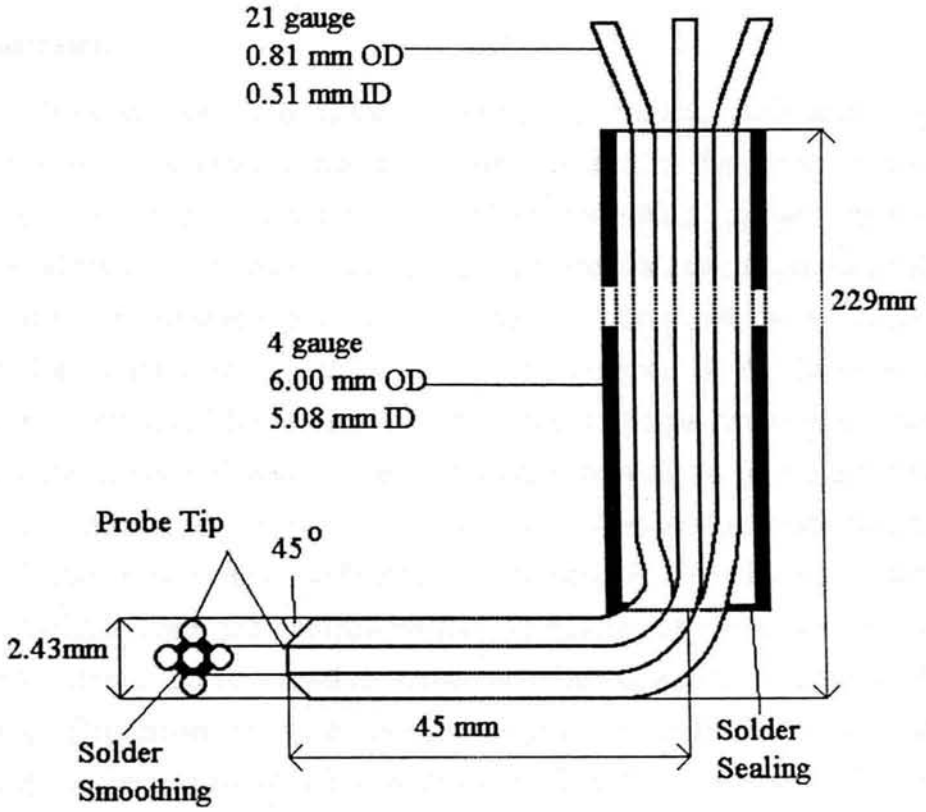

Figure 3.20 - 5-Hole Probe Geometry

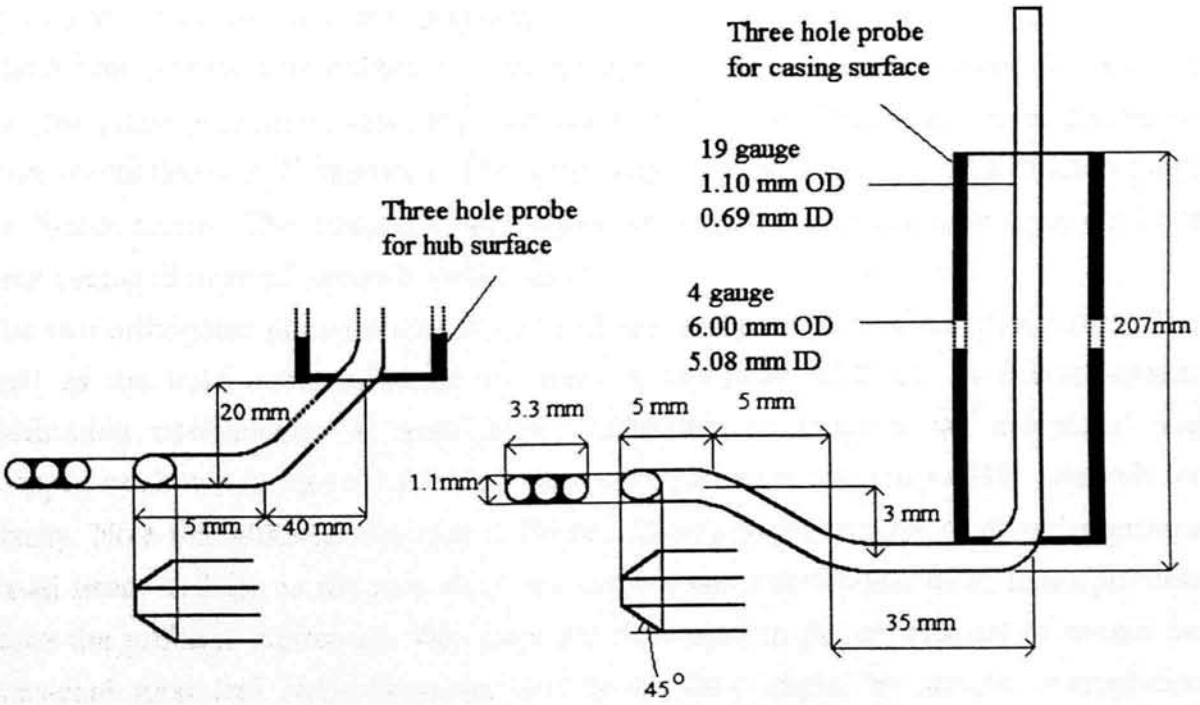

Figure 3.21 - 3-Hole Probe Geometries

Probe Calibration

The 3 and 5-hole probes were calibrated using an existing calibration rig. The rig consisted of a two axis traverse which allowed rotation of the probe in two mutually orthogonal planes, using automated computer controlled stepper motors with a resolution of 66 steps per degree. A centrifugal fan provided the required air flow which enveloped both the reference pitot static probe and the probe being calibrated. The geometry of the calibration rig was such that the position of the probe tip remained constant in the airstream. The pressures of the 7 holes (5-hole probe plus reference total and static) were measured with a single pressure transducer and a scanivalve. This eliminated any calibration errors that could exist if 7 individual transducers had been used. The 5-hole probe was calibrated at an airspeed of ~90m/s which was the maximum available from the centrifugal fan. The range of velocities measured in the duct were 55-120m/s. There would therefore be potential errors as a result of Reynolds number effect. Discrepancies have been assessed to be up to 5% of the true dynamic pressure in the Reynolds number range $2x10^3$ to $20x10^3$ based on probe tip diameter, Dominy *et al* (1992). The operational Reynolds number range of the probe was $8.9x10^3$ to $19.3x10^3$ with the calibration taken at $14.5x10^3$. Therefore errors are estimated to be up to 2.5% of the true dynamic pressure.

The 5-hole probes were calibrated over a range of ±30° in the pitch plane and ±28° in the yaw plane (maximum yaw range obtainable with calibration rig and probe geometry) with points taken at 2° intervals. This cone angle covered the typical calibration range for 5-hole probes. The pressures were logged using a P.C. and analogue input card and time averaged over 0.5 seconds (500 points).

The two orthogonal planes nominally termed yaw and pitch are defined in figure 3.22 as well as the hole numbers which are used in equations (3.2-3.6) to define various calibration coefficients. At each angle, calibration coefficients are calculated and mapped as shown in figure 3.23 which shows the pitch and yaw map at 10° intervals for clarity. Note that although the map in figure 3.23 is asymmetric due to manufacturing a small head, as long as the map lines are smooth and continuous, there is no problem since the probe is calibrated. The maps are then used in the experiment to obtain the corrected total and static pressures and hence flow angle, by simple interpolation methods. Other types of probes are used in turbomachinery applications e.g. wedge and

prism probes, since they can access between blade rows easily through small inspection holes as they have no forward pointing sting.

$$\text{Pitch angle Coefficient, } Cp_{pitch} = \frac{p_2 - p_3}{p_1 - p_{av}} \quad \{3.2\}$$

$$\text{Yaw angle Coefficient, } Cp_{yaw} = \frac{p_4 - p_5}{p_1 - p_{av}} \quad \{3.3\}$$

$$\text{Stagnation Pressure Coefficient, } Cp_{total} = \frac{P_o - p_1}{p_1 - p_{av}} \quad \{3.4\}$$

$$\text{Dynamic Pressure Coefficient, } Cp_{static} = \frac{P_o - p}{p_1 - p_{av}} \quad \{3.5\}$$

where p is the free stream static pressure and p_{av} is the mean of the pressures measured by the side holes, that is:

$$p_{av} = \frac{p_2 + p_3 + p_4 + p_5}{4} \quad \{3.6\}$$

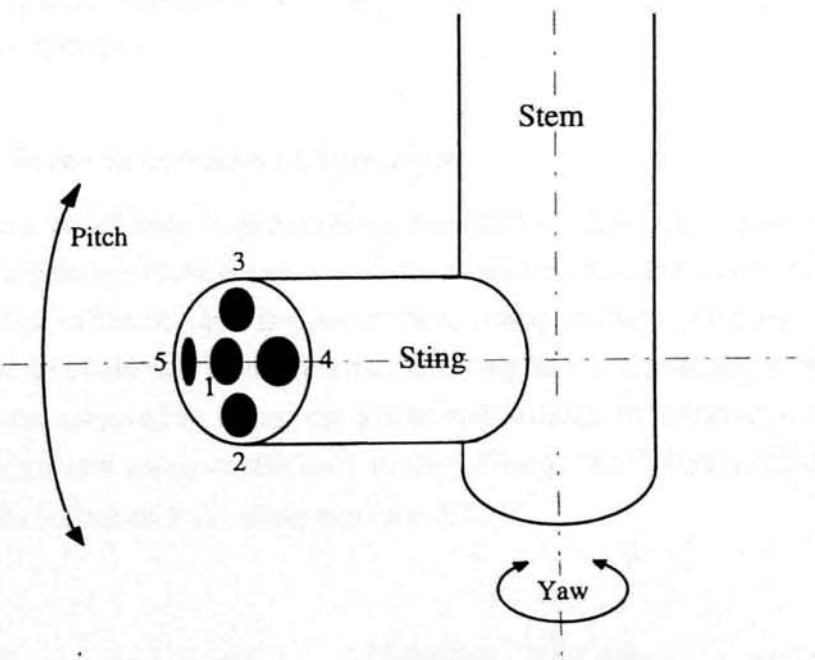

Figure 3.22 - 5-Hole Probe Angle and Hole Nomenclature

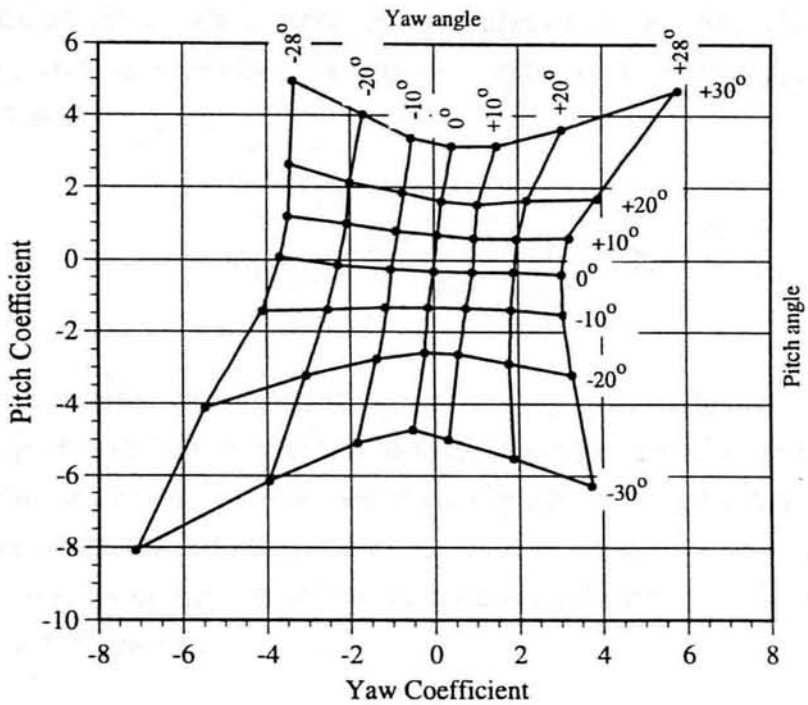

Figure 3.23 - 5-Hole Probe Yaw and Pitch Calibration Map

The same calibration procedure and mapping is carried out for the 3-hole probes but only in the yaw direction.

3 and 5-Hole Probe Data Matching Procedure

Due to the duration of tests (approximately 3 hours for 5 hole area traverse), variations in atmospheric pressure often occur, especially as if often the case, the 3 and 5 hole tests are performed on different days. Because of this, it was necessary to match or adjust the three data sets to avoid any discontinuities occuring at the interfaces of the combined results. This was achieved by taking the 5 hole bulk data as the reference set and scaling both 3 hole data sets using coefficients to this. Firstly, the 3 hole total pressures are converted to a coefficient form using equation 3.7.

$$(Cp_o)_{3hole} = \frac{(P_{o(in)})_{3hole} - (P_{o(l)})_{3hole}}{(P_{o(in)} - p_{(in)})_{3hole}} \qquad \{3.7\}$$

where (l) denotes local plane quantities and (in) the inlet quantity.
Then substituting the 3 hole coefficient just calculated and the 5 hole data inlet pressures measured, into equation 3.8, the new scaled value of $P_{o(l)new}$ at the local plane can be found.

$$(Cp_o)_{3hole} = \frac{(P_{o(in)})_{5hole} - (P_{o(l)new})_{3hole}}{(P_{o(in)} - p_{(in)})_{5hole}} \qquad \{3.8\}$$

Another source of error which required correction was probe alignment, i.e. ensuring that all three probes (5 hole, 3 hole hub and casing probes) are all aligned in the same direction at the start of the test. The mean flow direction at the interfaces of the 3 hole data sets were calculated and compared to the value at the respective interface of the 5 hole data set. Any neccessary correction was then made to the 3 hole data sets in order to match the bulk 5 hole set.

Pitot Probes

Pitot or total pressure probes are used to measure the stagnation pressure of the flow, i.e. the pressure of the flow if it were brought to rest isentropically. Various shaped pitot probes with one or two separate heads were used in the duct for either boundary layer or area traversing where a multiple holed probe would have been too intrusive and unnecessary. The pitot probes used to measure the boundary layers were made from steel hypodermic tubing of approximately 1mm outer diameter which was then flattened to approximately 0.5 mm outer diameter so that they could measure the boundary layer profile to a higher resolution. The example shown in figure 3.24 was the type used to measure the boundary layer on the strut surface. For accurate determination of the probes' positions (boundary layer and multiple holed probes) and also to prevent any damaged cause if the traverse were to drive them into the walls, a simple electrical contact circuit shown in figure 3.25 was used. When the slowly approaching probe makes contact with the metalic wall or surface, the base of the transitor is forced from 0 to 5V; this difference being sensed by the logging card and the traverse stopped. The non-metalic struts had thin strips of foil adhered to their surfaces to allow the electrical

contact circuit to operate (shown in figure 3.24). Pitot probes were used at the inlet plane (see figures 3.14 and 3.16), and at planes A1, B1 and B2 (see figure 3.17).

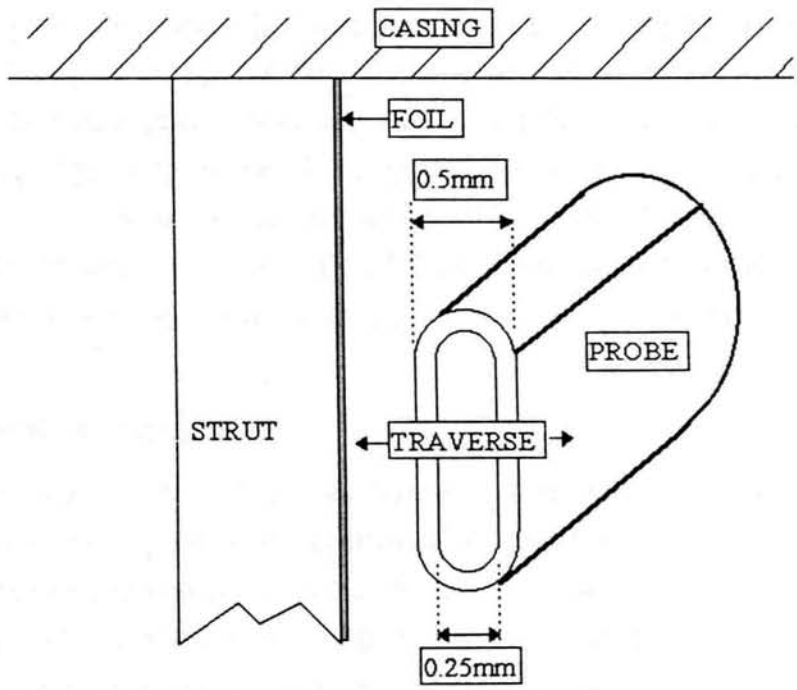

Figure 3.24 - Strut Boundary Layer Probe and Traverse

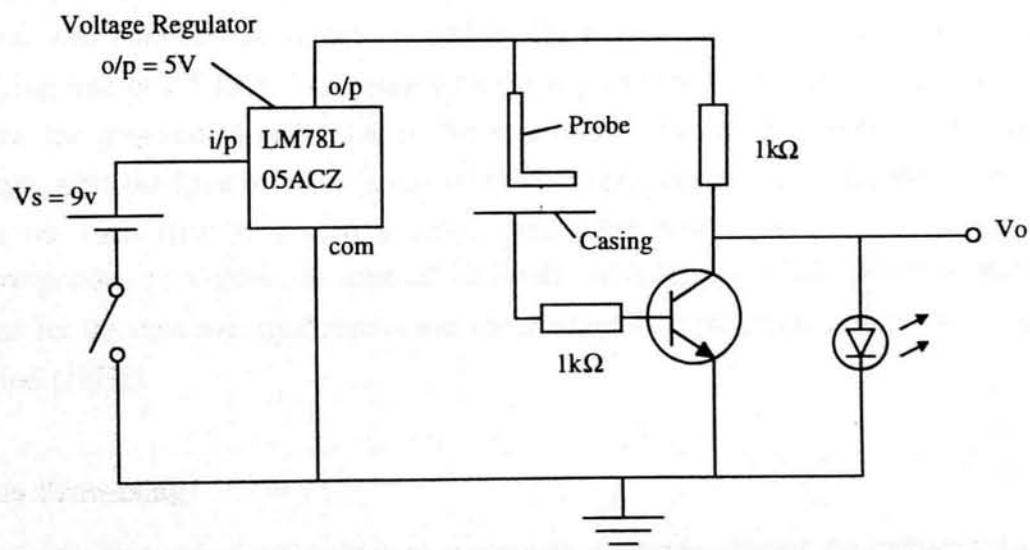

Figure 3.25 - Probe Wall Contact Circuit

3.3.6 Hot-wire

The hot wire used to measure the inlet turbulence conditions of the new inlet and turbulence grid was a single hot wire with its axis aligned perpendicular to the flow (DISA, probe type 55P11). The flow was assumed to be isotropic and purely axial in direction. The measurements were taken 15mm (half an IGV chord) downstream of the IGV trailing edge (inlet plane -1) using the 3-axis traverse. This allowed full area traversing in the true radial and circumferential directions. The hot wire control system was a DISA 55M01 main unit with a 55M10 CTA standard bridge. A DISA 55D25 auxiliary unit allowed signal processing including low and high pass filtering.

3.3.7 Data Control and Acquisition

The stepper motors which drove the traverses were driven by Digiplan PK3 stepper motor drivers, the step rate being controlled by a FORTRAN program which drove the motors at the maximum rate they could before they stalled. This and the data capturing system were all controlled by a 486 IBM desktop P.C. utilising a 66Mz processor. The pressures which were converted to voltages using the previously described pressure transducers, were then logged by the P.C. by means of a Strawberry Tree ACjr-12 analogue to digital (A/D) integrating board, which could sample up to 10,000 data points per second (10 kHz), if the bit resolution was reduced to 9. The input / output board was operated at 12 bit resolution (±0.024%) on a ±5V range and maximum logging rate of 2.5 kHz. The logging rate was governed by the time delay necessary to allow the pressure to settle due to the scani-valve switching between ports, the tube length, plus the time to allow a sensible time averaging period. Altogether, this meant that the total time to record a single data point took approx. 3.5 seconds which corresponded to a total run time of ~3 hours for a typical 5 hole traverse. Each data point for the time averaged results was the average of 1000 points taken over a 1 second period (1kHz).

3.3.8 Data Processing

Computer programs were written to assist with the processing of the gathered data. The raw data files were first converted using the previously obtained calibration coefficients of the various pressure transducers, into raw pressures, e.g. each hole of the five hole

probe data set. The exact procedure is described in detail by Treaster *et al* (1979) and is briefly discussed here.

Firstly, the 5 pressures read from the 5 separate holes of the probe are converted into values of pitch coefficient, Cp_{pitch}, and yaw coefficient, Cp_{yaw} using equations 3.2 and 3.3. These values are then interpolated onto the graph of Cp_{pitch} vs Cp_{yaw} (e.g. figure 3.23) to obtain the actual pitch and yaw flow angles. The static pressure coefficient, Cp_{static}, can then be found by interpolating onto the Cp_{static} vs pitch angle graph which has lines of constant yaw angle. The same method is used to obtain the total pressure coefficient, Cp_{total}, and then by using equations 3.4 and 3.5, the actual static and total pressure can be calculated.

Finally, by using Bernoulli's, the magnitude of the velocity can be found, equation 3.9.

$$V = \sqrt{\frac{2}{\rho}}(P_o - p) \qquad \{3.9\}$$

The 3 and 5 hole data sets were then matched together using the procedure previously described. When matching the 3 and 5 hole data together, it was necessary to first plot the 5 hole data to see which, if any, of the data rows near the hub or casing needed to be removed due to wall effects. This could either be due to flow acceleration through the small gap formed as the probe nears a surface and hence giving an artificially low static pressure, or it could be due to either hole 2 or hole 3 (see figure 3.22) entering the boundary layer and therefore once again giving false information. Either way it was easy to detect since a row of secondary flow vectors would be all pointing towards the nearing wall. Once the correct 5 hole data set was decided upon, the 3 hole data sets had to be cropped to ensure there was no overlap and hence discontinuities at the interfaces. At certain slots within the ducts when swirl was introduced, due to the probes' and ducts' geometries, the grafting of the two 3 hole sets of results onto the 5 hole set was made difficult. This meant that a small number of data points in areas of the 3-hole/5-hole interface could not be included in the final data sets. e.g. see figure 4.46.

Chapter 4

Experimental Investigation and Results

4.1 Scope of Investigation

The results presented here are part of a continuing research program to investigate the fluid flow phenomena within diffusing swan neck ducts. The aims of this experimental investigation were to make various detailed measurements within the duct in order to validate the cfd code M.E.F.P. with which future ducts could then be designed, and also to gain a better understanding of the flow physics within such duct geometries. This initially meant measuring wall static pressures along the hubs and casings of the two ducts, but first a new inlet had to be designed to ensure near uniform radial total pressure and velocity gradients at entry to the working section. Area total pressure measurements were made at various axial planes within both ducts and compared directly with the cfd results. It was observed that the cfd predicted the local static pressure peaks measured in the phase 1 duct better than it did the more severely locally diffusing phase 2 duct flow. Surface flow visualisation on the phase 2 duct produced some strange flow patterns in areas of the duct, in particular, on and around the struts. Total pressure measurements in the same part of the duct (strut casing region), showed a region of low total pressure and also high flow angles which occasionally exceeded the range of calibration. Together these results prompted more detailed unsteady static pressure measurements in and around the struts. These results confirmed the presence of an unsteady separation which then led the investigation back to the cfd results to see if any evidence of it was predicted numerically. Other investigations were also made such as the effect of swirling flow within the ducts on the duct loss; these results and others are contained in this chapter.

4.2 Inlet Conditions

As detailed in chapter 3, a new inlet was designed for the test rig in order to produce a near uniform radial total pressure and velocity gradient at the inlet plane, in order to simplify the analysis of the working section flow. The new inlet also had to produce a steady casing boundary layer at the inlet plane which the previous did not achieve.

4.2.1 Inlet Total Pressure Profile

A radial traverse at plane -1 (figure 3.14, pg 55) with the new inlet was performed at mid inlet guide vane (IGV) pitch with the IGV's set at zero degrees swirl, using a small (1.1mm outer diameter) pitot probe, to measure the total pressure variation. The results of which can be seen in figure 4.1.

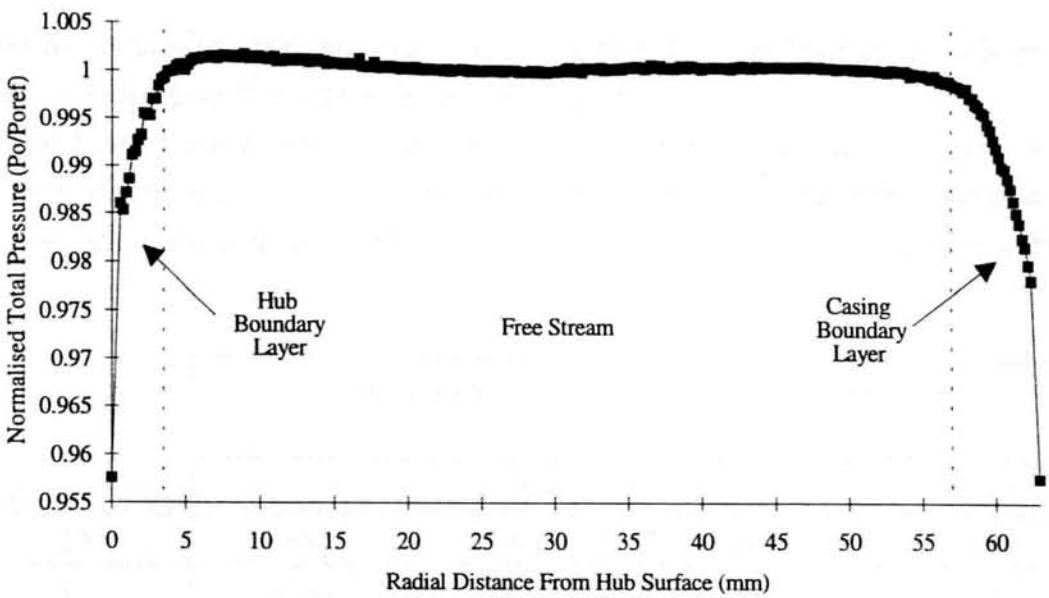

Figure 4.1 - Radial Total Pressure Distribution (Inlet -1)

As can be seen from figure 4.1, the radial free stream total pressure variation is very small, ±0.18% of absolute total pressure or ±90 Pa. The reference pressure, Po_{ref}, was the total pressure measured with a single pitot probe at mid span, approximately 45mm upstream of the IGV leading edge.

The reasonably symmetrically shaped hub and casing boundary layers together, occupy approximately 15% of the inlet passage height. Table 4.1 contains the displacement thickness, momentum thickness and shape factor for the new and previous inlet. The hub boundary layer properties calculated for the new inlet used the peak velocity as being the free stream velocity which was a slightly different from the free stream value used for the casing boundary layer. Important to note is the reduction in momentum thickness and corresponding increase in shape factor of the new inlet compared to the previous, indicating a decrease in the turbulence levels within the boundary layers.

Typical shape factor values for turbulent and laminar boundary layers are as follows:

Laminar boundary layer	2.3 - 3.5
Turbulent boundary layer	1.3 - 1.8
Separating turbulent boundary layer	1.8 - 2.2

[C.I.T]

Turbulent boundary layers are less likely to separate due to better mixing with the free stream which acts to re-energise the boundary layer.

The pitot probe could only measure to within 0.55mm (probe radius) of the hub and casing surfaces, and hence the two points at 0 and 63 mm have been calculated and plotted using the known mean inlet dynamic head (from measured wall static pressures).

	New Inlet		Previous Inlet	
	Casing	Hub	Casing	Hub
δ^*	0.92	1.11	0.86	0.90
θ	0.60	0.43	0.68	0.65
H	1.52	2.59	1.27	1.38

Table 4.1 - New and Previous Inlet Boundary Layer Properties

4.2.2 Hot Wire Turbulence Measurements

The hot wire turbulence results shown in figure 4.2. were taken over one inlet guide vane pitch. The turbulence level rises to 15% in the hub and casing boundary layers; 4% in the IGV wakes and the free stream turbulence does not exceed 2%. The relatively low free stream turbulence arises because the turbulence is created part way through the inlet where the velocity is relatively low and thus when the bulk flow is accelerated through the contraction, the turbulence in percentage terms reduces. Moving the turbulence grid downstream in order to increase the free stream turbulence levels would distort the inlet total pressure profile due to the non-uniform radial flow velocity, making analysis of the downstream flow more difficult.

4.4 Inlet Ground Vortex

When surface flow visualisation was performed in the duct, unexpected flow patterns appeared on the casing surface of the duct, immediately downstream of the first bend. Initially this was thought to be due to horse shoe vortices shed off of the inlet guide vanes, however when the IGV's were removed, the flow patterns still remained (figures 4.3 & 4.4), with and without struts. It was then postulated that, what if an inlet ground vortex as commonly appears at the engine inlet of gas turbine propelled aircraft and at the inlet of open circuit wind tunnels, was occuring and which could possibly be the cause of this flow phenomena.

When some aeroplanes begin their take off run, a veritable tornado often develops between the engine inlet and the runway causing dust and debris to be sucked off of the floor by the low pressure core and ingested by the engine. This inlet ground vortex not only causes problems of foreign object damage (FOD) through ingestion of solid particles, but it can also cause a degragation of compressor performance due to non-uniform inlet flow conditions. This transient distorted flow field often appears at the inlet to wind tunnels which can often be the cause of flow unsteadiness. Figure 4.10 shows a diagram of such an inlet ground vortex.

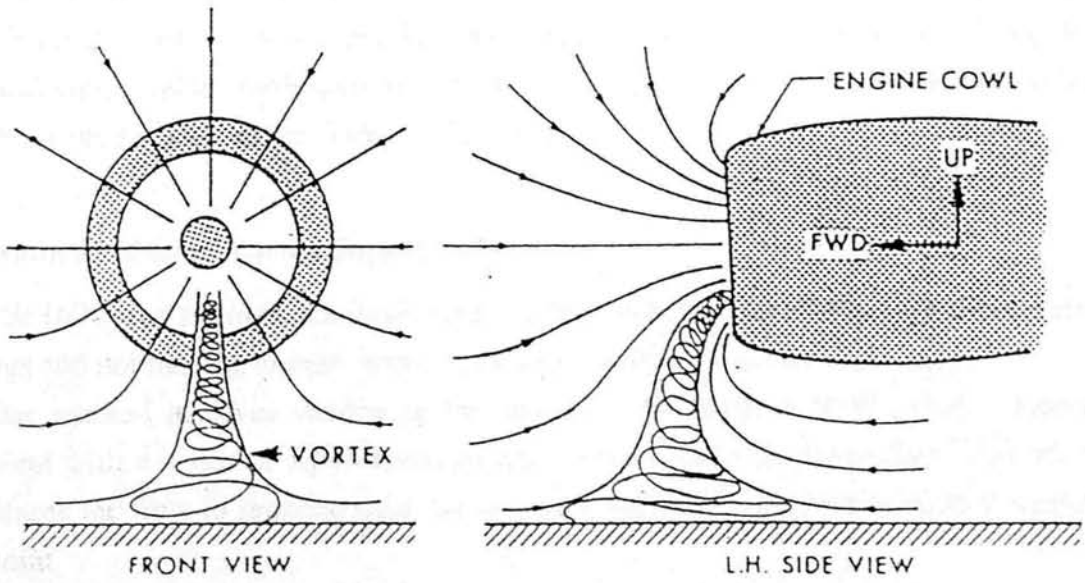

Figure 4.10 - An Engine Inlet Ground Vortex [Loughney (1971)]

To investigate the inlet for signs of of this flow phenomena, flow visualisation in the form of smoke was used. Very quickly a meandering inlet vortex became apparent with a core of approximately 50mm diameter. Inlet vortices have a tendency to meander in this way especially if as is the case , the inlet is not in close proximity of the ground.

4.4.1 Mechanisms of Inlet-Vortex Formation

In order to suppress or even eliminate the inlet vortex it is neccessary to understand the mechanisms of it's formation. De Siervi *et al* (1982) documented an experimental and theoretical study on the mechanisms of inlet-vortex formation using a water tunnel and hydrogen-bubble flow visualisation for the experimental study, and a secondary flow approach for the theoretical study. They found that there were two mechanisms for the formation, one being the intensification of ambient vorticity, Shin *et al* (1986), the second being linked to the variation in circulation along the length of an inlet. This second mechanism is more difficult to understand but it is basically due to the separation of viscous 3-D boundary layers on the outer surface of the inlet. A comprehensive explanation is given by De Siervi *et al* (1982). Although their experiments proved that a boundary layer such as that found on the floor in the vicinity of an inlet was not needed to produce an inlet vortex, it is more than often the prime cause in test rigs since they tend to be aligned in this way. In this case it is the combination of the two opposing floor boundary layers at the stagnation point which meet and spiral upwards causing the vortex, Colhour *et al* (1971). This was assumed to be the prime cause in the Durham SND rig case.

4.4.2 Methods of Inlet-Vortex Suppression

The following methods are those used to suppress inlet-vortices found on stationary test rigs and not moving aircraft inlets and are discussed by Colhour *et al* (1971).

One method involves ventilating the surface in the vicinity of the vortex stagnation point with a series of small holes ejecting perpendicular to the surface. This blowing causes the flow to separate from the wall thus preventing the formation of a stagnation point.

Another method involves blowing parallel to the surface so as to induce a primary flow in one direction which eliminates the converging flow pattern which would otherwise occur and form a vortex.

By far the simplest and most effective solution which is used employs the use of an asterisk shaped fence as shown in figure 4.11. The intersection of the arms was placed on the floor in the vicinity of the observed vortex stagnation point. The rotational flow near the ground plane in the boundary layer cannot form a stagnation point because of the fence. Instead, the flow is forced to separate from the ground plane and up into the inlet without forming a vortex. The various arms of the fence also disburb the circular flow in the ground plane, thus inhibiting vortex formation.

This method was tried and optimised so that with the final solution (figure 4.11), no inlet ground vortex using smoke was observed. However, upon repeating the flow visualisation test with the vortex supressor in place, the casing flow pattern still occured. The fences were 0.28m high and the distance from the ground to the base of the inlet was 0.95m.

Evidence later in this chapter will show this to be due to an unsteady casing surface flow separation.

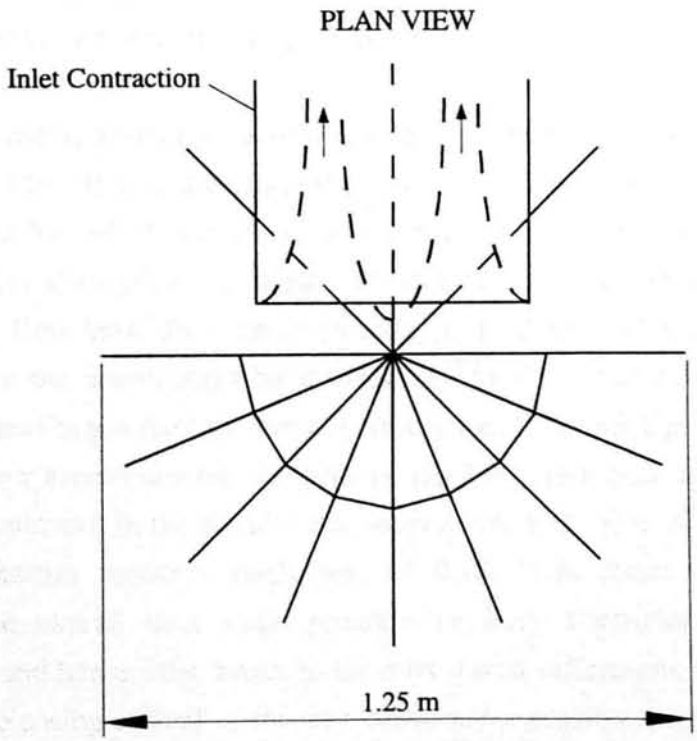

Figure 4.11 - Inlet Ground Vortex Suppressor

4.5 Static Pressure Development

Static pressure measurements have been made along the hub and casing surfaces of both phase 1 and 2 ducts for various combinations of inlet guide vanes and struts. In addition to this, measurements on the phase 1 duct have been made at varying swirl angle in order to investigate the effect of inlet swirl on duct static pressure recovery.

4.5.1 Phase 1 Duct with Zero Swirl

Figure 4.12 shows the static pressure development through the phase 1 duct for the two cases, with and without inlet guide vanes. The static pressure recovery coefficient, Cp (eqn. 2.1) was non-dimensionalised by inlet dynamic head, the nominal inlet plane being situated half an inlet guide vane chord, downstream of the IGV trailing edge (16mm, x/h = -1.977).

The static tappings on the casing surface, approximately half an inlet passage height upstream of the casing bend, show that there is an upstream influence of the bend and the flow has already accelerated to 10% above the inlet dynamic head at this axial position. Results presented later in this chapter will show that the flow is influenced by the bend approximately one inlet passage height upstream.

The flow on the casing surface accelerates to a peak suction Cp value of -0.4 at an axial position of zero (the start of the geometric bend). The casing flow then immediately undergoes a diffusion which continues until almost the duct exit; a small amount of acceleration occurs at an x/h = 4.5 which is where the duct just enters the parallel exit section. The hub flow basically behaves in an opposite sense to the casing flow. Once again it adjusts to the downstream bend before the bend is actually reached. The first bend is concave and hence the flow initially decelerates to a peak Cp of 0.45 at x/h = 1. From here the flow accelerates for two passage heights before once again undergoing a diffusion to the duct exit in the parallel exit section where the duct achieves an average overal static pressure recovery coefficient of 0.46. Note there is no measurable difference in the overall duct static pressure recovery coefficient when the duct contained IGV's and hence inlet wakes to the duct. Local differences in the value of Cp occur, e.g. on the casing surface of the first bend, and a possible explanation for this is discussed in chapter 5.

Firstly examining the hub flow, it can be seen that as the swirl angle increases, the point at which the diffusion occurs as a consequence of the concave bend, shifts downstream, closer towards x/h = 0. Increasing swirl angle also decreases the magnitude of peak diffusion at x/h = 1, as expected. The casing surface flow at 15 degrees swirl is similar to that at zero degrees, there being only a small reduction in peak velocity at the bend. At 30 degrees however, the magnitude of peak suction is significantly reduced on the first bend which will be shown to be beneficial in terms of losses for the casing flow. This benefit is offset however by the worsening flow on the hub as a consequence of high swirl causing thickening boundary layers and even flow separation. Table 4.2 summarises the static pressure recovery coefficient for the phase 1 duct at varying swirl angle.

IGV Angle (degrees)	Cp
0	0.46
15	0.43
30	0.42

Table 4.2 - Summary of Phase 1 Static Pressure Recovery Coefficient

4.5.3 Phase 2 Duct with Zero Swirl

Figure 4.14 below shows the static pressure development through the phase 2 duct when struts are not present in the duct. The general shape of the curves are similar to those shown in figure 4.12 with the non-inlet wake case giving slight local increases in peak velocities as in the phase 1 case. The difference in overall pressure recovery for the two cases, with and without IGV's was found to be within experimental error. The overall duct pressure recovery coefficient was measured to be 0.42.

the two struts appear to be similar, as expected since the flow is axial and has no inlet wakes.

Figures 4.18 and 4.19 show rms contours of static pressure coefficient. The rms is normalised against mean inlet dynamic head. These results can only be used qualitatively against other similar rms Cp plots shown in section 4.6.2 since the results were measured using long hypodermic tubes which will attenuate the signal by an estimated order of 50%, Irwin *et al* (1979).
To show quantitatively the flow around the two struts, figures 4.20 and 4.21 plot the strut Cp distribution along approximate stream lines. The exact position of the rows were shown in chapter 3, figure 3.12.

Figures 4.20 and 4.21 show there is a slight difference between the two separate strut flows, the main differences occuring around the leading edge and towards the casing.
This is not surprising as the leading edge is radius is very small and therefore exact positioning of static tappings from strut to strut in a region where the flow is known to be rapidly changing, will inevitably lead to differences in strut to strut readings. Added to this is the problem of ensuring both struts are aligned in the same axial direction. Both struts' hub flows appear to show a constant velocity along the strut chord at this spanwise position. Their near casing surface flows show rapid accelerations producing maximum velocities at between 2 and 10 percent chord of Cp's upto -0.9 which is the same value measured with the casing surface static tappings slightly ahead of the struts' leading edge.

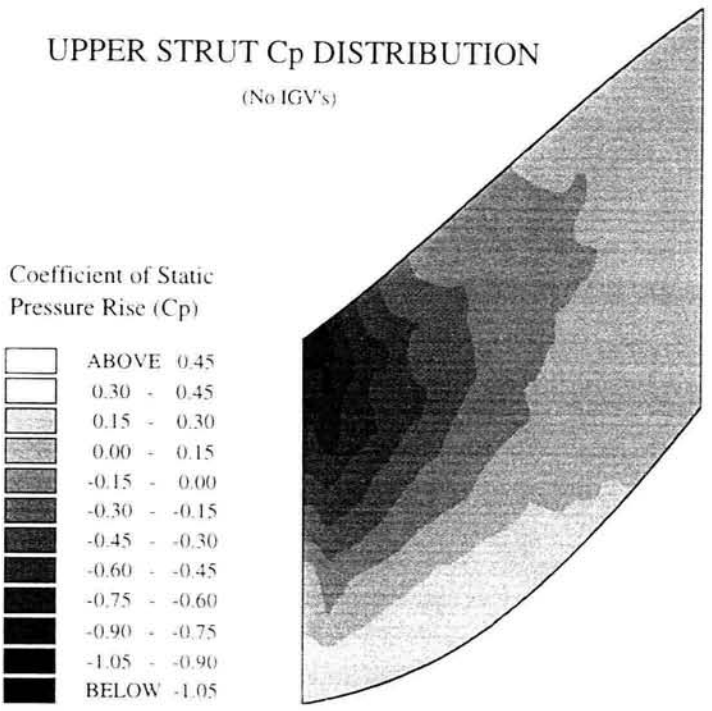

Figure 4.16 - Cp Contours (Upper Strut, No IGV's)

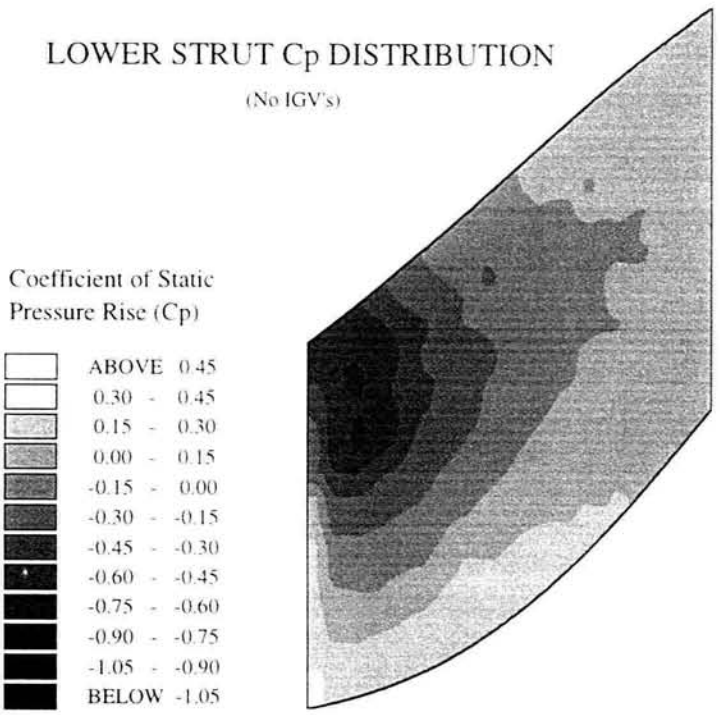

Figure 4.17 - Cp Contours (Lower Strut, No IGV's)

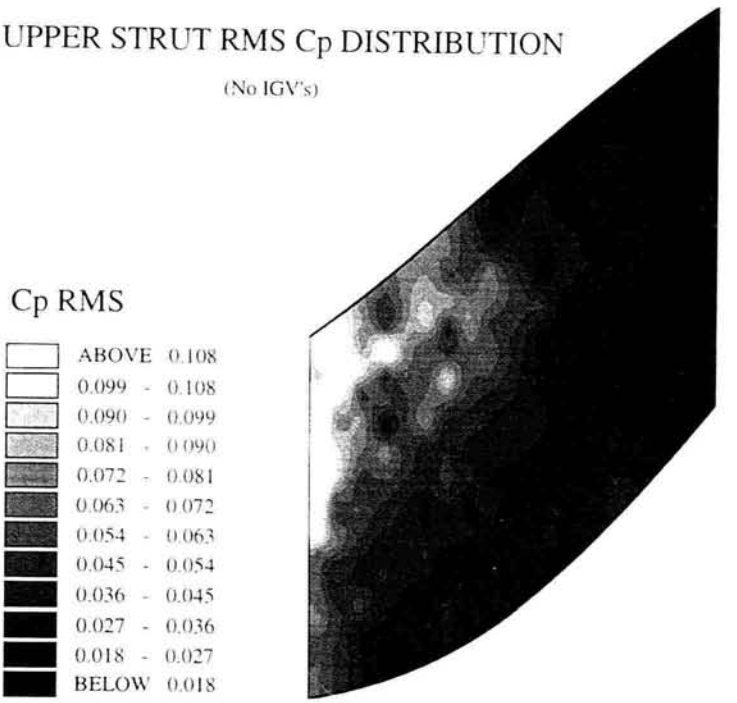

Figure 4.18 - Upper Strut Cp RMS Contours (No IGV's)

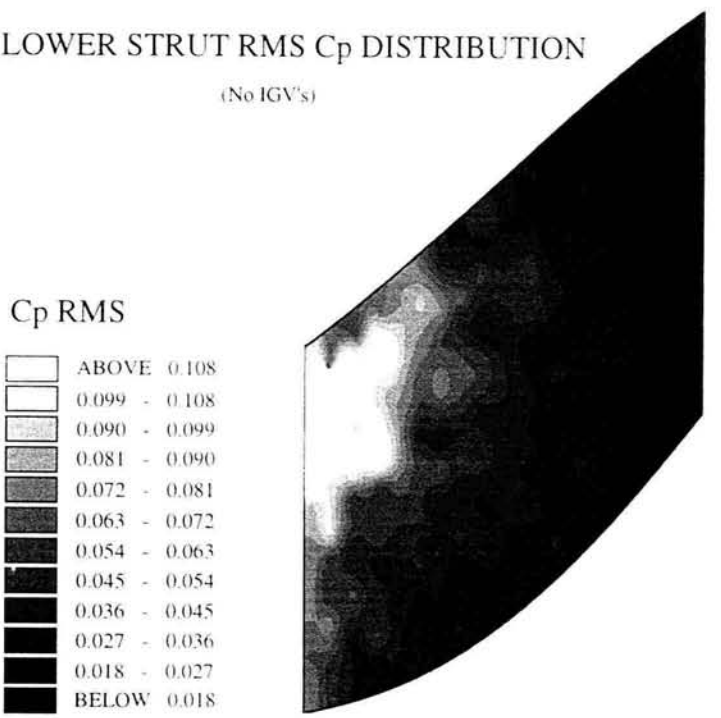

Figure 4.19 - Lower Strut Cp RMS Contours (No IGV's)

4.6.2 Strut Wake Interaction (with IGV's)

The relative circumferential position of the inlet wake to the strut leading edge can be changed to investigate the effects of IGV wakes and strut interaction.

Figure 4.22 shows the definition of IGV to strut position used in this section. A figure titled 'upper strut, igv at 10% strut pitch' implies that the upper strut has an igv wake almost incident to it's leading edge as shown in figure 4.22. In this case, because there are 34 IGV's and only 26 struts, with an igv wake incident (10%) on the instrumented side of the upper strut, the next igv wake is also incident approximately 10% on the instrumented side of the lower strut. In this relative position it is possible to have two igv wakes passing through the instrumented strut passage. The case of 40% clearly only achieves one igv wake within the passage.

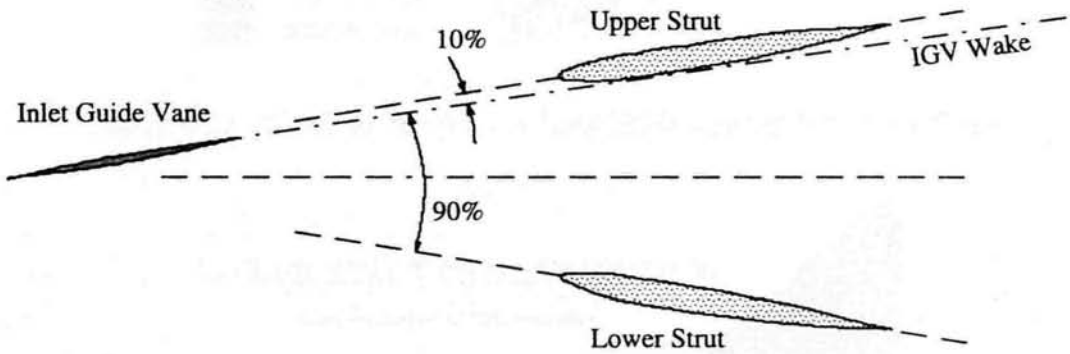

Figure 4.22 - IGV Wake Notation

Both figures 4.23 and 4.24 show that the shape of the Cp contours are similar to those of figures 4.16 and 4.17. Figures 4.25 and 4.26 show the Cp rms contours when an igv wake is incident on each instrumented strut surface. These figures show that despite the slightly higher turbulence levels present in the igv wakes, the rms on the strut surface is lower than without igv wake impact.

Finally figures 4.27 and 4.28 present the approximate stream line flow distribution across the span of the strut. They show that the magnitude of peak velocity at 5-10% chord has been reduced to 60% of it's value (-0.53 c.f. -0.90) in the near casing region.

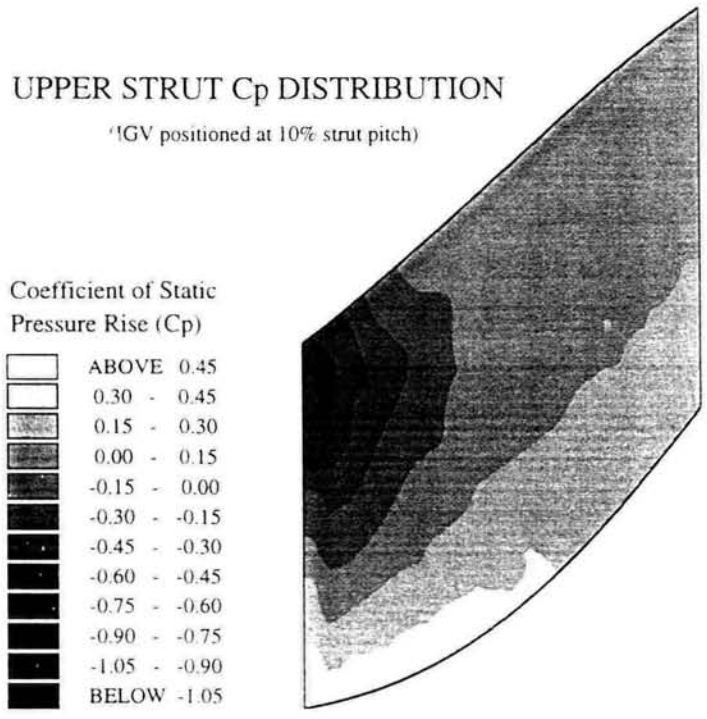

Figure 4.23 - Cp Contours (Upper Strut, IGV wake at 10% Strut Pitch)

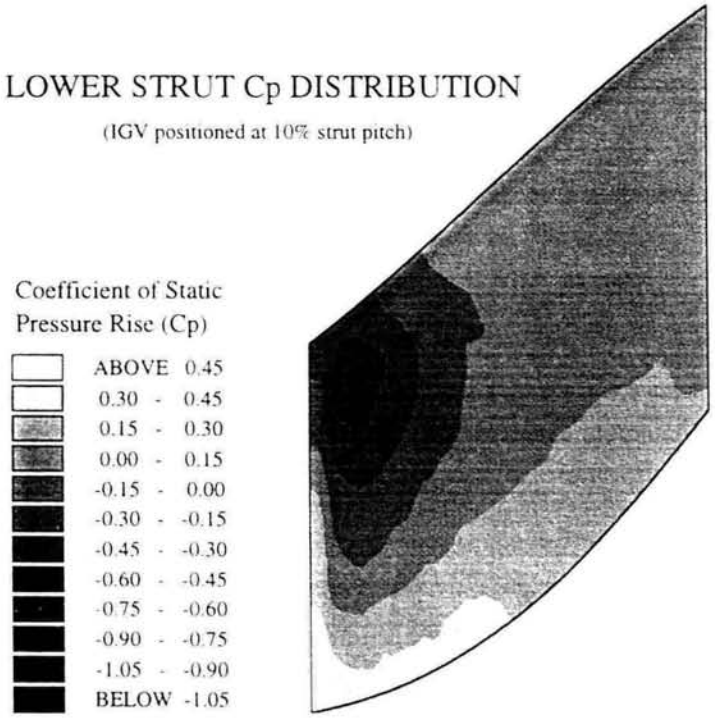

Figure 4.24 - Cp Contours (Lower Strut, IGV wake at 10% Strut Pitch)

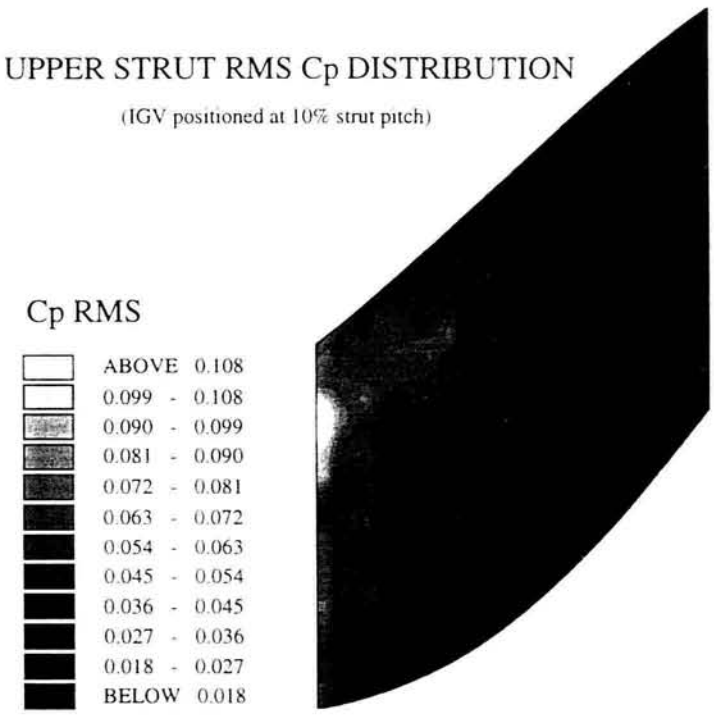

Figure 4.25 - Upper Strut Cp RMS Contours (IGV at 10% Strut Pitch)

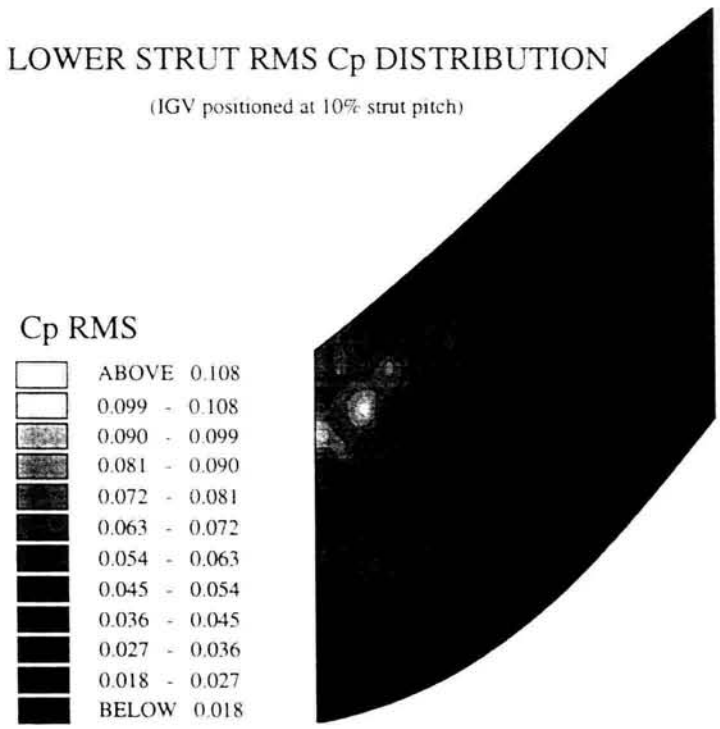

Figure 4.26 - Lower Strut Cp RMS Contours (IGV at 10% Strut Pitch)

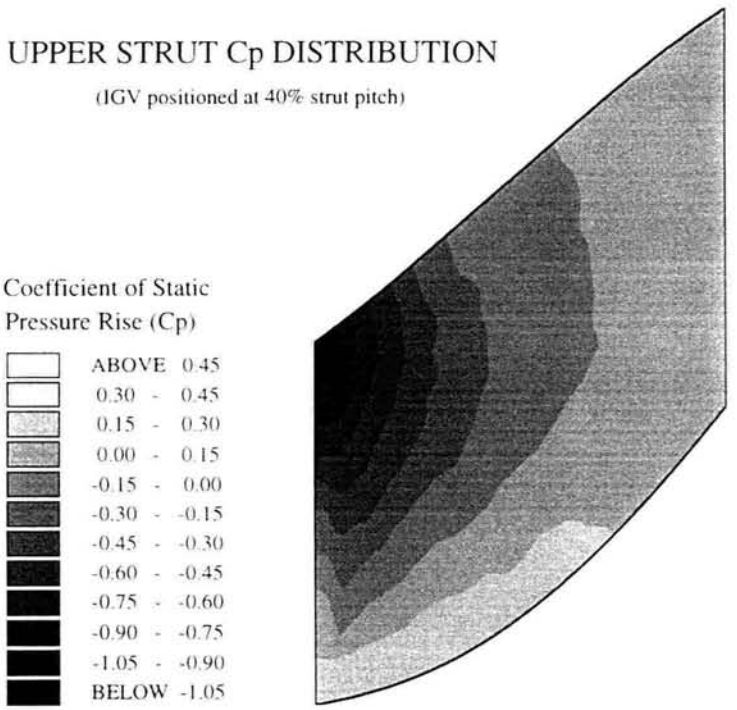

Figure 4.29 - Cp Contours (Upper Strut, IGV wake at 40% Strut Pitch)

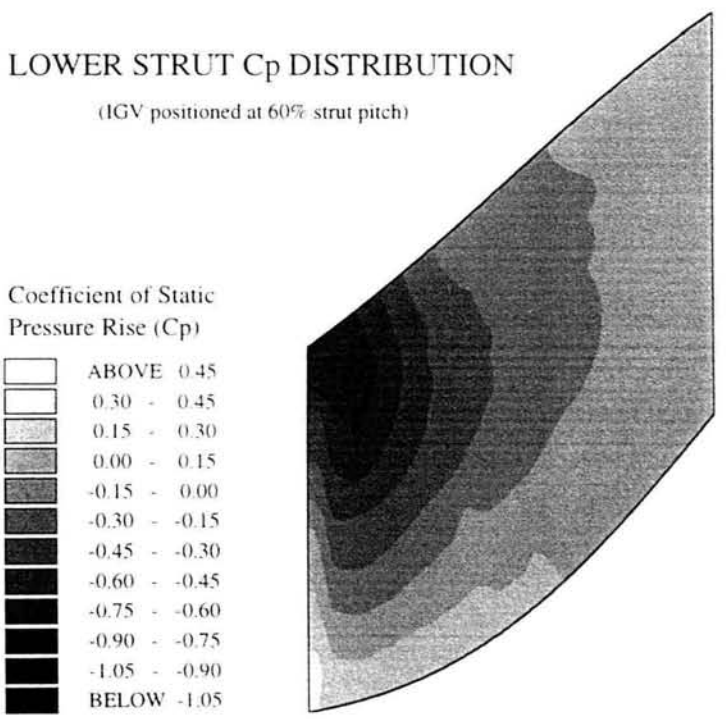

Figure 4.30 - Cp Contours (Lower Strut, IGV wake at 60% Strut Pitch)

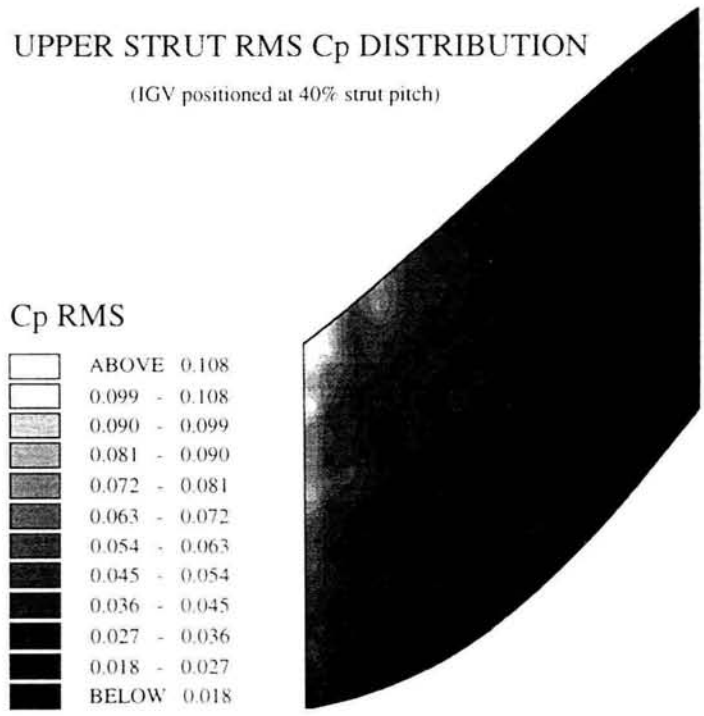

Figure 4.31 - Upper Strut Cp RMS Contours (IGV at 40% Strut Pitch)

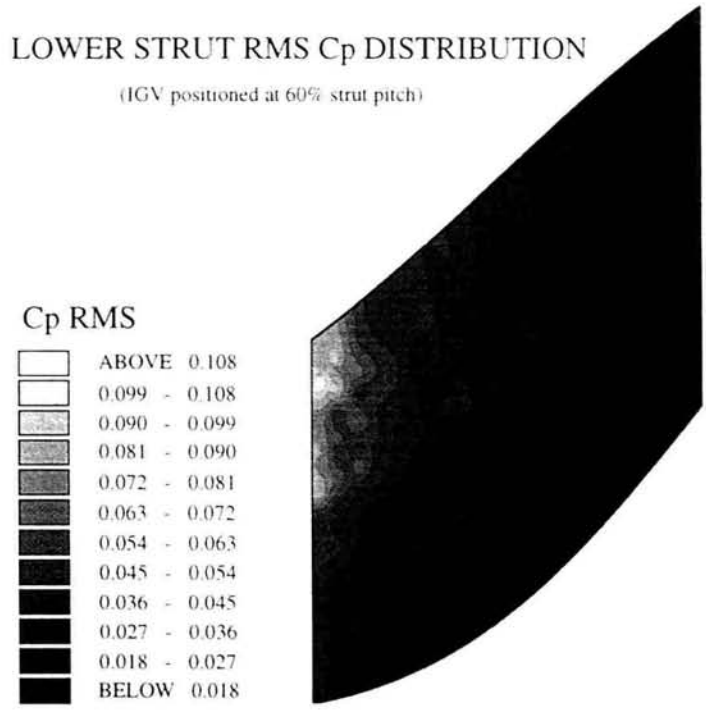

Figure 4.32 - Lower Strut Cp RMS Contours (IGV at 60% Strut Pitch)

Figures 4.29 and 4.30 show that once again the shape of the Cp contours are the same as for the other inlet wake positions. Figures 4.31 and 4.32, the Cp rms contours, show that the level of unsteadiness is about the same as when the inlet wake was incident on the strut surface (figures 4.25 & 4.26), which is lower than for the case without inlet wakes (figures 4.18 & 4.19). Figures 4.33 and 4.34 show that the magnitudes of peak velocities and accelerations are greater with wakes at 40% and 60% strut pitch compared to the case without wakes (figures 4.20 & 4.21) or with wakes at 10% pitch (figures 4.27 & 4.28).

4.7 Phase 1 Area Traverses

Figures 4.35-4.46 contain the results of the combined 3 and 5 hole probe traverse measurements at planes -1,3,6 and 11 in the phase 1 duct at 0,15 and 30 degrees inlet IGV swirl angles. At each plane and swirl angle, five plots are presented. They are, total pressure, static pressure, yaw angle and pitch angle contours and also secondary velocity vectors. The yaw, pitch and secondary velocity vectors were calculated by first calculating the mean flow direction for the particular data set, i.e. 3 hole hub, 3 hole casing or 5 hole bulk flow, and then each flow angle calculated and plotted relative to the mean flow direction.

Zero Degrees Swirl

Figure 4.35, the inlet plane (-1) at zero swirl shows the thin symmetrical inlet wake along with hub and casing boundary layers. The total and static pressures are almost uniform across the bulk flow since the inlet was designed to achieve a near uniform radial inlet total pressure and velocity distribution. Note, although it was possible to traverse over more than one pitch at the inlet plane, initial investigations showed excellent circumferential periodicity. Subsequent tests were therefore traversed over a single pitch but with a much finer grid and geometric progression in order to capture the thin igv wake which contributes a significant proportion of the overall loss at the inlet plane. The geometric progression can be seen in the plot of secondary velocity vectors which also show there to be excessively high crossflows in the wake which are due to the very narrow wake only affecting one of the side holes of the probe.

Figures 4.29 and 4.30 show that once again the shape of the Cp contours are the same as for the other inlet wake positions. Figures 4.31 and 4.32, the Cp rms contours, show that the level of unsteadiness is about the same as when the inlet wake was incident on the strut surface (figures 4.25 & 4.26), which is lower than for the case without inlet wakes (figures 4.18 & 4.19). Figures 4.33 and 4.34 show that the magnitudes of peak velocities and accelerations are greater with wakes at 40% and 60% strut pitch compared to the case without wakes (figures 4.20 & 4.21) or with wakes at 10% pitch (figures 4.27 & 4.28).

4.7 Phase 1 Area Traverses

Figures 4.35-4.46 contain the results of the combined 3 and 5 hole probe traverse measurements at planes -1,3,6 and 11 in the phase 1 duct at 0,15 and 30 degrees inlet IGV swirl angles. At each plane and swirl angle, five plots are presented. They are, total pressure, static pressure, yaw angle and pitch angle contours and also secondary velocity vectors. The yaw, pitch and secondary velocity vectors were calculated by first calculating the mean flow direction for the particular data set, i.e. 3 hole hub, 3 hole casing or 5 hole bulk flow, and then each flow angle calculated and plotted relative to the mean flow direction.

Zero Degrees Swirl

Figure 4.35, the inlet plane (-1) at zero swirl shows the thin symmetrical inlet wake along with hub and casing boundary layers. The total and static pressures are almost uniform across the bulk flow since the inlet was designed to achieve a near uniform radial inlet total pressure and velocity distribution. Note, although it was possible to traverse over more than one pitch at the inlet plane, initial investigations showed excellent circumferential periodicity. Subsequent tests were therefore traversed over a single pitch but with a much finer grid and geometric progression in order to capture the thin igv wake which contributes a significant proportion of the overall loss at the inlet plane. The geometric progression can be seen in the plot of secondary velocity vectors which also show there to be excessively high crossflows in the wake which are due to the very narrow wake only affecting one of the side holes of the probe.

The low energy inlet wakes provide a mechanism for the transportation of low energy hub fluid to the free stream flow and free stream fluid to the casing, when acted upon by the radial pressure gradient set up by the first bend. This can be seen in figure 4.36 which is a measurement plane situated immediately downstream of the first bend. Both the pitch angle contours and the secondary flow velocity vectors show the radial outward flow within the low energy wake seen in the total pressure contour plot. Note how the inlet wake has mixed circumferentially into the free stream and hence, has decayed in intensity. Also note the thin hub boundary layer as a consequence of radial transportation which would otherwise be thick due to the diffusing flow. The now diffusing casing flow also causes the hub boundary layer to thicken. Slightly upstream where the flow accelerates around the first bend we would expect the boundary layer to thin significantly e.g. Parsons *et al* (1973). The radial static pressure gradient is also clearly visible in the static pressure contour plot.

Figure 4.37 shows the results of measurements taken at plane 6 which lies just before the second more gradual bend. Note here the static pressure gradient is now reversed as the influence of the second bend is taking affect ahead of the bend. However, the weaker radial pressure gradient due to the second bend plus the established secondary flow momentum from the first bend means that the direction of secondary flow is not reversed. This can be seen by the secondary velocity vectors and perhaps more clearly by the pitch angle contours which still show radial outward flow in the region of low total pressure corresponding to the inlet wake. Note the hub boundary layer is still relatively thin and the casing boundary layer which has grown thicker and is starting to show that the radial outward flow is turning back on itself and transporting low energy casing boundary layer flow into the free stream. This can also be seen in the secondary velocity vectors plot.

Figure 4.38 which was measured in the parallel exit section at plane 11, basically confirms the trends discussed so far. The clearest and most useful of the plots is probably the total pressure contours. This shows the hub boundary has grown thicker due to diffusion after the second bend and the low energy casing boundary layer has also continued to grow to almost occupy the casing half of the duct. Remnants of the inlet wake still exist but of course by now it is very weak and insignificant compared to the hub and casing boundary layers. The other plots show little information since the flow is in a parallel duct with no radial pressure gradient and hence the only effects are traces of the earlier duct flow, i.e. secondary flows.

15 Degrees Inlet Swirl

Figure 4.39 shows the results of an area traverse at the inlet plane with the igv's set at 15 degrees swirl angle. The total pressure loss as a result of flow separation on the leading edge of the flat plate igv's can be seen by an increased wake thickness compared to the zero swirl case. A thinning of the wake near both the hub and casing boundary layers suggests that the flow has not only been changed relative to the axial flow case as a consequence of added swirl but also by secondary flow creation at the vane tips and this is shown by the secondary flow velocity vectors plot; and which evidence of will also be shown later in figures 4.70 and 4.71.
Although the igv vanes are untwisted, their short chord and low turning result in a mean bulk flow which has almost the same yaw angle. The yaw contours show that only near the walls where the characteristic overturning of the flow occurs, does the yaw angle differ from the bulk flow angle.

On turning through the initial, radially outward bend the skew of the wakes is exaggerated as a consequence of conserving angular momentum which needs to balance out the centrifugal forces. By plane 3 (figure 4.40) the total pressure contours show that the wakes have rotated to lie at approximately 45 degrees from the radial direction. This trend is not clearly seen on the plot of yaw contours due to the large range of flow angles and few contour levels. Dominy *et al* (1995) showed an average increases of bulk flow yaw angle of 3 degrees compared to plane -1 which is due to the axially diffusing flow. There was also a radial bulk flow variation in circumferentially averaged yaw angle with the higher angles measured nearer the hub in accordance with conservation of angular momentum. The static pressure gradient is also visible in figure 4.40 with lower pressures near to the casing, largely due to the accelerated flow. One consequence of the wake skewing is that even at this relatively upstream position, little if any part of the wall boundary layer may be regarded as isolated from wake interaction influences.

The flow continues to develop through the duct with characteristics observed at plane 3. At plane 6 (figure 4.41) the radial pressure gradient has reversed although it is relatively weak. Here the wakes are observed to have skewed further and the high loss fluid associated with these wakes has almost entirely accumulated at the casing as shown by the total pressure contours. The vortical motion which continued to drive the flow

towards the casing in the axial flow case (figure 4.37, pitch contours) is no longer observed and this is reflected in figure 4.41 by the remarkably uniform circumferentially variation of pitch angle. The secondary velocity vectors in figure 4.42, show two counter rotating vortices in the casing half of the duct passage which as like the axial flow case act to transport the low total pressure core away from the casing and into the free stream. There is very little static pressure variation at the exit plane (plane 11).

30 Degrees Swirl

Figure 4.43 shows the inlet traverse for the 30 degree swirl case. At this flow angle the separation on the igv leading edge is very significant in terms of loss production. The inlet wake is spread across over half the igv pitch. The shape is similar to that seen for the 15 degree case with lower loss regions near to the tips due to overturning of the flow. This is clearly visible in the secondary velocity vector plot.
At plane 3 (figure 4.44) the skewing of the wake is approximately the same as at 15 degrees, best shown by the secondary velocity vectors. As the hub flow enters the first bend, it diffuses so rapidly due to the increased swirl, that the hub boundary layer thickens and ultimately would be at risk of separating. Conversely, the casing flow is thinner than it was for both 15 and 0 degree cases due to the increased swirl component. It will be shown later that these factors significantly effect the duct loss. It can be seen that the bulk flow yaw angle at this plane is well above 40 degrees due to the decelerated axial flow.

By plane 6 (figure 4.45) the flow has been skew so much that the four contour plots show almost uniform circumferential quantities. The secondary velocity vectors show a slightly exaggerated form of the picture at plane 3, i.e. more skewing of the inlet wake.
In the exit parallel section (plane 11, figure 4.46) the secondary velocity vectors show one large anti-clockwise vortex filing the whole passage from hub to casing. The hub boundary layer is thicker than for the 0 and 15 degree cases due to the increased swirl on the hub surface. The main difference between the flow at 30 degrees compared to the other two flow angles is that the low total pressure core which has been seen to move away from the casing surface by plane 11 in the two previous cases, is significantly reduced. There is a small region of low total pressure near the casing which corresponds to the secondary flow velocities transporting casing flow to the free stream.

4.8 Phase 2 Area Traverses

This section contains the results of area traverses made at plane -1 (inlet), slot 1 (immediately after the first bend) and slot 2 (in the parallel exit section), see figure 3.16. Slot 1 has the same nominal x/h value as plane 3 in the phase 1 duct, and slot 2 being in the parallel exit section of the duct, can be compared to plane 11 in the phase 1 duct. As explained in chapter 3, when struts are in situ in the duct, it is not possible to traverse with 3 and 5 hole probes at slot 1 on the phase 2 duct. Also note that all area traverses in the phase 2 duct have been made at zero degrees inlet swirl angle.
Although the inlet conditions are almost the same whether struts are present or not, they are nevertheless included as proof and also for completeness.

Figure 4.47 shows the measured inlet conditions for the case without igv's or struts present. The hub and casing boundary layers are clearly visible in the total pressure plot and the contours of yaw and pitch show that the flow is purely axial with a maximum deviation of 2.29 degrees.
Figure 4.48, the case with struts is almost identical to figure 4.47, the case without struts. Note in the static pressure plot, there appears to be a line dividing the hub and casing halves of the duct passage. The reason for this is twofold; firstly, the traverse was made in two circumferential sweeps, first the casing half then the hub half during which time the atmospheric pressure changed slightly, and secondly the contouring over such a small range has caused an interval to exist at the mid span position. This does not occur in the total pressure plot because here, the pressure range is that much larger due to the boundary layers.

Figure 4.49 shows the inlet traverse when the IGV's are in situ at zero degrees incidence. Note that all the phase 2 area traverses were made over two pitches to check on circumferential periodicity. A geometric progression was not used over two pitches and hence there appear to be small differences in the two inlet wakes because of the relatively few points defining the wakes.
As for the case without IGV's, figure 4.50 (IGV's and struts) is almost identical to figure 4.49 (IGV's , no struts).

Figure 4.51 shows the slot 1 results for the non-igv case and being at slot 1 it it without struts as well due to the traverse restrictions. It clearly shows a static pressure gradient of approximately 1 kPa from hub to casing which is the radial pressure gradient driving the secondary flows within the inlet wakes when they are present. Close examination of the total pressure plot reveals that near to the casing, the total and static pressure are about equal, i.e. the flow is stationary. This is confirmed by the yaw angle contours which show near zero flow angle in the bulk flow but values up to ± 40 degrees which is both outside the range of probe calibration and unlikely in a flow which has a high axial velocity.

Figure 4.52 shows the slot 1 results for when the IGV's are present. Visible are the two inlet wakes in the total pressure plot with once again a thick, low energy, stagnant flow in the near casing region. Again the yaw angles range from + 40 to - 40 degrees suggesting low axial velocity flows. The pitch contours show the radial outward flow (from hub to casing) within the two IGV wakes. The radial pressure gradient is of the order of 1 kPa in the bulk flow as in the non-igv case.

Figure 4.53a & b show the results measured at slot 2 (in the parallel exit section) for the case without IGVs and struts. There are no significant flow features for this particular case as shown by the secondary velocity vectors. The yaw and pitch angle contours show the exit flow to be within ± 10 degrees. The total pressure plot shows a low energy hub flow associated with the diffusing and thickening boundary layer. Note, at slot 2, the circumferential traverse is taken over two igv pitches when struts are not present but over two strut pitches when they are.

Figures 4.54a & b show the slot 2 results for the case with struts but no IGVs. The total pressure plot once again shows the low energy hub boundary layer but more importantly shows the large regions of loss associated with the downstream strut wakes. The yaw contour plot shows the bulk flow to be within ± 7 degrees however, close to the casing surface yaw angles increase to ± 30 degrees. This is confirmed by the secondary velocity vectors plot.

Figures 4.55a & b, the results for slot 2 with IGV's but no struts appear at first glance to be similar to the previous figure (with struts but no IGV's). Traversed over two igv

pitches the wakes are still clearly visible at the exit section of the duct although not as prominent as the wakes created by the struts in the previous figure due to the extra length and hence diffusion. Although difficult to see from the secondary velocity vectors, the pitch contours clearly show that the radial outward flow initiated at the first bend by the radial pressure gradient is still visible within the flow in the igv wakes.

The final set of results for the case with IGV's and struts may be seen in figure 4.56a & b. The first main difference between this case and the case without IGV's is that the flow appears to be more ordered and structured. The secondary velocity vectors show two counter rotating vortices within the downstream right hand strut passage. Although the complete left hand strut passage has not been measured, the part which was measured shows a voracity of the correct direction. The static pressure plot shows much better uniformity when IGV's are present in the duct possibly due to the better mixing of the flow by the process of secondary flows. The total pressure plot is dominated by the strut wakes however by comparing figures 4.54a and 4.56a it can seen that the secondary flows occurring when IGV's are present, act to mix the low energy casing flow more into the free stream flow.

4.9 Area Traverses at Planes A1, B1 & B2

As mentioned previously it was not originally possible to traverse at slot 1 when the struts were in situ in the duct, with the existing 3 and 5 hole probes and traverse. In order to investigate more fully the local influences of the struts on the duct flow, a new traverse mechanism and two new slots (slots A and B) were designed and added to the duct. From these slots, a number of smaller sized single hole pitot tube probes were manufactured in order to measure the total pressure loss development in and around the strut passage. The definition and traverse locations of these probes were described in chapter 3, figure 3.17, page 57.

Figure 4.57 shows the total pressure contours measured at plane A1 which is the axial location where the strut profile is thickest. Due to the duct geometry at this position it was not possible to traverse right up to the strut and hub surface and hence no boundary layers can be seen. However, they would be relatively thin at this point and compared to the thick dominant casing boundary layer seen in figure 4.57, their contribution to mass averaged loss would be relatively insignificant.

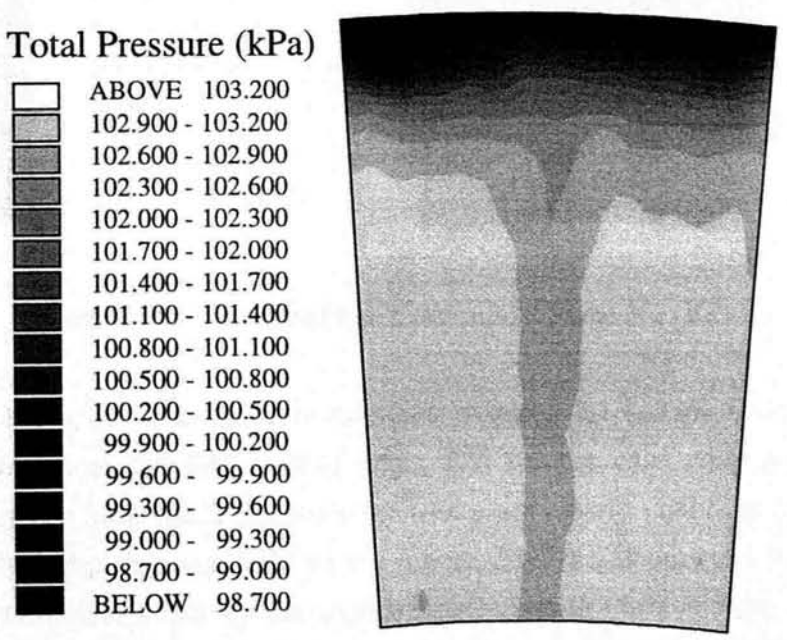

Figure 4.57 - Total Pressure Contours at Plane A1 (IGV's)

5mm upstream of the strut trailing edge at plane B2 (figure 4.58) it was possible to traverse up to the hub and casing surfaces. Here we can see the relative significance of these parts of the flow. Note the thin strut surface boundary layers and slightly thicker hub boundary layer which also shows signs of radial flow due to the inlet wake positioned at mid strut pitch. More importantly the casing boundary layer has grown in physical size and intensity due to the interaction of the strut and casing flows. The radial outward flow at mid pitch can be seen to re-energise the casing flow and hence partly suppress any flow separation.

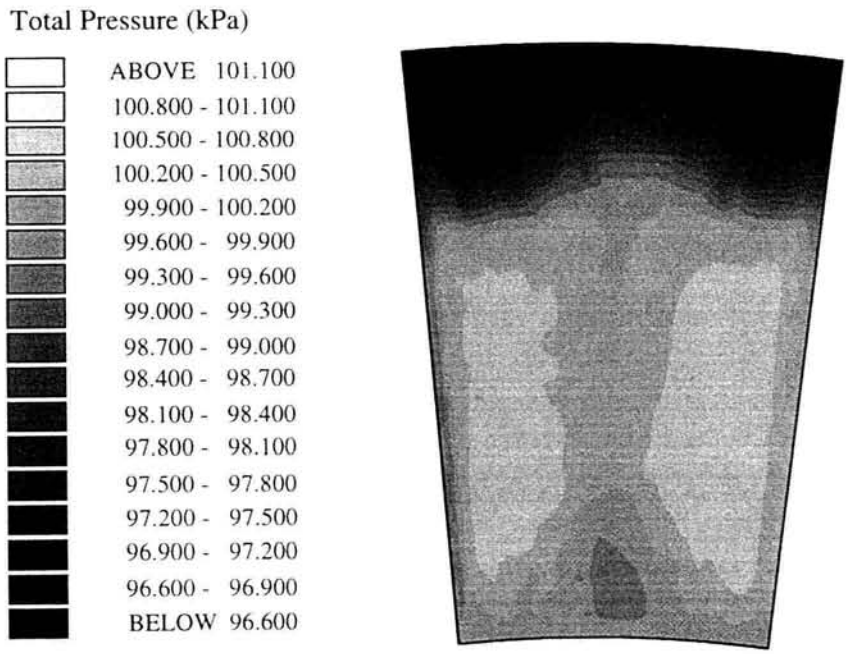

Figure 4.58 - Total Pressure Contours at Plane B2 (IGV's)

Figure 4.59 shows the total pressure contours at plane B1 (133% Cax) i.e. 1/3 strut chord downstream of the strut trailing edge, still for the case with igv's and struts. Measured over one strut pitch, the two strut wakes are clearly visible at the sides of the picture with the decaying igv wake in the centre. The radial outward flow within the inlet wake is still clear to see by the total pressure contour plots and the two loss cores due to the strut casing interaction are spreading and mixing into the free stream and hence decaying in intensity.

Qualitatively it has been shown that the major loss generator is the strut casing region where the combined diffusion rates highest.

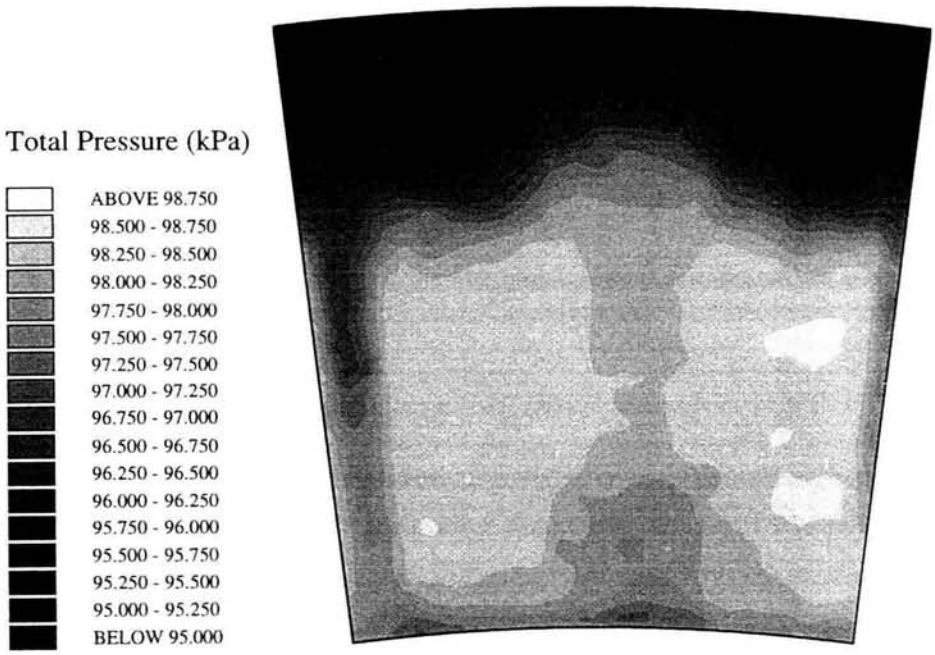

Figure 4.59 - Total Pressure Contours at Plane B1 (IGV's)

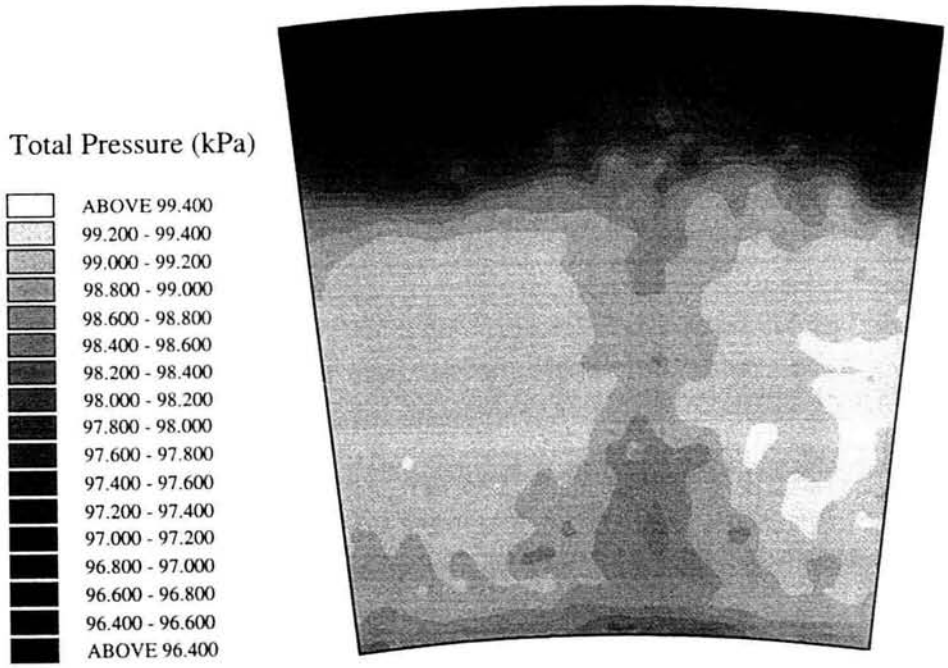

Figure 4.60 - Total Pressure Contours at Plane B1 (No Struts)

Figure 4.60 shows the total pressure contours measured at plane B1 for the case with igv's but no struts. Evidence of radial flow within the IGV wake can be seen, however, the contours appear to be less ordered compared to figure 4.59 where the struts were present. This agrees with the previous section's results when comparing figures 4.55a & b with figures 4.56a & b which were measured at slot 2. Qualitatively the overall losses at plane B1 appear to be greater when the struts are added to the duct.

4.10 Strut Casing Fillets

It has long been known that the addition of a 'fillet' to a wing body junction on aircraft can have a significant impact on interference drag associated with the intersection of the two bodies, e.g. Devonport *et al* (1990). The interference drag is that component of drag of an assembled wing and fuselage which is greater than the sum of the drag of the two bodies, each measured separately. It seems reasonable that an analogous effect may exist within turbomachinery blade rows. Debruge (1980) showed qualitatively that a fillet in a 90 degree corner can drastically reduce the probability of corner flow separation. Unfortunately no loss measurements were made. Devenport *et al* (1990) concluded from their experiments that their fillet did not prevent leading edge separation, or apparently the formation of a horseshoe vortex. Instead it displaced the separated flow structure away from the wing surface in a manner that suggested it increased the effective radius of the nose of the wing. He went on to conclude that with the possible exception of it is effect on interference drag (which could not be discerned from the measurements in the investigation) the fillet did not modify the flow past a wing body junction in a desirable way.

In choosing the size of a fillet radius there is usually a compromise between having it large enough so as to reduce or eliminate any corner interference drag but not so large that it effects the aerodynamic performance.

The fact that little literature on this subject has been published, possibly because general guidelines cannot be suggested for particular applications since the size of optimum fillet may be so geometry dependent, meant that designing strut casing fillets for the Durham SND had to be an educated guess based on an unpublished report which tested the efficiency of a two stage air turbine with 5 different sizes of fillets. Two different sized fillets were decided upon and manufactured from silicon rubber. Four struts were

filleted with the smaller fillets and another four with the large, the centre passage in each case was the one traversed. The fillets had equal radii around the strut and had the dimensions shown in figure 4.61 and table 4.3. The reason for the fillet not being symmetrical (i.e. quarter of a circle) was to reduce the possibility of a thin rubber interface peeling away from the casing surface in the high speed flow. The fillet was adhered to the strut surface and assumed to sit flush with the casing surface when the casing was put in position.

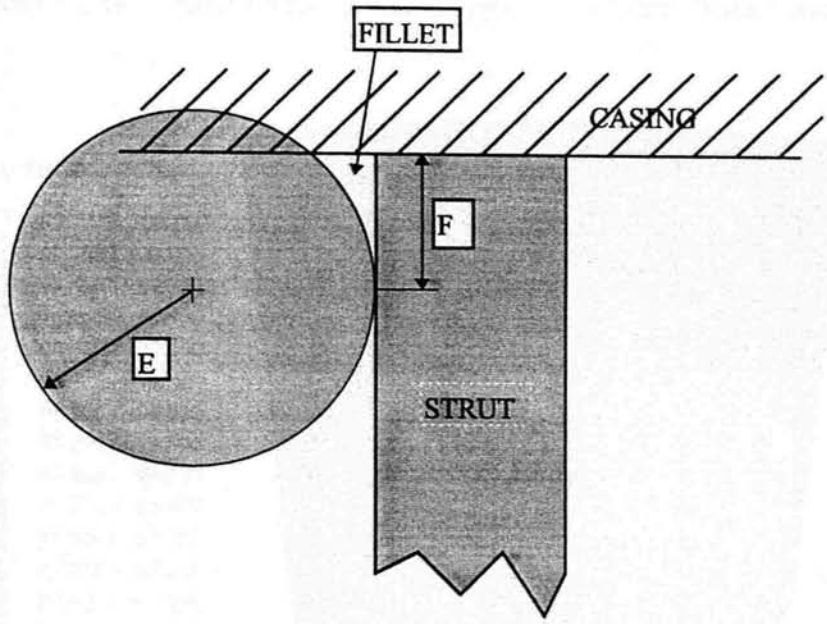

Figure 4.61 - Strut Casing Fillets

	E (mm)	F (mm)
Smaller Fillet	10	7
Larger Fillet	14	10

Table 4.3 - Strut Casing Fillet Dimensions

At plane A1 (the position of maximum strut thickness) the percentage blockage due to the smaller fillets was 0.35%. This is the ratio of the sum of the two fillet cross sectional

areas divided by the strut passage area without the presence of fillets. The calculated value for the larger fillets is 0.74%. Measurements downstream of the strut at plane B1 were made with the two different sized fillets to investigate whether or not the effect of the fillets was beneficial in terms of duct loss.

Figure 4.62 below shows the results for the smaller fillet case. Comparing to figure 4.59 (the equivalent unfilleted case) the trends appear to agree with Devenport *et al's* (1990) findings, i.e. the separated flow structure appears to have been displaced away from the casing and into the free stream. Qualitatively, the loss appears to have slightly increased with the addition of the smaller fillets. i.e. there appear to be more black contours.

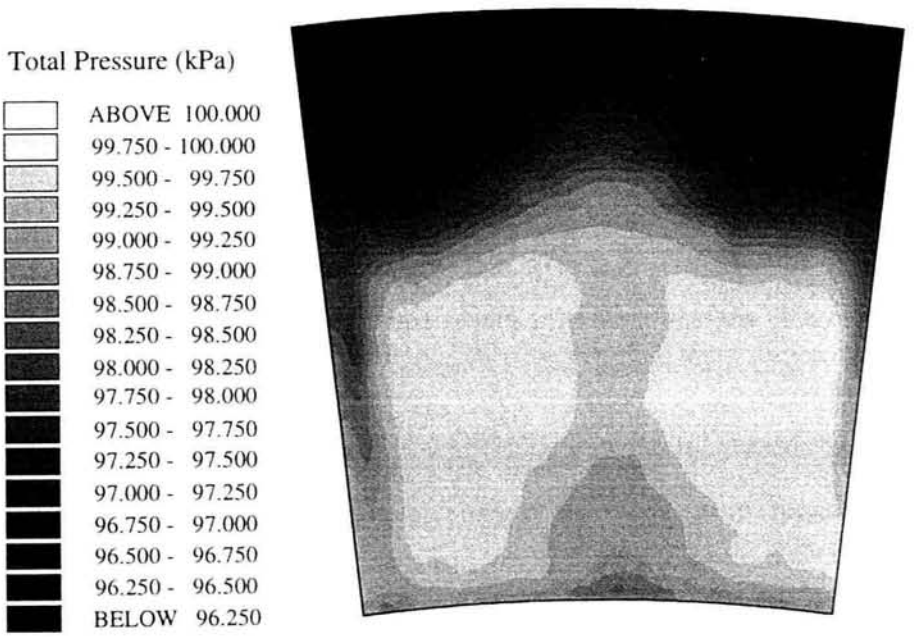

Figure 4.62 - Total Pressure Contours at Plane B1, Smaller Casing Fillets (IGV's)

Examining figure 4.63 (the larger filleted case) the trends appear to continue since the low pressure cores have shifted even further into the free stream when the size of the fillets are increased. It is difficult to say qualitatively whether or not the mass averaged loss has increased between the two sizes of fillet because although the low pressure core has extended further towards the casing, its intensity has if anything reduced.

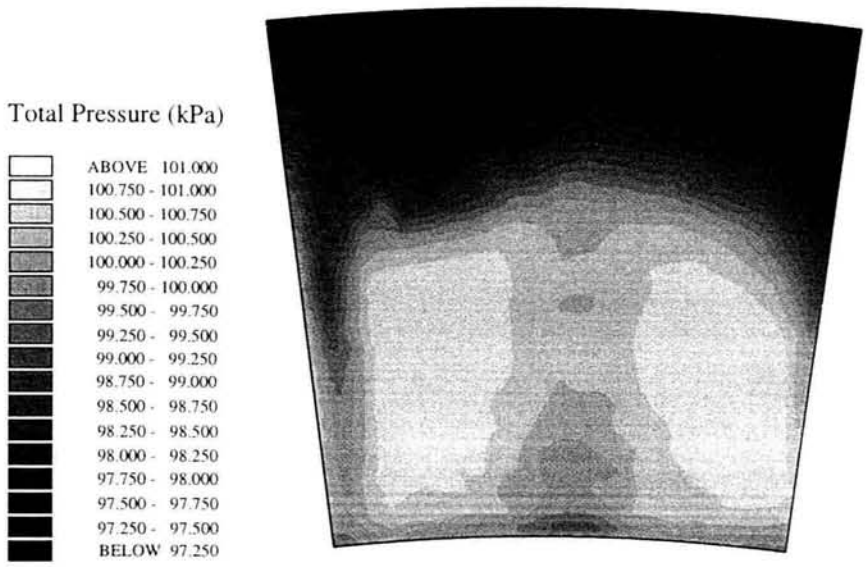

Figure 4.63 - Total Pressure Contours at Plane B1, Larger Casing Fillets (IGV's)

4.11 Strut Surface Boundary Layer

Using the system shown in figure 3.24 (chapter 3) it was possible to measure the strut boundary layer and know when the probe reaches the strut surface. The boundary layer was measured at 10 radial positions at plane A1 (the plane where it was not possible to complete a full area traverse due to the duct and strut geometry) to within 2mm of the hub and casing surfaces. The boundary layer thickness, δ, (the distance in which the velocity reaches 99% of the free stream velocity, Vm) was approximately 0.66 mm at mid span which is small due to the accelerated flow. This meant that with a probe radius of 0.25 mm only approximately 2/3 of the boundary layer could be measured. Figure 4.64 shows the boundary layer measured at mid span which has been normalised against free stream velocity, Vm, on the x-axis and by boundary layer thickness, $\delta \approx 0.66$ mm, on the y-axis. It is compared with a common approximation to a turbulent boundary layer [C.I.T. (1993)] where y is the distance from the surface, and shows reasonable agreement for the part of the boundary layer which could be measured due to the probe radius. This suggests the strut boundary layer is turbulent which would be typically expected at this part of the aerofoil since the Reynolds number based on strut chord and mid span strut trailing edge velocity is $\approx 4.5 \times 10^5$. The 10 traverses plotted in contour format, figure 4.65 show the boundary layer to be thicker nearer the casing compared the hub surface.

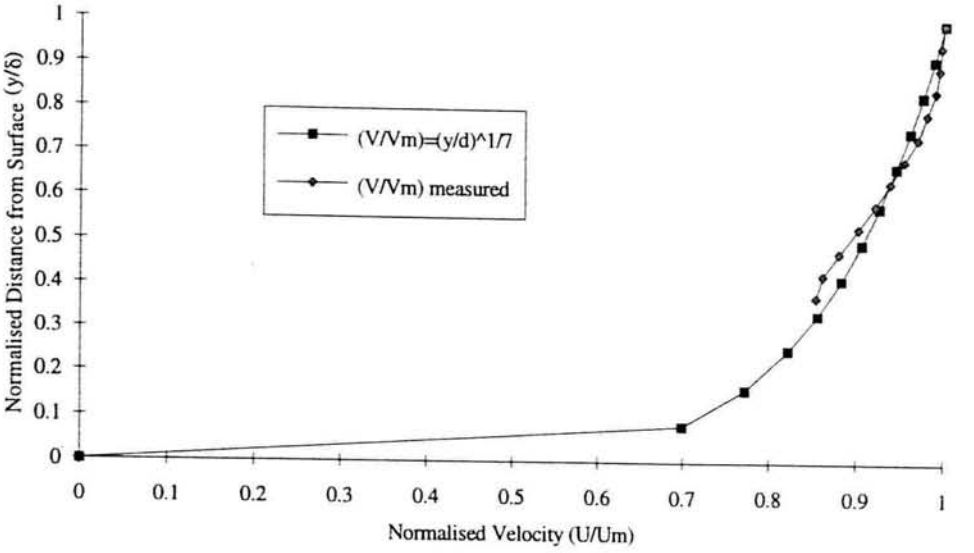

Figure 4.64 - Approximate Turbulent Boundary Layer Profile Comparison

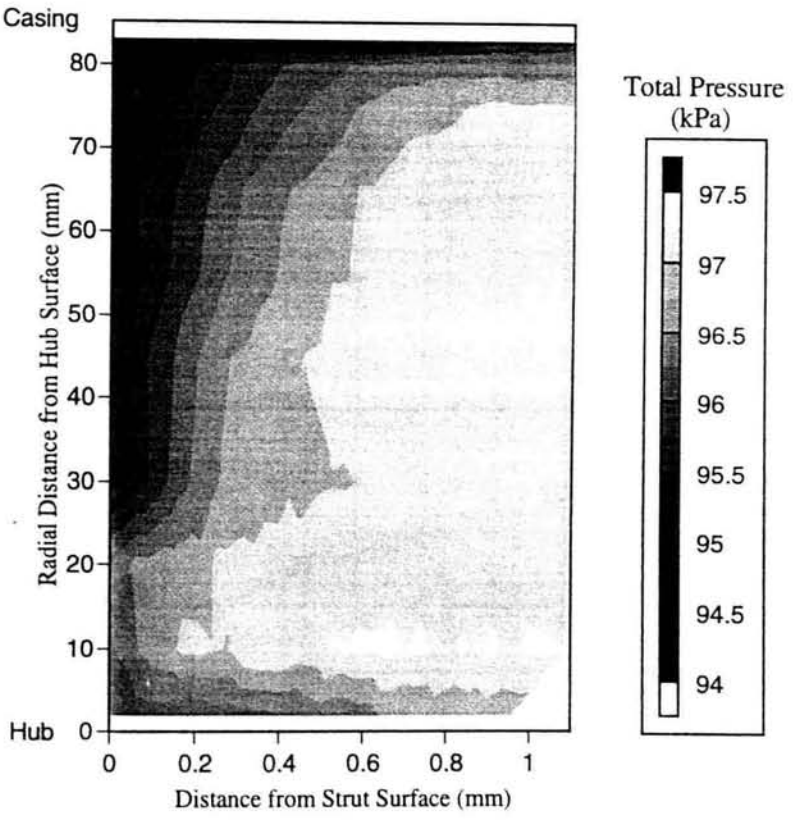

Figure 4.65 - Total Pressure Contours of Strut Surface Boundary layer at Plane A1.

4.12 Large Scale C4 Strut Aerofoil

A large scale (2.5:1) strut model was manufactured in order to ascertain the isolated Cp distribution and total pressure loss of the strut in a non-diffusing duct. This enables any other effects the struts may have on the flow when in situ in the duct, to be investigated. The large scale strut had 14 static tappings positioned along the chord at mid span with 6 of them within the first 10 % of the chord.

Figure 4.66 below shows the Cp distribution along with the strut profile. The flow rapidly accelerates around the leading edge to reach a peak Cp of -0.5 at about the 10% chord position. From here it diffuses all the way to the last tapping which is at 90 % Cax. The dotted lines are extrapolated to the strut leading edge where the flow stagnates giving a Cp of 1.

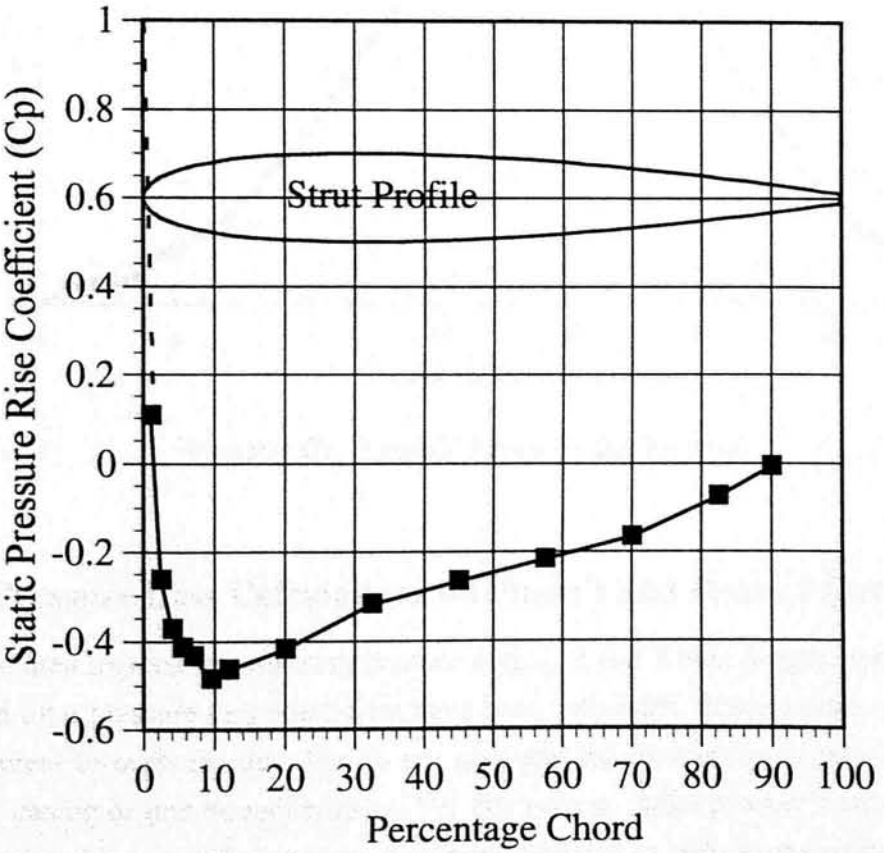

Figure 4.66 - Large C4 Strut Static Pressure Distribution

Figure 4.67 shows the downstream wake traverse results taken at 230% Cax so the wake had spread in the pitchwise direction. It shows a symmetrical wake with a peak loss of 11% inlet dynamic head. The mixed out value of total pressure loss coefficient based upon the mid-span pitch at the trailing edge was 1.19%. However, the Reynolds number of the large C4 strut was 30% lower than that of the real strut in the duct (3.5×10^5), and therefore a correction based upon the local skin friction coefficient (C_f') for a turbulent $1/7^{th}$ power law profile was made. i.e. $C_f' \propto (\text{Re. No.})^{-1/5}$. This reduces the loss coefficient by 0.08% to a value of Cpo = 1.11%, based upon the difference in Reynolds numbers.

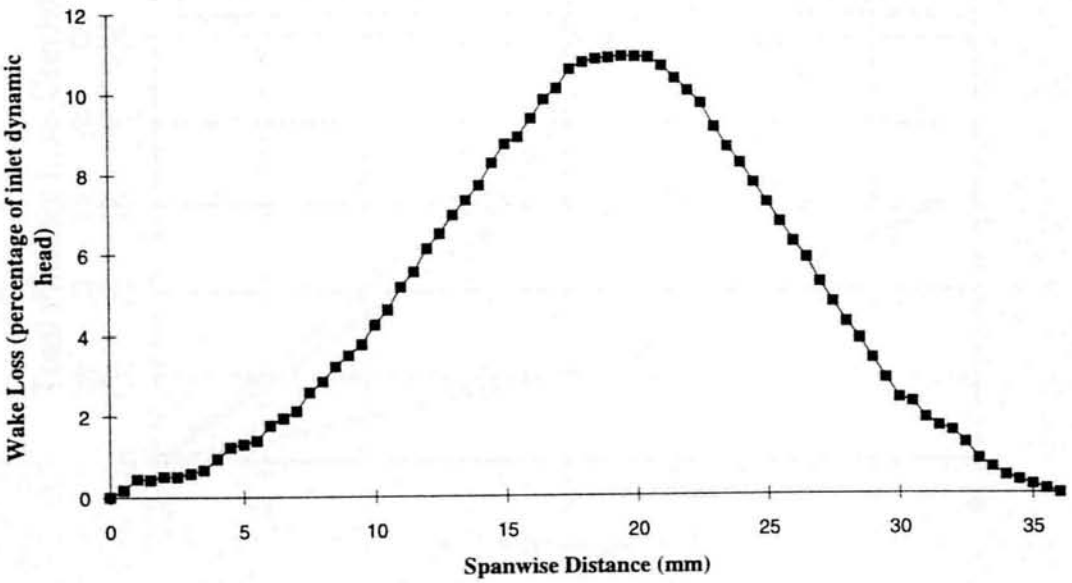

Figure 4.67 - Large C4 Strut Wake Traverse

4.13 Total Pressure Loss Calculations on Phase 1 and Phase 2 Ducts

From the area traverse measurements made with 1, 3 and 5 hole probes, values of mass averaged total pressure loss coefficient have been calculated. These values give the loss development through the duct but do not give any information as to the source of the loss, i.e. casing or hub boundary layer. For this reason, radial plots of circumferentially mass averaged loss coefficient have also been included to help in the explanation later as to the main sources of duct loss.

4.13.1 Phase 1 Duct With Varying Swirl

Figure 4.68 shows the measured phase 1 duct loss at 0, 15 and 30 degrees swirl. The duct loss is simply the measured loss at the local plane minus the measured loss at the inlet plane. Table 4.4 gives a summary of these losses.

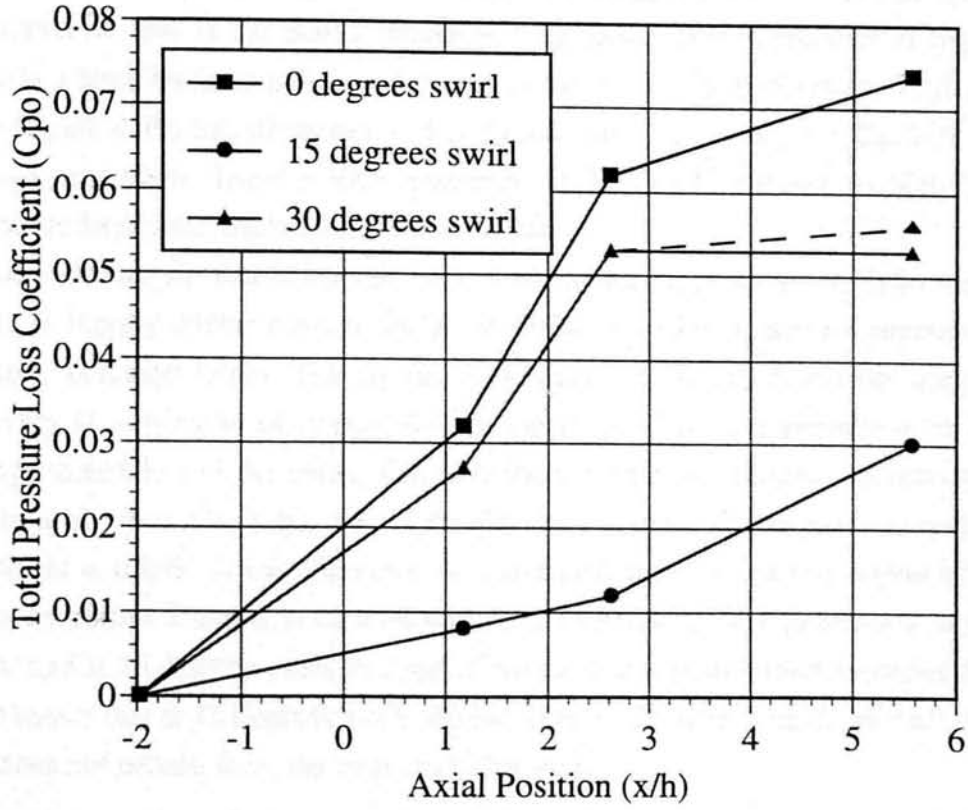

Figure 4.68 - Phase 1 Duct Cpo Development at Three Swirl Angles

Swirl Angle (degrees)	Plane 3	Plane 6	Plane 11
0	0.032	0.062	0.074
15	0.008	0.012	0.030
30	0.027	0.053	0.053

Table 4.4 - Summary of Phase 1 Duct Loss Development

Figure 4.68 shows that for the phase 1 duct, there appears to be an optimum swirl angle from the point of view of total pressure loss, between the angles of 0 and 30 degrees and that it is likely to be close to 15 degrees. The 15 degree case shows that the most significant difference compared to the 0 degree case is from plane 3 to 6. In this part of the duct, the losses are reduced by 87% when 15 degrees swirl is introduced. Close examination of figures 4.69 and 4.70 show that the part of the duct responsible for this difference in loss is the casing boundary layer flow. At 0 degrees swirl (figure 4.69) there is a large increase in loss at the casing from plane 3 to 6 but in the 15 degree swirl case (figure 4.70) this difference is significantly less, accounting for the 87% reduction in loss generation. There is little difference in the two hub flows; in both the loss is mainly redistributed further into the free stream.

These facts suggest that at zero degrees swirl, the casing boundary layer between planes 3 and 6, rapidly thickens due to sustained diffusion under an adverse pressure gradient causing increased losses. This agrees with figure 4.13 which shows the static pressure recovery at varying swirl angles. At zero degrees swirl, there appears to be a sudden change in gradient of the casing line indicating a reduction in diffusion rates at an axial position of x/h = 0.9. Table 3.3 shows that the x/h value of the plane 3 traverse at the casing is = 0.889. It can therefore be concluded that, the casing region of the duct between planes 3 and 6 is responsible for the significant loss generation at 0 degrees swirl, and at 15 degrees swirl, this part of the duct flow is alleviated significantly. Figure 4.70 shows that at 15 degrees swirl, the hub flow in the latter part of the duct (plane 6 to 11) does not benefit from the increased inlet swirl.

Increasing the swirl angle to 30 degrees does not benefit the flow further in terms of losses; in fact they are made worse, and approach the values measured at 0 degrees, as shown by figure 4.68. The losses generated between the inlet and plane 3 are due to the hub boundary layer thickening under the extreme swirl angle. As discussed in chapter 2, if the swirl angle is high enough, hub boundary layers can grow and under extreme conditions even separate. Figure 4.44 shows the extremely thick hub boundary layer responsible for the increased losses between plane -1 and 3. The hub boundary layer remains fairly unchanged from plane 3 to the exit, however, the increased path length on the casing due to the swirl, causes the losses from plane 3 to plane 6 to increase. This is also shown by the thickened casing boundary layer seen in figure 4.45. From plane 6 to 11 there appears to be no loss. This is clearly not the case since even in a parallel duct

with well behaved flow, there will be some losses due to skin fiction. Figure 4.46 reveals the reason. Due to the duct and probe geometries, it was not possible to traverse up to all the surfaces at some flow angles, and 30 degrees swirl at plane 11 happens to be one of them. Figure 4.46 shows that some of the casing and hub boundary layers could not be measured and hence the value of mass averaged loss is lower than it should be. The value at plane 11 for the 15 degree swirl case has a similar problem but the discrepancy here is a lot less for two reasons. Firstly the probe could traverse closer to the duct surfaces and secondly, the different flow structure at 15 degrees swirl causes a lot of the casing boundary layer loss to be transported into the free stream and is therefore accounted for, (figure 4.42). A conservative estimate of the duct loss at plane 11 based upon the parts of the boundary layer which could be measured, produces a minimum value of loss coefficient = 0.056, which is shown in dotted in figure 4.68.

Figures 4.70 and 4.71 also show drops in loss towards the hub and casing tips which was mentioned in section 4.7. These are due to a thinning of the inlet wakes due to secondary flows.

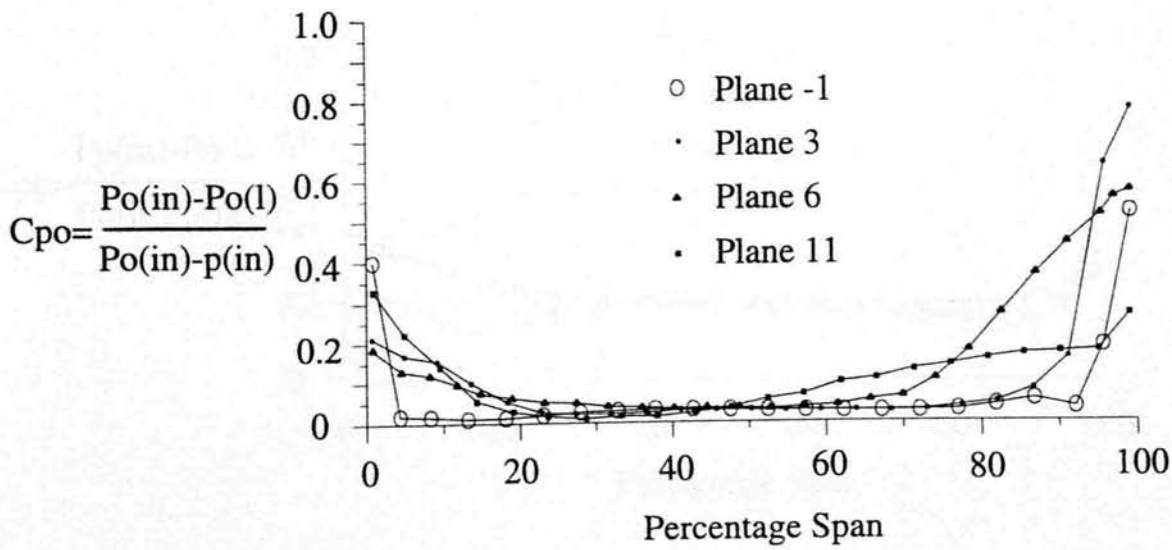

Figure 4.69 - Radial Distribution of Circumferentially averaged Cpo
(Phase 1, 0 degrees Swirl)

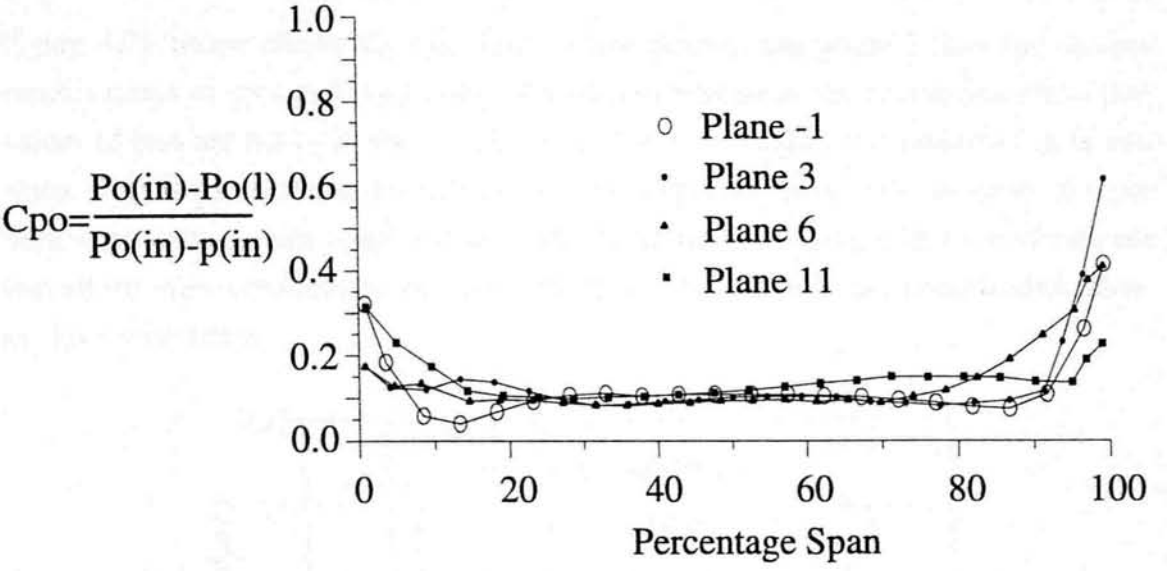

Figure 4.70 - Radial Distribution of Circumferentially averaged Cpo
(Phase 1, 15 degrees Swirl)

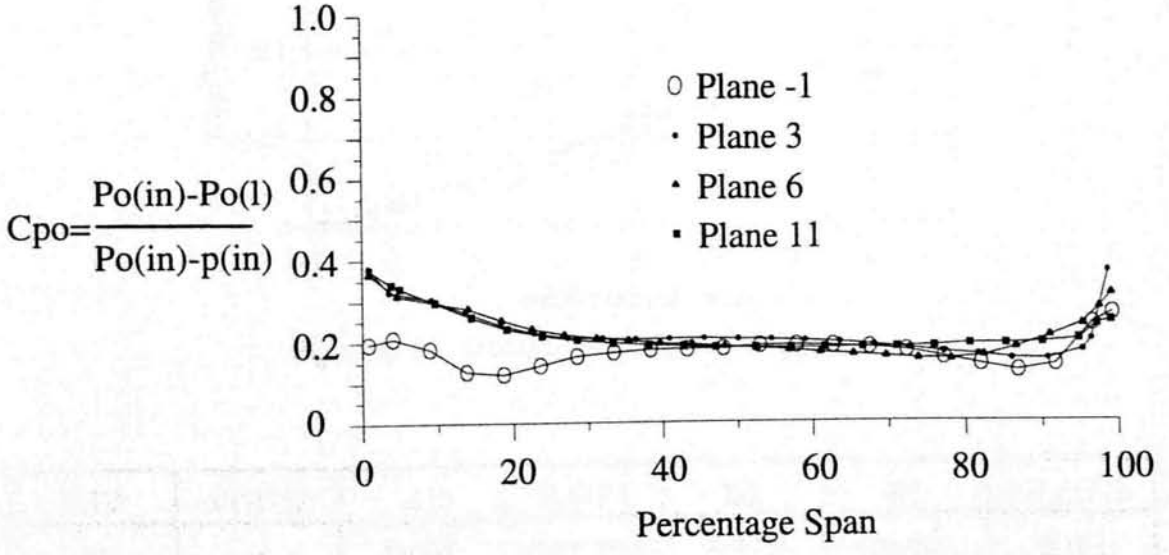

Figure 4.71 - Radial Distribution of Circumferentially averaged Cpo
(Phase 1, 30 degrees Swirl)

4.13.2 Phase 2 Duct with Combinations of Fillets, Struts and Igv's

Figure 4.72 below shows the loss development through the phase 2 duct for various combinations of igv's and struts. Table 4.5 which summarises the duct losses, show that values of loss are not available at every plane for every single permutation of igv's and struts. This is for two reasons; firstly it was not physically possible to traverse at some planes for some combinations and secondly , time restraints along with necessity meant that efforts were concentrated on investigating the more realistic and complicated cases. i.e. igv's with struts.

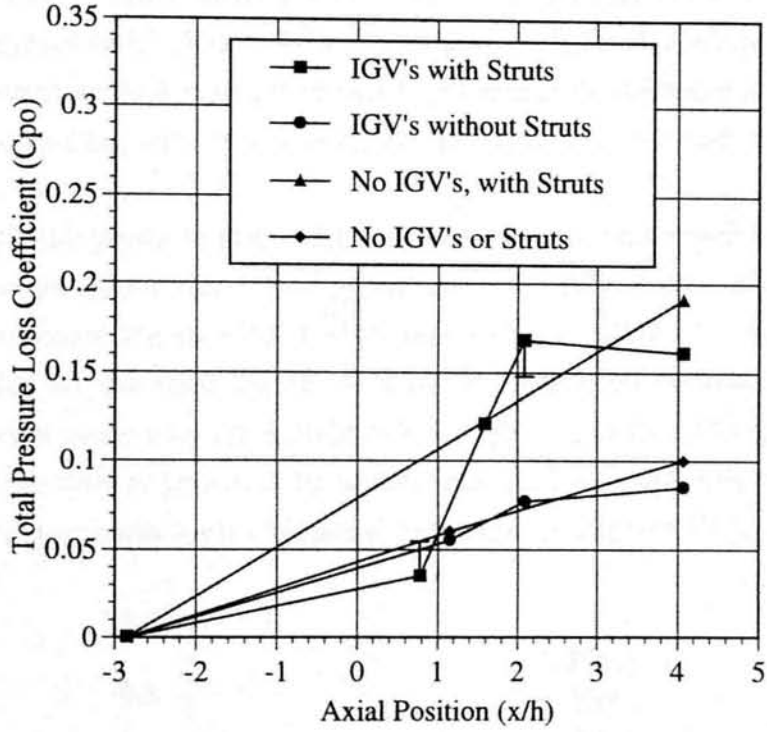

Figure 4.72 - Phase 2 Duct Cpo Development

IGV	STRUT	A1	SLOT 1	B2	B1	SLOT 2
✔	✔	0.035	********	0.121	0.168	0.161
✔	✘	********	0.055	********	0.077	0.085
✘	✔	********	********	********	********	0.191
✘	✘	********	0.060	********	********	0.100

Table 4.5 - Summary of Phase 2 Duct Loss Development

The first point to note about figure 4.72 is that the duct losses for the two cases with struts are almost double the measured losses without. With igv's present the increase in loss due to the strut is 189% and without igv's it's 191%; remarkably similar. The source of increased loss can be ascertained by comparing figure 4.73 with 4.74 or slightly clearer due to more measurement planes, figure 4.75 with 4.76. Plane B1 in figures 4.75 and 4.76 shows that the loss is attributed to the casing flow in the region of the strut which confirms the qualitative results found from the contour plots earlier in section 4.9.

The next point to note is that for both cases (with and without struts) the losses are less with the igv's in situ. Both cases give a reduction in loss coefficient of 15% when igv's set at zero degrees swirl are added. This is because the igv wakes allow secondary flows to develop which act to re-energise the thick low energy casing boundary layer. This can be seen by comparing slot 1 results in figures 4.73 and 4.75, (the case without struts).

In figure 4.72, the points at planes A1 and B1 have error bars added to them. The first point (A1) shows an error bar extending upwards. This is because at plane A1 it was not possible to measure the strut boundary layers which would act to increase the actual loss. At plane B1 the error bar shows a move downwards because the uncalibrated single hole pitot probe only reads accurately to within typically ±10 degrees. In this part of the duct, the flow is known to be separated at the casing and hence the loss is over estimated. This accounts for the 'apparent' rise in loss from plane B1 to slot 2.

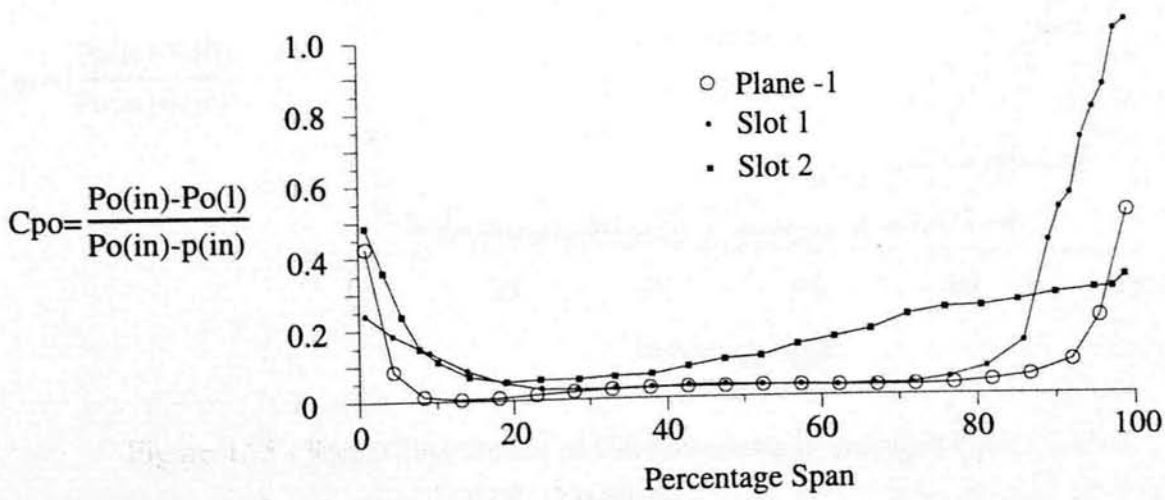

Figure 4.73 - Radial Distribution of Circumferentially averaged Cpo
(No IGV's or Struts)

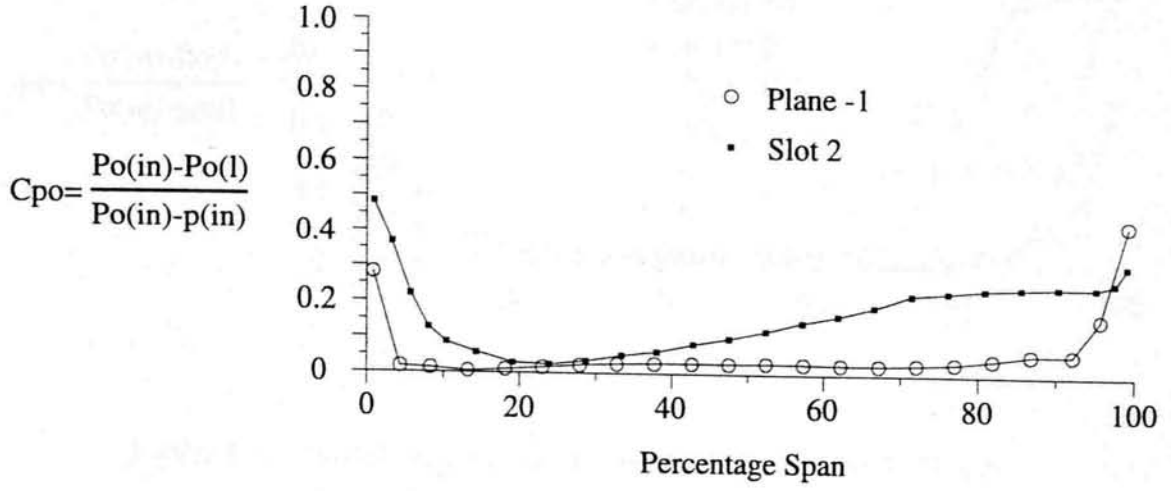

Figure 4.74 - Radial Distribution of Circumferentially averaged Cpo
(No IGV's, Struts)

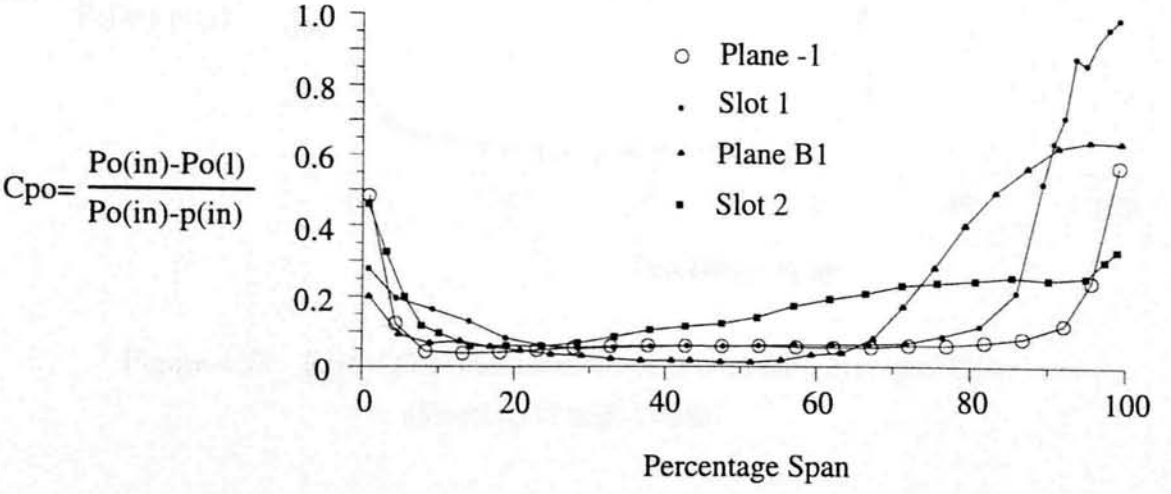

Figure 4.75 - Radial Distribution of Circumferentially averaged Cpo
(IGV's, No Struts)

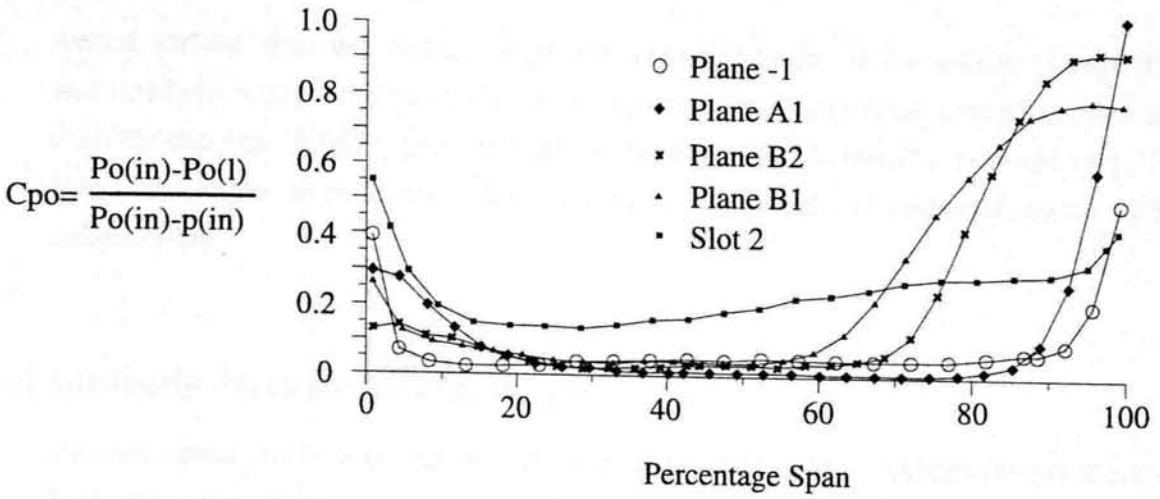

Figure 4.76 - Radial Distribution of Circumferentially averaged Cpo
(IGV's and Struts)

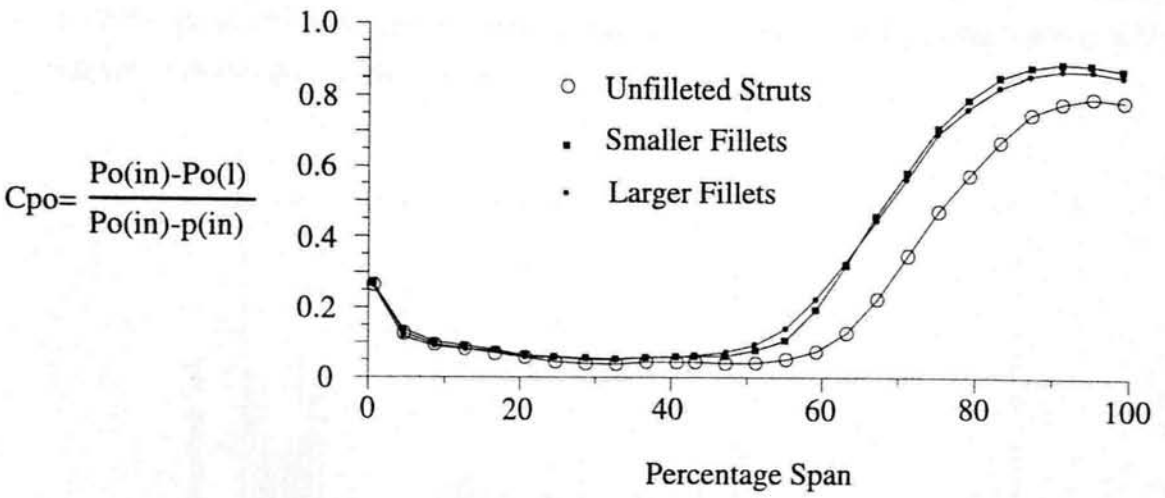

Figure 4.77 - Radial Distribution of Circumferentially averaged Cpo
(Small and Large Fillets)

The results for the filleted struts are shown in figure 4.77. As expected the three curves for the hub side of the passage are almost identical. The mass averaged values confirm the qualitative suggestion that fillets actually increase the total pressure loss. The smaller filleted case gave a duct loss of 0.251 and the larger filleted struts produced a Cpo = 0.252. The effect of the fillets was to increases the loss, possibly due to increased

wetted surface area and surface roughness since the finish on the silicon rubber fillet was nowhere near as smooth as the struts' surfaces. Swapping struts around showed that even for one size of fillet, both the flow distribution and loss coefficient could vary. The fillets also appear to redistribute the loss into the free stream as suggested earlier by the contour plots.

4.14 Unsteady Pressure Measurements

Unsteady pressure measurements were made at all of the static tappings shown in figure 3.11 using the equipment described in section 3.3.1, in order to ascertain if the flow separation shown by the flow visualisation results was of a repeatable dominant frequency. At each tapping 8192 data points were taken at a logging frequency of 400 Hz over a 20 second period. Fourier transforms of the signals were taken and plotted as a power spectrum as shown in figure 4.78. This contains the power spectrum measured at 100% speed (85 m/s inlet velocity), at the mid strut pitch casing static tapping which is level with the strut leading edge (see figure 3.11).

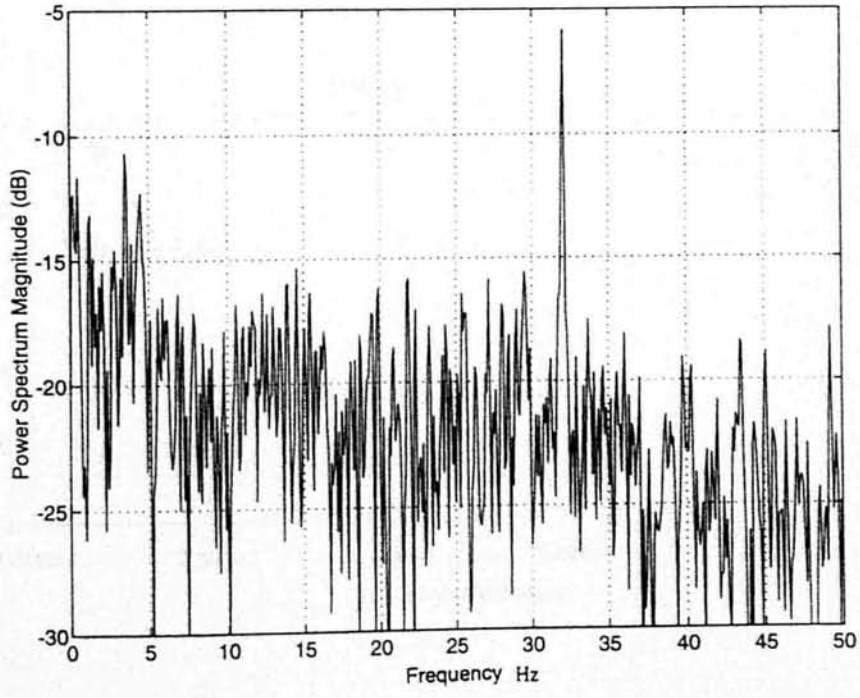

Figure 4.78 - Unsteadiness Power Spectrum at 100% Reynolds Number

Figure 4.78 shows that the unsteady signal contains a dominant frequency of 31.8 Hz. This frequency has a signal to noise ratio of an order of magnitude and was found to exist at all 16 tappings tested (figure 3.11) with approximately the same magnitude. Measurements were taken at the original tapping at progressively lowered Reynolds numbers to investigate it's effect on both the unsteady dominant frequency and the signal to noise ratio. In the flow phenomena known as vortex shedding, the Strouhal number is almost independent of Reynolds number, as long as the Reynolds number is high enough, so that the flow structure does not change. Although this flow phenomena is not vortex shedding (it is an unsteady separating boundary layer), it would not seem unreasonable to expect the reduced frequency to remain constant also. Strouhal number or reduced frequency for the vortex shedding of flow around an infinitely long cylinder is given by equation 4.1 [Massey, B.S. (1989)].

$$\frac{f.d}{Vm} = 0.198\left(1 - \frac{19.7}{\mathrm{Re}}\right) \qquad \{4.1\}$$

where f is the frequency of vortex shedding, d the cylinder diameter and Vm the free stream velocity.

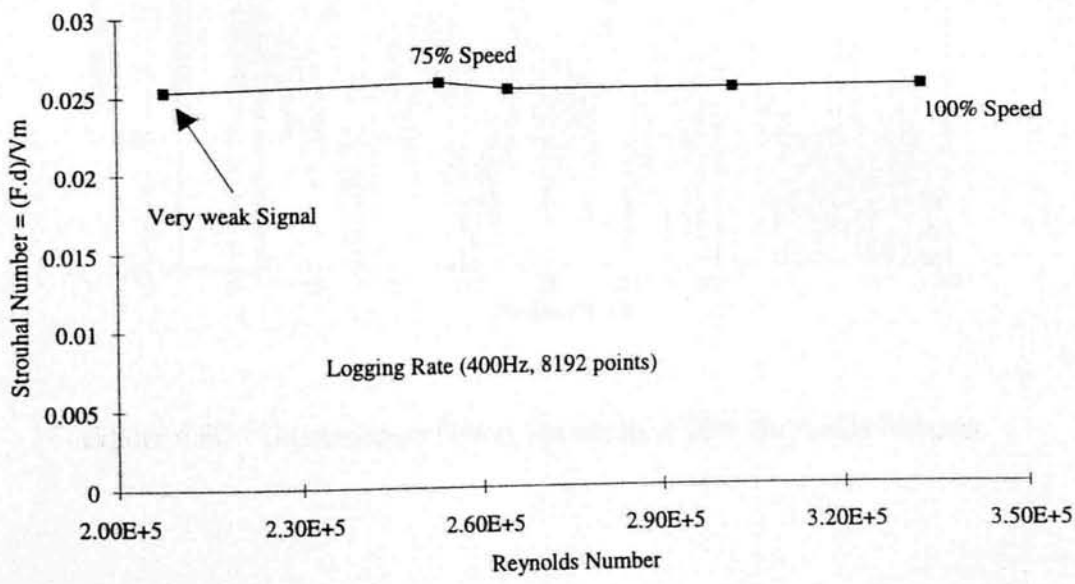

Figure 4.79 - Unsteadiness Strouhal Number Variation with Reynolds Number

Figure 4.79 shows that as the Reynolds number was lowered, the Strouhal number remains constant. i.e. as long as the flow structure remains unchanged the frequency of unsteadiness varies linearly with velocity. Figure 4.80 shows the measured results taken again from the original tapping but at 90% Reynolds number. However, as the Reynolds number was lowered, the signal to noise ratio also fell, until at approximately half speed (40 m/s inlet velocity) the signal to noise ratio was considered to be very weak (almost too weak to observe a dominant frequency above the noise) and possibly the flow regime was starting to change, i.e. the flow was not separating.

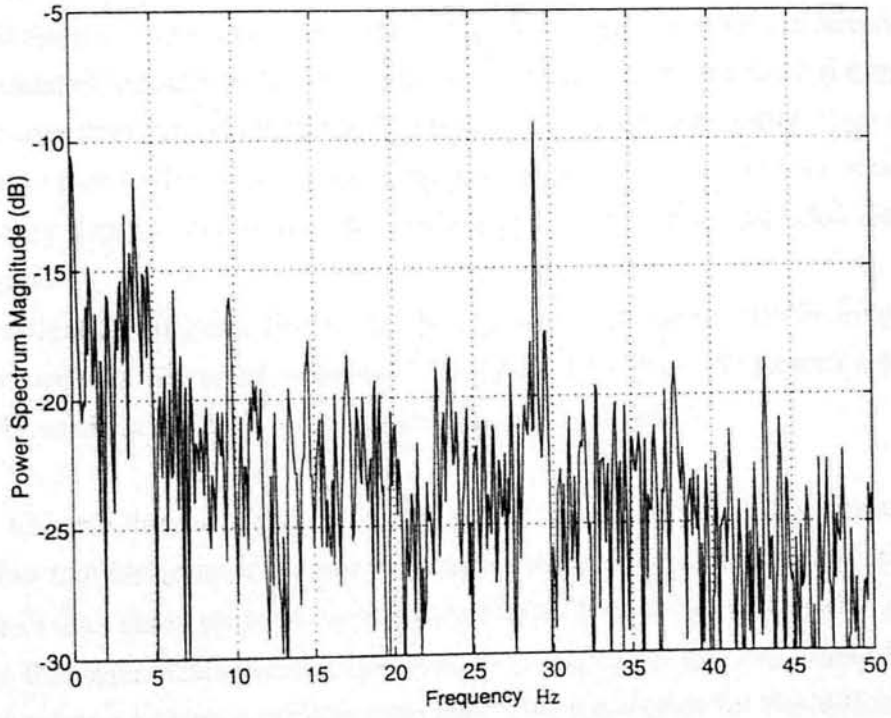

Figure 4.80 - Unsteadiness Power Spectrum at 90% Reynolds Number

Chapter 5

Discussion of Experimental Results

This chapter summarises the results presented and discussed in chapter 4 and will draw together some conclusions from them.

The effect of inlet swirl on the phase 1 duct has been discussed in detail in chapter 4, but in summary there appears to be an optimum swirl angle of approximately 15 degrees at which angle the total pressure loss coefficient is a minimum. This measured loss is approximately 40% of the measured loss at 0 degrees swirl and 57% of the measured loss at 30 degrees, however at 30 degrees swirl, the measured loss is almost certainly under estimated because of probe restrictions. These restrictions were present at swirl angles greater than zero degrees due to the duct and probe geometries. This meant that some areas close to the walls, where a significant proportion of the loss is situated due to boundary layers, could not be measured and therefore included in the loss calculations.
This investigation suggests that if the phase 1 duct was made slightly longer, i.e. the diffusion rate was decreased, improved performance in terms of reduced total pressure loss can be made at the design flow swirl angle of zero degrees.

No area traverse data is available for the phase 1 duct without IGV's, however, figure 4.12 shows that differences in static pressure recovery only exist locally within the duct. The overall duct static pressure recovery coefficient for the two cases (with and without IGV's) is the same. These local differences exist mainly on the first casing bend where the acceleration and hence velocities are high. One hypothesis for this difference is that the presence of the inlet wakes and hence secondary flows, acts to re-energise and thin the casing boundary layer which increases the local effective area.

In figure 4.14, (the static pressure distribution for the phase 2 duct, with and without IGV's and without struts), the same effect, may also be observed. It must be noted however that these differences are both local and small. The same effect can be seen in figure 4.15, when the struts are in situ. Table 4.3, p133, the summary of the phase 2 duct

loss development shows clearly the effect of the inlet wakes. For both cases, with and without struts, the addition of the inlet wakes reduced the overall duct total pressure loss coefficient by approximately 15%, compared to figure 4.15, due to the reasons already discussed. The wakes created by the IGV's were approximately 2-D wakes whereas in a real inter-turbine diffuser, the upstream blade row would have secondary flows associated with each wake which may help re-energise the boundary layers and hence reduce or suppress flow separation.

A change in the casing surface flow recovery gradient at x/h = 1 may be observed in both of the cases, suggesting that at this point, the flow fails to remain attached and hence the casing boundary rapidly thickens causing a reduced effective area increase. Kirkham (1993) measured the hub and casing boundary layer profiles at all 11 planes in the phase 1 duct and at x/h = 1, the casing boundary layer profile shows classic signs of the separation point profile, shown in figure 2.5.

Figure 5.1 below, shows the casing surface shape factor development through the phase 1 duct with inlet wakes, [Kirkham (1993)]. The three regions of typical laminar, transitional and turbulent boundary layer values have been marked on the graph. However, shape factor on its own, is not sufficient information which can be used to define the type of boundary layer present. For example, a high shape factor, ≈ 2.5, could arise from a turbulent boundary layer undergoing continuous acceleration and hence re-laminarising, as is sometimes the case in turbine blade passages.

Figure 5.1 however, suggests that the rapid rise in shape factor occurs at x/h $\approx$ 1, i.e. into the diffusing part of the casing flow. A high shape factor due to a re-laminarisation can only arise in a continuing accelerated flow as already mentioned. Therefore, it is more likely that the high shape factor beyond x/h = 1, is due to a turbulent boundary layer separation which can occur at shape factor numbers of around 2. This hypothesis is certainly consistent with the other available information, e.g. change in static pressure recovery gradient at x/h = 1.

This flow phenomenon has a detrimental effect on the total pressure loss coefficient as will be discussed shortly.

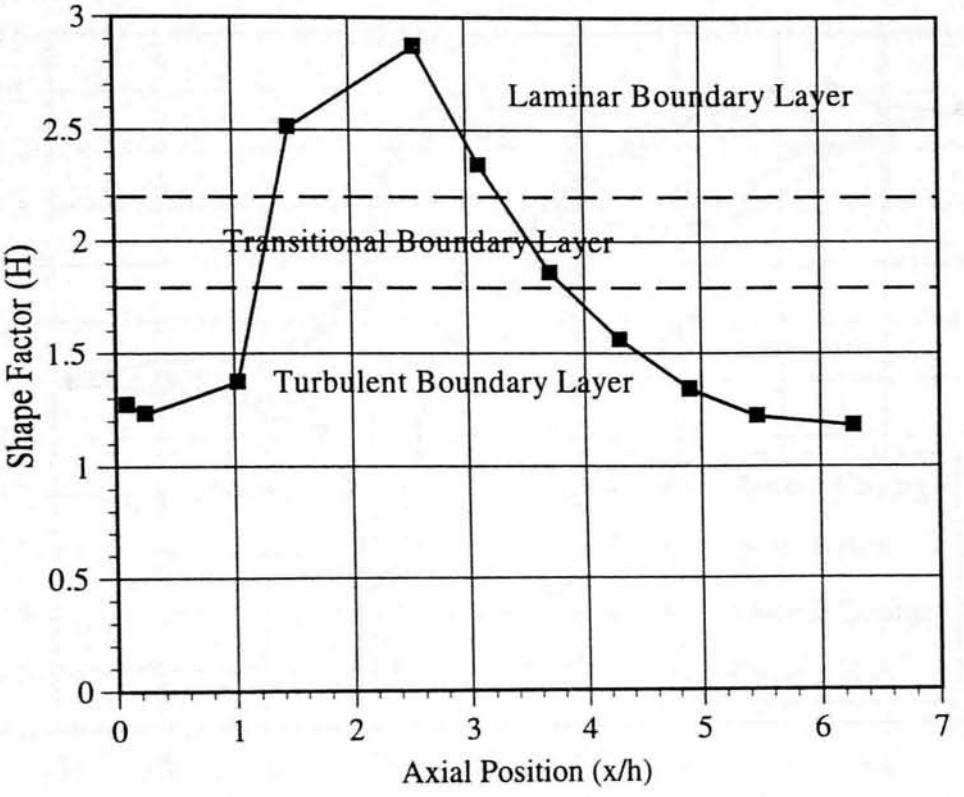

Figure 5.1 - Phase 1 Duct Boundary Layer Shape Factor Development, With IGV's [Kirkham (1993)]

Figure 5.2 shows the static pressure recovery development for the phase 1 and phase 2 ducts, both with IGV's for direct comparison. The more severe casing bend on the phase 2 duct causes the flow to reach a peak suction Cp value of -0.5 compared to -0.35 for the phase 1 duct. The following diffusion rates are hence greater in the phase 2 duct and the change in static pressure recovery gradient associated with the thickening and separating boundary layer occurs at an earlier axial position of x/h = 0.5 compared to x/h = 1 for the phase 1 duct. The other major difference between the two ducts is the hub curvature on the second bend. In the phase 2 duct, the convex hub curvature is greater than in the phase 1, causing the flow to accelerate to the same velocity as measured at the inlet; the phase 1 reaching a Cp = 0.25.

As in the phase 1 duct case, the effect of IGVs only caused local changes in the static pressure recovery; the difference in overall duct recovery was negligible. Their addition did however have a beneficial effect on the duct total pressure loss coefficient by reducing it by 15% for both cases, with and without struts. This 15% reduction in loss with IGV's is generated duct loss and does not include the additional loss created by the IGV's themselves. Britchford *et al* (1997) however, found that their non-diffusing inter-compressor swan neck duct loss coefficient increased from 0.020 to 0.035 when inlet wakes were added. They attributed this increase in loss to mixing of the OGV wakes within the duct, which since their duct was not separating, could not be offset by a larger reduction in loss due to suppression or reduction of flow separation.

Table 5.1 summarises the phase 1 and phase 2 duct static pressure recovery and effectiveness for the IGV cases. It shows that the phase 2 duct recovers 4% less inlet dynamic head compared to the phase 1. The addition of struts to the phase 2 duct has a larger adverse effect and recovers 9% less inlet dynamic head than the empty duct case. The phase 1 duct was 83% effective in recovering static pressure whereas the phase 2 with struts was only 56%.

	Cp	ε
Phase 1	0.46	83%
Phase 2 (Without Struts)	0.42	76%
Phase 2 (With Struts)	0.31	56%

Table 5.1 - Summary of Phase 1 and Phase 2 Duct Cp and ε (with IGV's)

Figure 5.6 compares graphically the measured losses of the two ducts for the case with IGV's. It clearly agrees with the static pressure recovery results, i.e. the phase 1 duct has the highest overall duct Cp with lowest Cpo and the opposite for the phase 2 duct with struts. Note once again the *apparent* reduction in loss for the phase 2 duct case with struts, as was observed in section 4.13.2. This was attributed to an overestimation of the

true loss at x/h ≈ 2, due to the unavoidable inaccurate measurement of total pressure when using an uncalibrated single hole pitot probe at large flow angles.

It should be noted that the data contained in Table 5.1 was obtained using area averaging. Care must be taken if losses using these values along with the equations given in section 2.3 are obtained and compared to the mass averaged values shown in figure 5.6 (and elsewhere in the thesis). All experimental losses derived from area traverses using both single or multi-holed probes and all CFD losses have been calculated using mass averaging. Difference between the losses derived from the two different methods of averaging may exceed 30% in some cases.

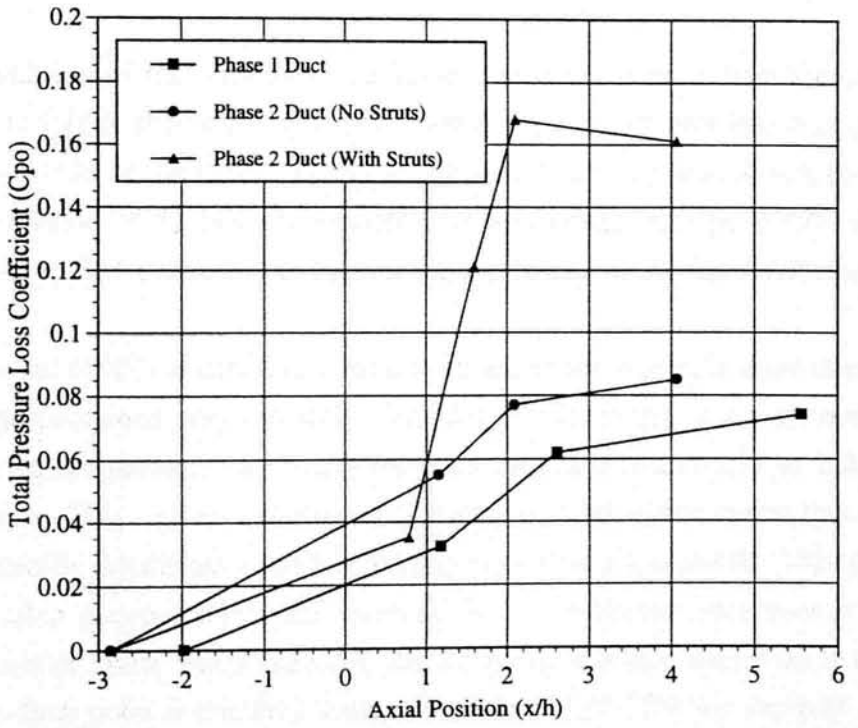

Figure 5.6 - Phase 1 and Phase 2 Ducts' Measured Cpo Developments

The large scale strut investigations described in section 4.12 were intended to highlight the influence of the struts on the duct flow, and vice versa, and in particular the additional losses incurred due to the struts themselves. As shown in chapter 4, an isolated C4 profile aerofoil in a non-diffusing duct produces a mass averaged stagnation pressure loss coefficient of 1.11%, based upon inlet dynamic head, which for the large

scale strut is the same for the strut and duct inlet since there is no duct curvature or diffusion. However, for the smaller diffuser struts this is not the case, since, there is both a radial static pressure gradient due to flow acceleration and deceleration due to duct curvature, and also a slight axial pressure gradient due to the downstream duct diffusion. This poses the difficult question of what should be taken as the smaller strut inlet dynamic head, in order to directly compare the large scale strut loss with the smaller strut loss. Since whatever value of inlet dynamic head assumed for the smaller struts, will always be different from the duct inlet dynamic head and hence impossible to make a direct comparison, it seems sensible to be consistent and use the same reference throughout, i.e. the duct inlet dynamic head but then to bear caution when making quantitative comparisons.

A simple addition of the strut and duct losses raises the overall duct loss coefficient from 0.085 to 0.096, shown in figure 5.7. Even if the isolated strut loss was doubled to 2.2% which would be the case if the actual strut inlet velocity was 60 m/s compared to the assumed value of 85 m/s, the overall duct loss would only be 0.107. The actual measured rise to 0.16 demonstrates the dramatic influence of the strut/wall interaction.

Britchford *et al* (1997) carried out a similar investigation however their duct was non diffusing and contained only one strut. They found that for the case with realistic inlet compressor wakes present, the overall duct loss increased from 0.035 to 0.038 for the inlet wake case. This implies a maximum strut loss of 0.3% which seems low even for a NACA 65 profile which has a sharper leading edge than a C4 profile. This diminutive increase is also questionable since nowhere in the published text does it state the number of outlet guide vanes used, i.e. the pitchwise distance over which the loss is averaged. A final point is that they quote an accuracy of ±0.75% for the inlet wake case which means that the measured increase of 0.3% when the strut is inserted, is within the experimental scatter.

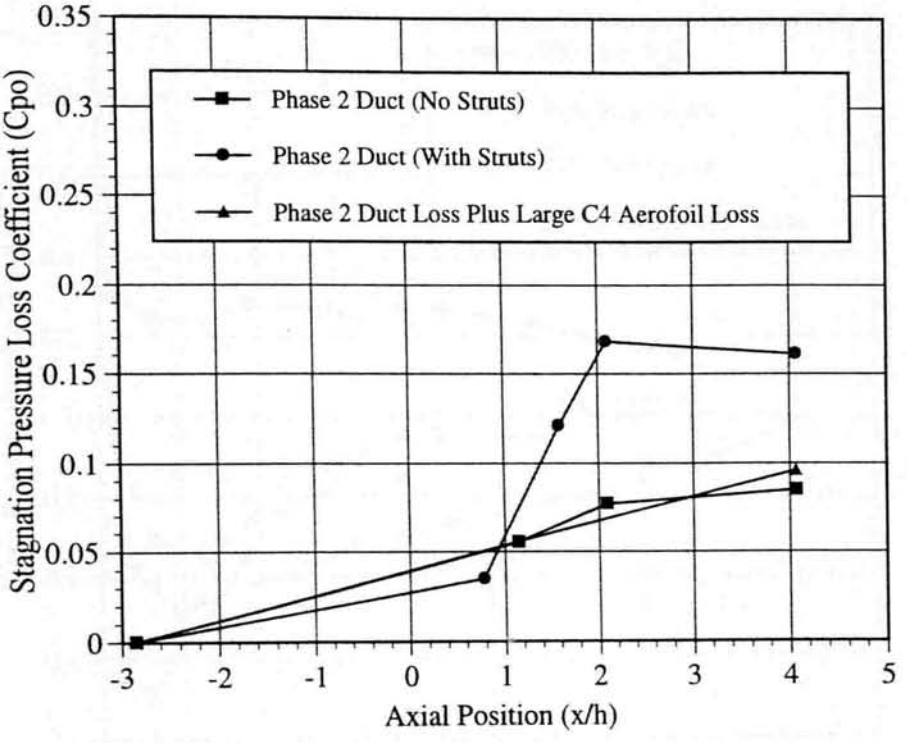

Figure 5.7 - Phase 2 Duct Cpo Development

The static pressure distributions measured at three spanwise positions across the original struts (5, 50 & 95%) are presented in figure 5.8, where 0% refers to the hub and 100% the casing. Each of the three spanwise distributions is the average of the upper and lower struts' Cp distributions for the clean inlet case (fig's 4.20 and 4.21). They are compared to the Cp distribution measured at mid span on the large C4 aerofoil in a non-diffusing duct.

The graph shows clearly that the duct diffusion is having a significant effect on the strut surface flow. At the hub (5% span), the flow on the strut surface is almost constant velocity due to the strut blockage which causes the flow to accelerate, cancelling the duct and strut diffusion. At mid span (50% span), the two distributions are of the same shape, however the duct diffusion here, shifts the duct strut distribution upwards. At the casing (95% span), the strut leading edge is situated in the accelerating duct flow, and hence here, the flow accelerates to a greater value than on the large C4 strut. Downstream of 5% Cax, the flow rapidly diffuses due to the combined duct and strut diffusion. Note for the smaller strut, the trailing edge pressure is above the zero line due to duct diffusion.

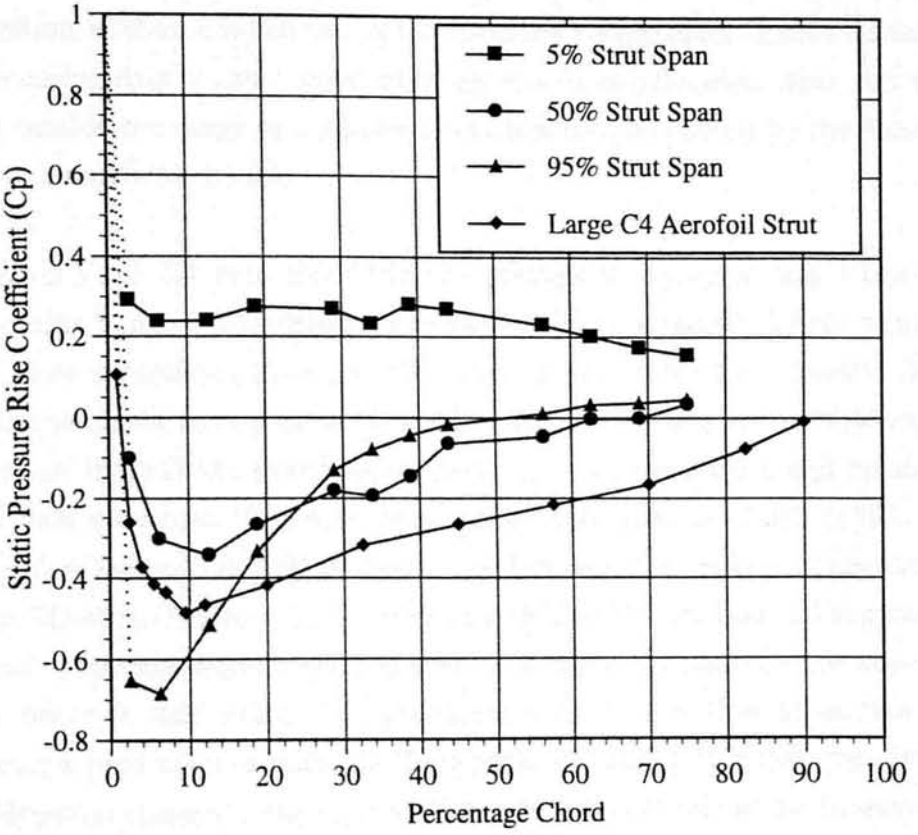

Figure 5.8 - Strut Static Pressure Distributions

Together, all of the experimental measurements and investigations carried out on the phase 2 duct suggest the presence of a three dimensional casing separation.
The summarised evidence for this is given below.

- Surface flow visualisation results shown at the beginning of chapter 4 show casing surface flow patterns akin to those produced by flow separation. These patterns occurred even without struts or IGV's present, however, a more regular structure was observed when struts were present.

- Separation bubbles are a cause of total pressure loss due to the dissipation of energy in large eddies. The experimental results show that the casing boundary layer between the two bends, contributes significantly to the overall duct total pressure loss, e.g. figure 4.75 & 4.76.

- Separation bubbles contain low axial velocities within them. Experimental 3 hole probe casing data at slot 1 show relatively low axial velocities. Also, this data was often outside the range of calibration which would be caused by the recirculating flow of a separation bubble.

- Figures 5.3 and 5.4 show that CFD over predicts the value of peak suction on the first casing bend, -1.25 predicted compared to -0.9 measured, for the strutted duct case. Flow separation (which the CFD does not predict for the unstrutted duct case) would change the aerodynamic shape of the duct locally and hence could explain the difference in CFD and experimental peak velocities since there will be changes in local duct curvature. This hypothesis agrees with Harloff *et al's* (1992) findings where they studied the flow in both a non-diffusing, non separating circular S-duct, and a diffusing (Ae/Ai = 1.51), separating circular S-shaped duct. Their predictions of static pressures were in good agreement with the measured for the non-diffusing case, however they wrote "The inaccurate prediction of flow separation leads to inaccurate prediction of static pressures in the separating duct flow case because of aerodynamic changes". Their code (PARC3D, 3-D N-S solver) did however predict flow separation, but the problem was more a flow separation positioning problem as opposed to a failure to predict flow separation at all, as was the case for the author's unstrutted duct predictions.

When the struts are in situ in the duct, figures 4.7 and 4.8 show there is certainly flow separation in the vicinity of the strut casing interface. The flow patterns on the casing, appear to form a traditional horse shoe vortex around the strut leading edge. This flow seems to form two distinct bubbles either side of the strut starting at approximately 20% Cax and continuing to about 70% Cax. These bubbles account for the flow patterns observed in figure 4.8 on the strut surface. It is this part of the duct where diffusion rates are greatest due to the combined strut and casing diffusion, and it is also approximately the position at which the gradient of static pressure recovery changes in figure 4.15, discussed earlier.

There is also evidence for an unsteady casing flow which is summarised below.

- The unsteady casing static pressure results presented in section 4.14 of chapter 4, show there to be an unsteady component of static pressure with a Reynolds number dependent frequency, similar to the phenomenon known as vortex shedding. It was found to have the same frequency, 31.8 Hz, and same signal to noise ratio of at least an order of magnitude, at all the positions measured, x/h from 0.048 to 1.158 (the vicinity of the struts).

- Kirkham (1993), measured the boundary layer development through the phase 1 duct and found there to be a dramatic unsteadiness associated with the casing boundary layer downstream of the first bend, to which at the time he attributed to an unsteady casing separation at the inlet.

This unsteadiness is due to transitory stall as a result of too rapid diffusion, i.e. operating a diffuser too close to the Cp* line shown in figure 2.4. This flow phenomena is undesirable since it is characterised by highly pulsating flows which cause pressure fluctuations, instability in the flow and poor performance.
To avoid this undesirable flow phenomena, the designer should clearly increase the length of the diffuser in order to reduce the high diffusion rates. If this option would make the diffuser unacceptably long for a particular application, then possibly truncating the diffuser as shown in figure 2.8 may improve the diffuser performance by stabilising the casing separation into a recess which can improve the smoothness of the flow and hence reducing unsteadiness. This would involve suddenly increasing the area at approximately the position at which the flow is intermittently separating.

Chapter 6

Computational Investigation and Results

6.1 Scope of Investigation

The aim of the computational investigation was to use the experimental results presented in chapter 4 to validate the Rolls-Royce in house code M.E.F.P., the Moore Elliptic Flow Program, in order to allow new future swan neck ducts to be designed with more confidence. This part of the project was originally the responsibility and under the control of Rolls-Royce plc, however more recently, the code has been run with the phase 2 duct and new test cases at Durham University by the author.

In addition to this, another code, BTOB3D, Dawes (1987) which was already available to run on a P.C. or workstation was also used to model the ducts, the results of which may be found in Norris *et al* (1997). The two codes produced similar results and hence only limited Dawes results are included in this thesis. The bulk of the CFD results consist of M.E.F.P. predictions which are in slightly better agreement with the measured results and which also have a more flexible clearer output format.

The commercially available software package 'PHOENICS' was used to design the new inlet profile which provides the test section with a more uniform total pressure profile and more stable casing surface boundary layer as previously discussed.

6.2 Methods of Investigations

6.2.1 PHOENICS

The commercial code PHOENICS [C.H.A.M.] uses the pressure correction method and was run on an HP workstation to model the inlet. The code first assumes a pressure field across the domain and then calculates a velocity field from the momentum equation. If continuity is not conserved then the pressure field is corrected by a factor which then produces a new velocity field. This loop is continued until continuity is conserved and the solution is said to be converged. The code and grid were first validated before being used to design a new inlet. This involved modelling the original inlet and ensuring that the predicted inlet total pressure profile agreed reasonably well with that measured with a boundary layer type probe at the diffuser inlet plane -1.

Boundary Conditions and Computational Grid

Since the inlet was axisymmetric (i.e. no circumferential variation), a 2-D 'slice' with one cell thickness was sufficient to model the duct. The casing tube which exists on both the original and new inlet was modelled by PHOENICS to ensure that the turbulence grid was situated in the part of the duct with the most uniform velocity. This was necessary since the total pressure loss through the grid is proportional to the velocity of the fluid passing through it and hence affects the total pressure profile at entry to the working section. The grid was first validated by comparing the predicted and measured radial velocity profile of the previous inlet. Then, different types of ellipses were used to model the new inlet casing profile until one which in combination with the original hub profile, produced a satisfactory velocity profile both at the grid position and the inlet plane. The radial total pressure profile measured at the inlet plane with the new inlet was shown in figure 4.1, p69.

6.2.2 Dawes BTOB3D

A modified version of the Dawes blade to blade 3-D solver (BTOB3D) was used to model phase 1 and phase 2 ducts. The modification was necessary to allow for non-uniform inlet total pressure profiles to be included in the simulation. The original version of the code assumed a uniform circumferential total pressure profile, hence the code was modified to allow an array containing the measured circumferential variation to be read in and used as the inlet boundary condition. The non-uniformity occurs as a result of the inlet guide vanes which provide realistic radial inlet wakes to the duct. BTOB3D, Dawes (1987) is a steady time marching 3-D viscous code which solves the Navier-Stokes equations using a mixing length turbulence model. A typical size grid for the most difficult case (inlet wakes with struts) was 49 x 141 x 33 in the I (pitchwise), J (axial) , K (spanwise) directions and is shown in figures 6.1 and 6.2. Figure 6.1, a meridional view of the grid, shows the axial spacing of the grid and also a radial projection of the inlet J plane which shows the radial and circumferential grid spacing. The cells were concentrated at the strut leading and trailing edges as well as the hub, casing and strut surfaces in order to resolve the boundary layers. Figure 6.2 shows a radial projection of the K surface grid used in and around the struts where the flow is most rapidly changing. Note the somewhat skewed cells at the strut leading edge,

unavoidable, due to the nature of the code which makes the solution harder to predict compared to the M.E.F.P. grid shown later. Skewed cells require more approximations to be made, e.g. areas, volumes, and hence finer grids provide greater accuracy and more confidence in the solution. In particular, the H-grid used by BTOB3D, inherently has problems of skewed cells at leading and trailing edges, shown in figure 6.2.

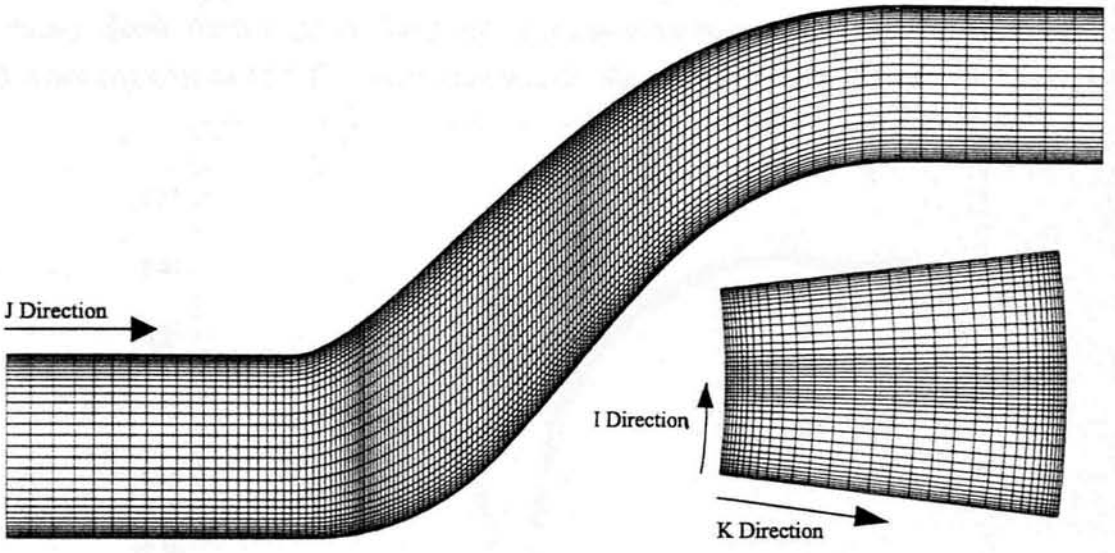

Figure 6.1 - Meridional and Axial Grids Used for BTOB3D

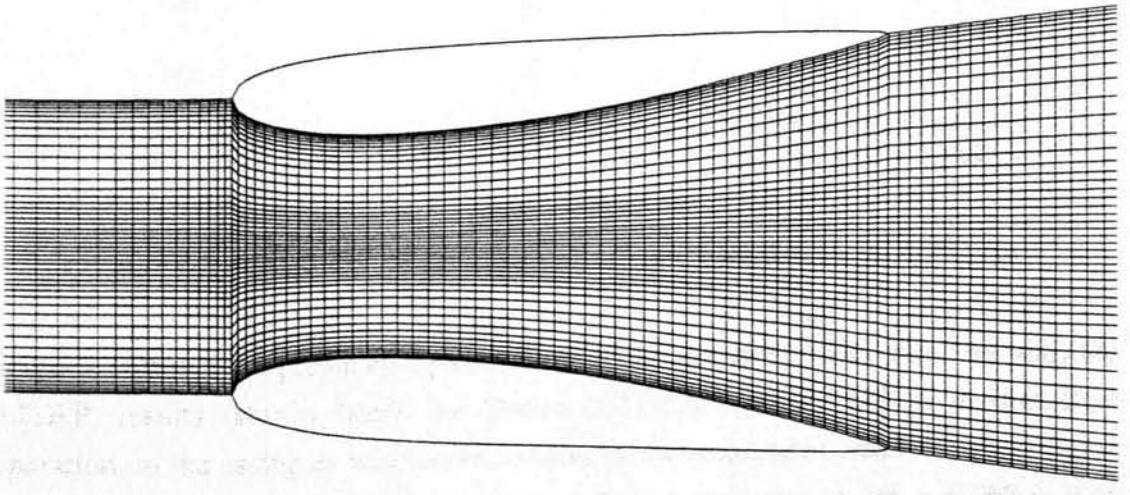

Figure 6.2 - K-Plane Grid Used for BTOB3D

This code was used as a quick and easy alternative to M.E.F.P. in order to assess briefly the effects of the inlet wakes and struts in the duct, since at the time, M.E.F.P. was not

available for use by the author at Durham. The code was deemed suitable for this purpose since it is a code widely used for turbomachinery applications.
Subsequently, M.E.F.P. along with it's much more flexible processing and output graphics package (GRAFFITI), was made available to the author, and since the primary aim of the work was to validate the Rolls Royce software using the measured experimental results, only a few computational results using BTOB3D are included in this thesis. Some further results have been published by Norris *et al* (1997). The main CFD work consists of M.E.F.P. generated results, shown later in this chapter.

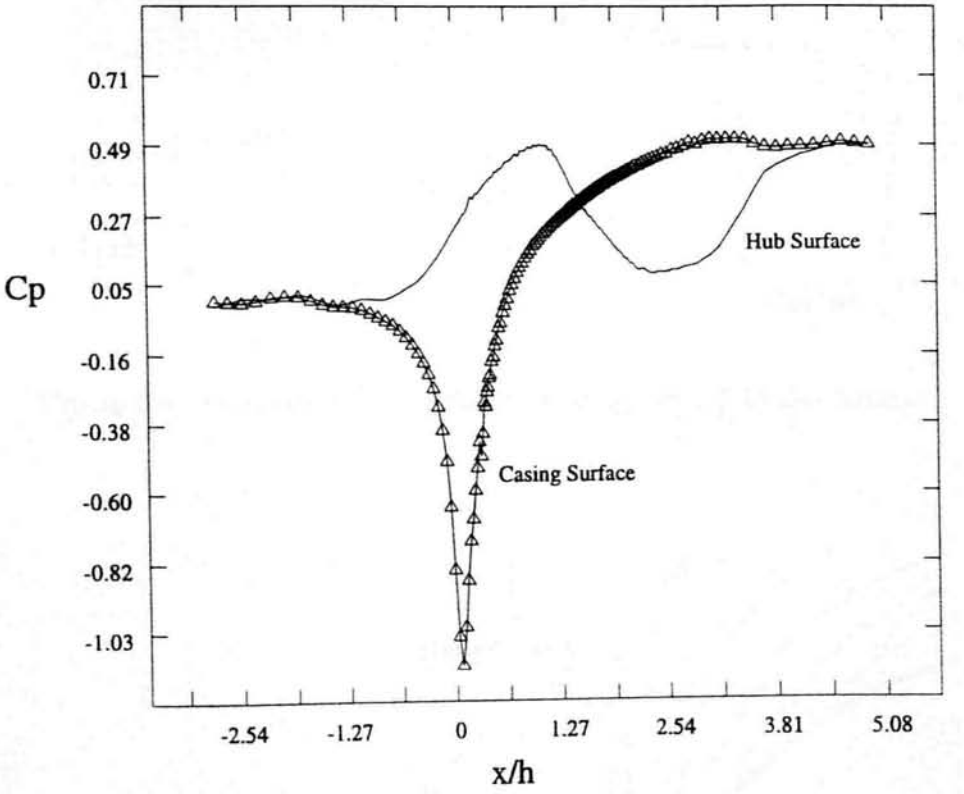

Figure 6.3 - Predicted Cp Development (Phase 2, No Struts, With IGV's)

Figure 6.3 shows the predicted Cp development for the empty duct case. As with the M.E.F.P. results (shown later), the Dawes (BTOB3D) results fail to predict flow separation on the casing as was shown to exist by the measured results shown in figure 4.14. The overall static pressure recovery coefficient measured at x/h = 4.062 is 0.46 compared to a measured value of 0.40, and an M.E.F.P. value of 0.48.
Figure 6.4, the predicted pitch angle contours nominally at slot 1 (x/h = 1.15), compare well qualitatively to the measured contours shown in figure 4.52. The predicted and

measured free stream flow angles agree with a value of approximately 42°, however, within the radial wake close to the hub where the radial flow is greatest, the CFD predicts a peak value of 59° compared to a measured peak value of approximately 54°.

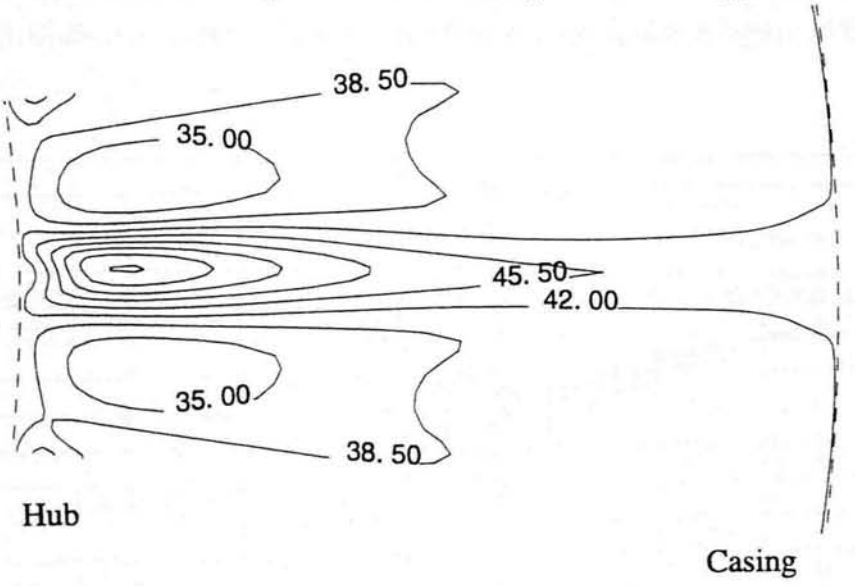

Figure 6.4 - Predicted Pitch Angle Contours at x/h = 1.15 (No Struts)

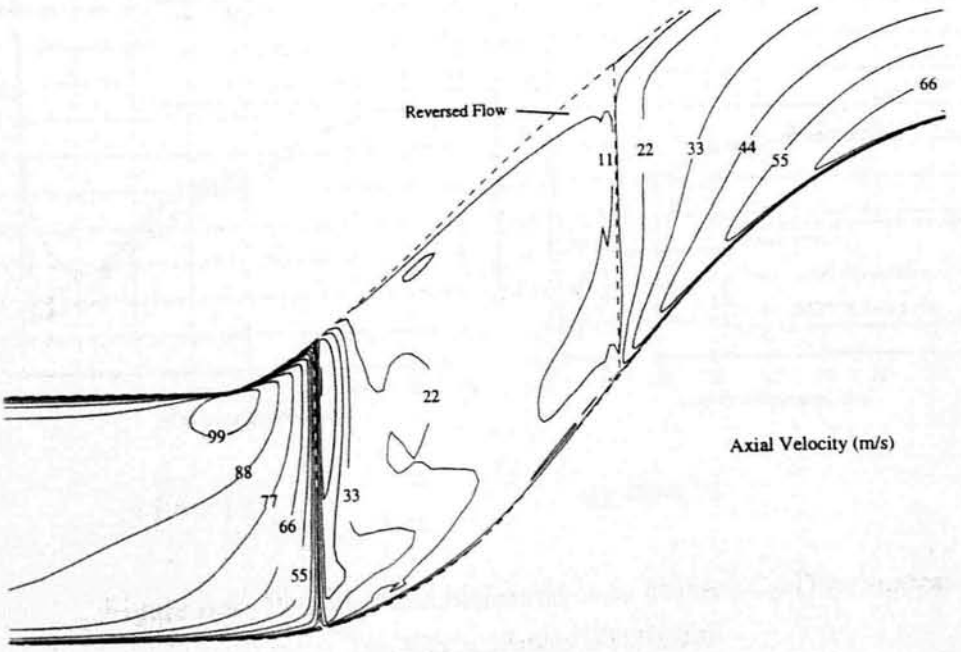

Figure 6.5 - Predicted Axial Velocity Vectors (With Struts, I = 1)

Figure 6.5 shows the predicted axial velocity vectors in the I=1 plane, i.e. it shows the strut surface flow. Although not clear to see due to the contouring levels, there is a small region of negative axial velocity (reversed flow) at the strut casing interface. This agrees at least qualitatively with the flow visualisation results shown in figures 4.8 and 4.9.

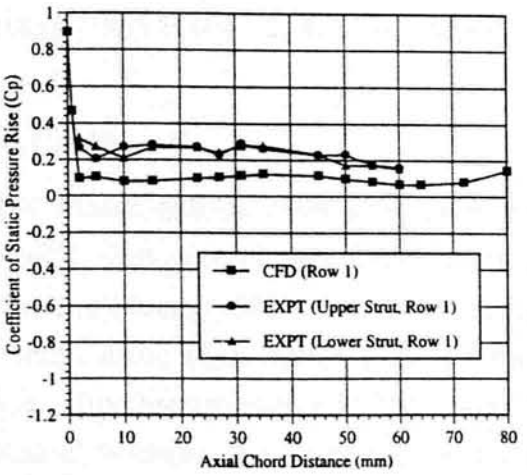

a) Row 1

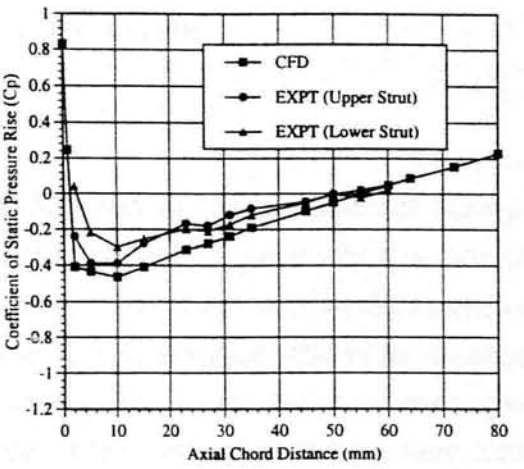

b) Row 8

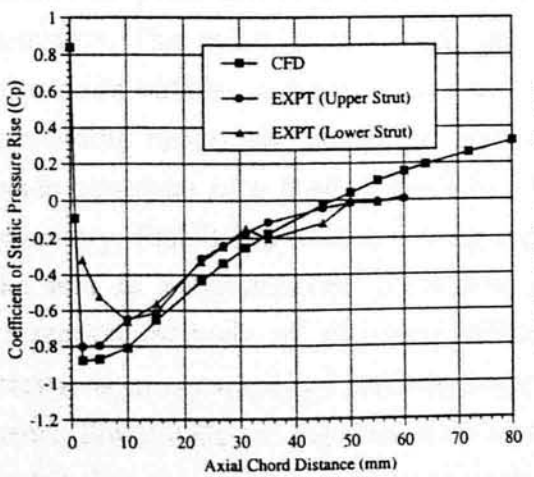

c) Row 13

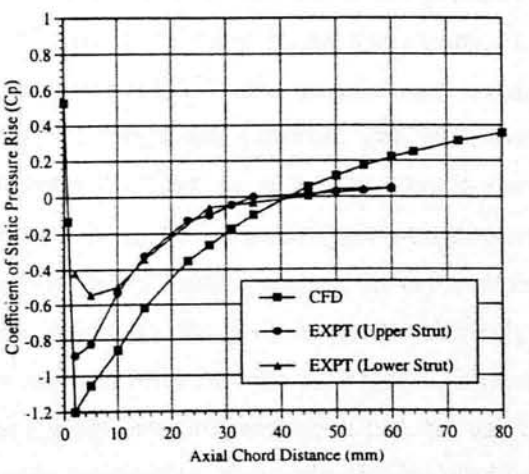

d) Row 15

Figure 6.6 - Predicted and Measured Strut Surface Cp Distributions (no IGV's, Dawes BTOB3D)

Figures 6.6a-6.6d compare quantitatively the predicted strut surface static pressures with the measured distributions at four spanwise positions. Row 1 denotes the near hub surface, row 8 mid span and row 15 the casing. The effect of the smaller predicted flow separation compared to the actual flow separation may be observed increasingly from mid span (row 8) to the casing (row 15). From approximately 30% Cax onwards, the larger measured flow separation causes the rate of diffusion to decrease towards the casing, until at row 15, the flow velocity remains constant.

6.2.3 M.E.F.P.

The Moore Elliptic Flow Program is a code based on the algorithm of Moore *et al* (1985). This is an elliptic, finite volume pressure correction code which is described in detail in Moore (1985). The continuity equation is integrated over a cell-centred control volume using linear interpolation of the velocity at each corner (grid point) to obtain the mass flux through each side. The momentum equation is then integrated over upwinded control volumes and finite difference forms of the convection and pressure terms are then obtained by central differencing of linear interpolated variables. The advantage of using an elliptic pressure correction method for this type of flow geometry, is that it allows the prediction of reverse flow across grid surfaces which are in the primary flow direction. This makes them suitable for problems containing horse shoe vortices, 2-D separation bubbles and even secondary flows when highly skewed grids are used. The upwinding nature also allows the prediction of transverse pressure gradients such as occur upstream of a bend or obstacle allowing the flow to accommodate to the new geometry. Finally the control volume approach leads to accurate mass conservation at the end of each iteration, potentially giving good total pressure results. Pressure correction methods are also very efficient since, firstly they require relatively few iterations to converge and secondly highly skewed cells are not an embarrassment and hence fewer cells are required. Also since highly non-uniform cells can be used, this makes them ideal for complex turbomachinery geometries. They can also be applied to a large range of flows from low to high Reynolds numbers. The turbulence model used was the Moore's mixing length model.

The results presented in this chapter are for the following three cases.

1. Phase 2 Duct without struts, with inlet wake

2. Phase 2 Duct with struts and inlet wake positioned at 0% strut span, i.e. axially in line with the strut leading edge.
3. Phase 2 Duct with struts and inlet wake positioned at 35% strut span.

Calculation Grid and Boundary conditions

The domain consisted of one strut pitch for all three cases and extended from the inlet plane at x/h = -2.856 to the exit plane (Slot 2) at x/h = 4.062. The same grid was used for the empty duct case, as was used for the strutted case; the solid obstacle (the strut) was turned on and off for the two solutions. The grid used for the standard strutted case is shown in figures 6.7-6.9. Figures 6.7 and 6.8 show the K-Plane mesh, i.e. a radial view, and figure 6.9 shows the J-Plane in the vicinity of the strut, i.e. a meridional view. Note from figures 6.7 and 6.8 how M.E.F.P. achieves fine orthogonal meshing in the strut boundary layers and around the strut leading and trailing edges. The grid was also concentrated towards the hub and casing surfaces in order to resolve these boundary layers. The grid consisted of 111 points axially (I direction), 41 circumferentially (J direction) and 35 radially (K direction). The inlet wake along with the hub and casing boundary layers were defined from the inlet experimental traverse.

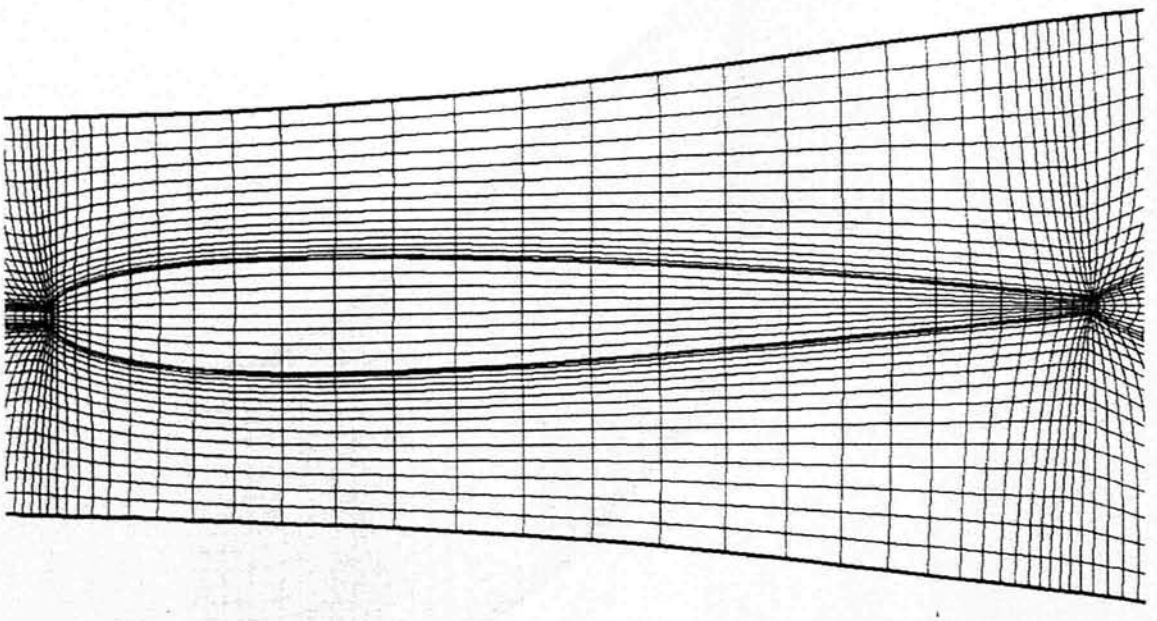

Figure 6.7- View of K-Plane Grid around the Strut

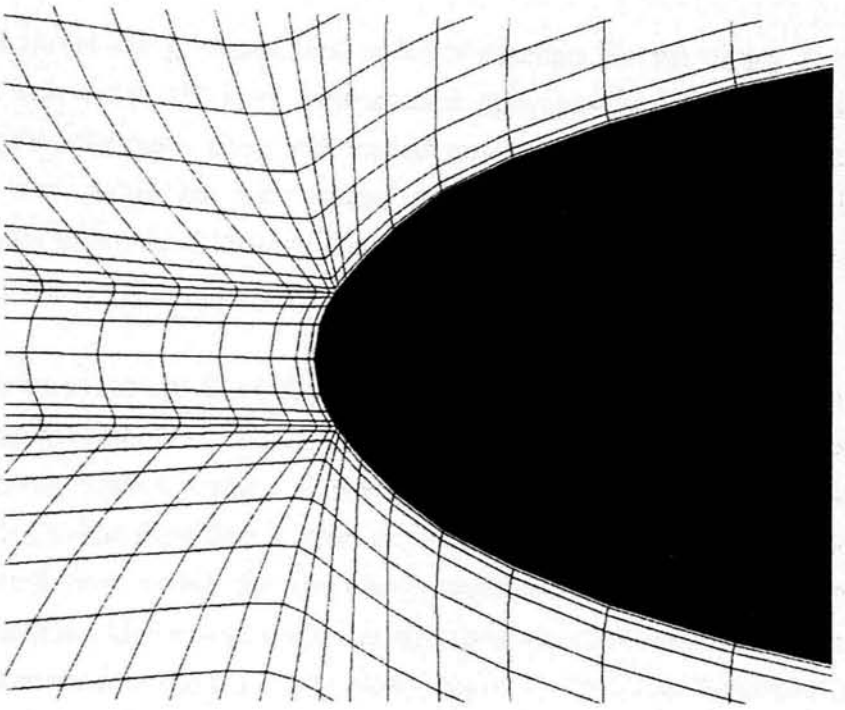

Figure 6.8 - Strut Leading Edge K-Plane Grid

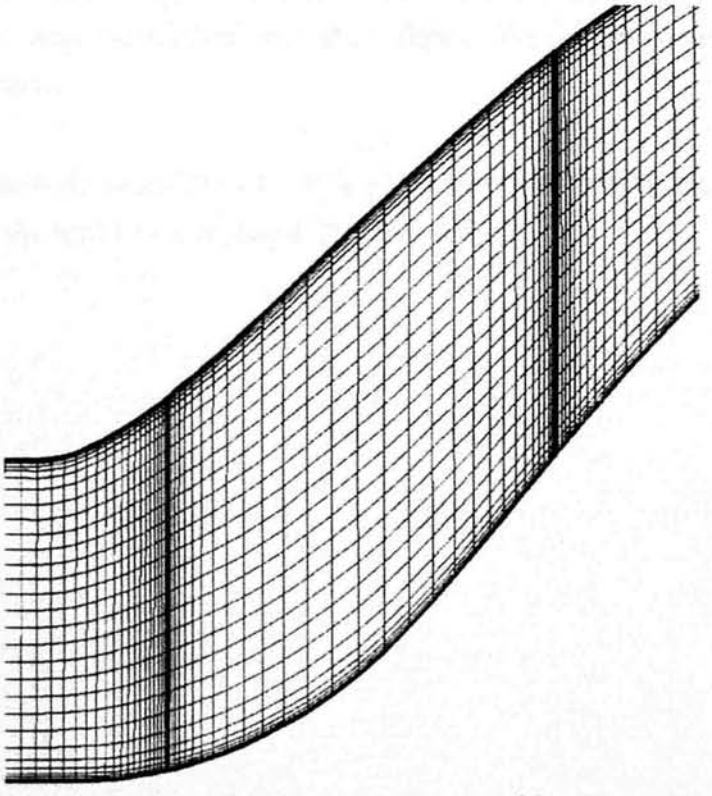

Figure 6.9 - Strut J-Plane Grid

Figure 6.10 shows the predicted total pressure contours for the empty duct case. The inlet wake, taken directly from experimental data, positioned at mid pitch, can be observed at the inlet plane along with the hub and casing boundary layers. At the second plane, half way along the inlet section, the hub and casing boundary layers have developed and grown in thickness. The inlet wake has decayed in intensity as it mixes with the free stream in the pitchwise direction.

At plane 3, immediately downstream of the first bend, the casing boundary appears similar to the second plane, and may even be thinner. This is due to the acceleration of the flow on the convex surface. Conversely, the hub boundary layer has significantly thickened due to the flow deceleration on the concave surface. There are also signs of radial outward flow within the low energy wake close to the hub due to the radial pressure gradient. At the next plane the hub flow has continued to thicken due to the further deceleration of the flow. The casing boundary layer has significantly thickened and deepened due to the now rapidly decelerating flow.

Plane 5 shows the radial transportation of the hub boundary layer within the inlet wake, due to the now well established secondary flows. The casing boundary layer has continued to thicken.

Planes 6 and 7 show the established secondary flows are now pulling the low loss casing fluid away from the surface either side of the inlet wake.

Table 6.1 shows that the overall static pressure recovery for the two IGV positions are almost the same.

	Cp	ε
No Struts	0.478	86%
Struts (IGV = 0%)	0.377	68%
Struts (IGV = 35%)	0.369	66%

Table 6.1 - Predicted Phase 2 Duct Static Pressure Recovery Coefficient

Figure 6.22 shows the predicted total pressure loss development through the phase 2 duct. Without struts where the code does not predict flow separation, the loss development is fairly linear throughout the duct. When the struts are added to the duct, the development within the inlet section is almost identical, as expected, to the unstrutted case. The separated flow due to the addition of the struts increases the loss significantly after the first bend and all the way to the exit plane. The overall predicted duct loss without struts is 5.3% of inlet dynamic head whereas with struts the loss is predicted to be 12.2% with either of the two IGV positions.

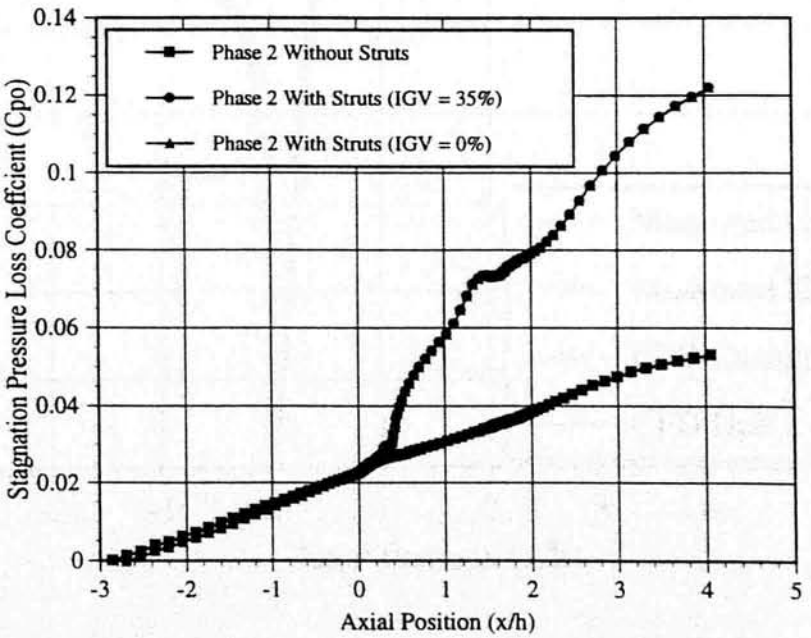

Figure 6.22 - Predicted Phase 2 Duct Cpo Development

Figure 7.1 plots the predicted and measured static pressure development through the duct for the empty duct case. The casing acceleration and hub diffusion are both over predicted immediately downstream of the first bend (x/h = 0), due to the code's failure to predict flow separation and hence change the effective local duct geometry. The measured flow reattaches and diffuses between x/h = 0.2 and 0.5 before fully separating at x/h = 0.5, which is shown by the change in gradient. In contrast, the predicted casing flow remains attached, and therefore continues to recover static pressure at a greater rate until a peak of 0.55 at x/h = 3. The separated casing flow not only affects the casing surface static pressure but due to the reduced effective area, the actual hub flow accelerates more rapidly in the latter part of the duct around the second convex bend, falling to a Cp = 0 compared to a predicted Cp = 0.2. This is clearly visible in figure 7.1.
In table 5.1 of chapter five, the phase 2 duct was quoted as recovering 0.31 of the inlet dynamic head. This value was the average of the hub and casing static pressures measured at the duct exit tappings which have an x/h = 5.062. This is a strut chord longer than the CFD grid which has it is last plane at the slot 2 axial position (x/h = 4.062). Therefore, for direct comparison of the measured and predicted overall static pressure recovery, the average of the measured hub and casing static pressures at x/h = 4.078 shall be quoted.
Table 7.1 shows that the predicted static pressure recovery for the case without struts is over estimated by 20%, due to the reasons just discussed.

	Without Struts	With Struts
Predicted (CFD)	0.478	0.369
Measured	0.397	0.317

Table 7.1 - Measured and Predicted Cp Values at Slot 2 (x/h = 4.062)

When struts are added to the duct, the additional flow acceleration and subsequent diffusion is sufficiently high that M.E.F.P. predicts at least some reversed flow. This was shown in chapter 6 to emanate from the strut casing interface approximately 25% Cax where it then spread both downstream and into the free stream. Figure 7.2 shows

measured results show a slight decrease in the recovery gradient signalling that the rapid deceleration is partially offset by the strut blockage. The CFD results show a more severe effect at this position, where the flow appears to actually accelerate slightly. The experimental results show the casing surface separation to occur at x/h = 0.8 causing the flow to reduce it is rate of diffusion. M.E.F.P. however, predicts this to occur 40 mm downstream at x/h = 1.2 which possibly accounts for the slight over estimation of the peak velocity at x/h = 0. The hub flow is also better predicted than in the unstrutted case with peak diffusion at x/h = 0.3 almost equalling the measured value. However, although the shape of the diffusion curve here on is the same as the measured, there is still a discrepancy in it's magnitude, albeit smaller than before, in the latter part of the duct due to the positional error of the predicted separation. This agrees with the findings of Harloff *et al's* (1992) who wrote "The inaccurate prediction of flow separation leads to inaccurate prediction of static pressures in the separating duct flow case because of aerodynamic changes".
The overall static pressure recovery is over predicted by 16% for the case with struts which is in closer agreement with the measured compared to the unstrutted duct case.

Figure 7.3 plots the measured and predicted total pressure loss development through the duct. As expected the CFD results under predict the loss due to inaccurate prediction of flow separation. In the unstrutted case, the CFD results under predict the actual loss by 38%, due to the failure to predict flow separation at all whereas for the strutted case where the separation is predicted but in the wrong place, the error is reduced to 25%.

Confidence in the solution could be improved by employing a finer mesh which acts to reduce the skewness of cells and hence reduces errors introduced by assumptions when calculating cell areas for example.
This would have to made at the expense of computational efficiency which is already compromised due to the fully three dimensional nature of the flow.

Another source of error is due to the simple turbulence model used which will always be in error once flow separation is present. Simple mixing length and one equation turbulence models predict erroneous eddy viscosity values due to a failure in predicting the correct boundary layer or separated wake velocity profiles, Chima *et al* (1993).

More advanced turbulence models are available but it is arguable whether any turbulence model is more accurate than any other, especially in an unsteady flow or separated flow region. Steady flow solvers such as the version of M.E.F.P. code used, attempt to drive inherently unsteady flow problems into a steady solution which will be in error compared to experimental time averaged results of an unsteady flow. Since the casing flow has been measured experimentally and is known to have an element of unsteadiness, it would be more accurate to use an unsteady solver to predict the flow, especially if the period of unsteadiness is of importance.

	Without Struts	With Struts
Predicted (CFD)	0.053	0.122
Measured	0.085	0.161

Table 7.2 - Measured and Predicted Cpo Values at Slot 2 (x/h = 4.062)

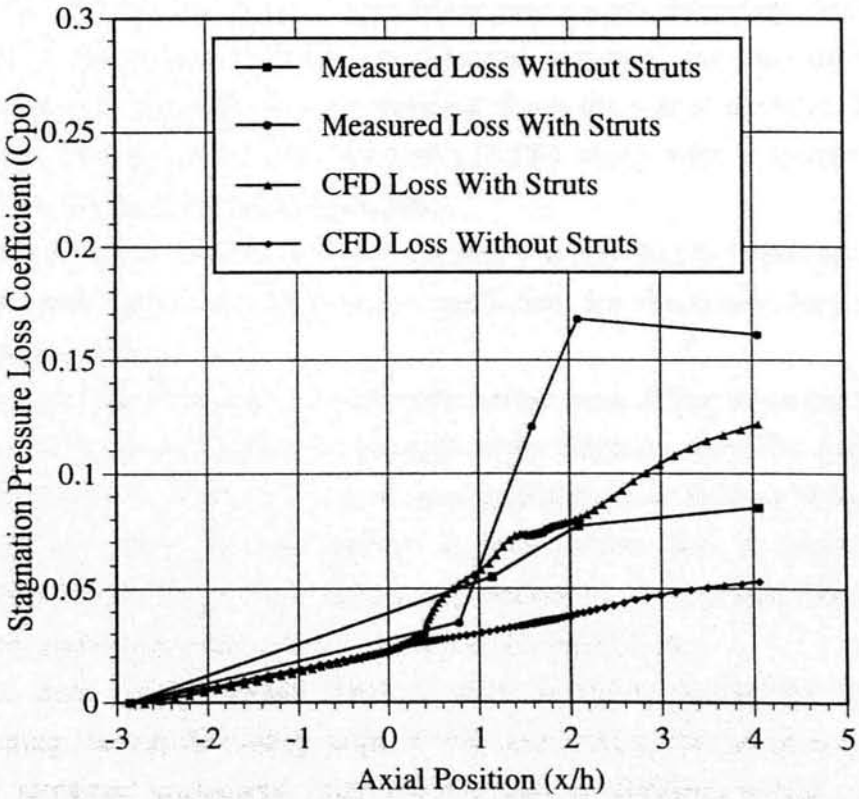

Figure 7.3 - Phase 2 Measured and Predicted Cpo Development

Chapter 8

New Strut Design

8.1 Original Design Philosophy

The phase 2 duct was originally designed without incorporating struts and hence its profile is not ideally suited for their addition. At the time of the struts' design, the only information to use as a design tool were CFD predictions and limited experimental results for the empty duct case. This meant that the effect of their addition on the local and overall duct flow was unknown. Their profile was chosen to be that of a symmetrical C4 aerofoil and their dimensions based upon existing intermediate pressure nozzle guide vanes (I.P. N.G.V's) from the RB 211 engine which are highly haded and also serve as struts and passages for services. This raised a problem that since the duct was not originally designed to accommodate struts; basing their dimensions on these haded I.P. N.G.V's, resulted in struts which had a high percentage thickness (23%). In practice, if the duct and struts were designed 'together', the duct diffusion would be adjusted to reduce the effect of the diffusion down the rear of the strut. For this reason a somewhat thinner profile was adopted (12.5%) along with a longer axial chord to exploit the length of the swan neck duct.

The exact position of the strut within the duct was also decided upon assuming the static pressure distribution and skin friction coefficient for the empty duct case. Hence the rationale was thus:

The leading edge of the strut should come before peak diffusion on the hub. This would provide blockage and relieve the strength of the diffusion. Also the trailing edge of the strut on the hub at 105 mm will be in an accelerating flow field, so there should be little tendency for either the strut surface or hub surface flow to separate. The results presented in this thesis have shown that neither of these points were likely to be a problem, especially when compared to the duct casing flow.

On the duct casing surface there is only available continuous diffusion and so positioning the strut's trailing edge at 105 mm meant that assuming the empty duct profile remained unchanged, quite modest rates of diffusion would occur on the strut surfaces. Both experimental and CFD results have shown that this not to be the case and

in hindsight, although the duct was not originally designed to accommodate struts, the chosen position of the subsequently designed struts, was probably not optimal.
The addition of the struts to the duct, not only has a pronounced and dramatic effect on the local duct flow in the region of the struts, but it also significantly changes the flow upstream of the struts. The axial position of the casing peak suction remains constant, however, the affect of strut blockage almost doubles (185%) its magnitude. This increase in velocity coupled with the strut leading edge acceleration, means that the diffusion on the casing immediately downstream of the first bend is too great for the flow to remain attached. Instead, the flow separates in a fully three dimensional manner (similar to a horse shoe vortex) and re-attaches itself to the strut casing interface at approximately 30% Cax. Evidence of this was shown by the flow visualisation results in figure 4.7.

8.2 New Strut Design Philosophy

The new design philosophy has the same aims as the original, i.e. to select the optimum position of the struts within the duct in order to minimise the overall duct total pressure loss whilst maximising the static pressure recovered. Experimental results suggest that the originally chosen position of the struts within the duct was far from optimal. This is not surprising considering the limited experimental results available for the empty duct case and no computational predictions for the case with struts, at the time of design. With the knowledge now known about both the local and overall duct flow with and without struts, the job of optimisation should be more reliable.
The new strut design is based upon CFD simulations which, although they do not predict the exact flow measured in the duct, nevertheless, do predict reversed flow for the case with struts, and hence for this case, it would seem reasonable to assume the trends of the CFD to be correct.
For the CFD predictions, which were made using M.E.F.P., the overall duct length was kept constant, and the strut chord (80 mm) and profile (symmetrical C4 aerofoil) were also left unchanged. The only variable was the axial position of the strut within the duct. Three new positions were chosen and their reasons are discussed below.

A) The first option is to try and achieve exactly what the original was designed to do. To achieve this, the strut needs to be moved upstream by 15 mm (see figure 8.1) to an x/h = 0.16 so that the strut leading edge acceleration which occurs for the first 10% Cax (8mm), counteracts the extreme duct diffusion.

B) The second option is to move the strut 95 mm (see figure 8.5) upstream of the first bend to an x/h = -1.11. In this position the strut leading edge acceleration occurs ahead of the duct surface acceleration and the strut surface diffusion can be used to reduce the duct surface acceleration. This position will generate a greater strut surface loss due to friction since the strut will be situated in a slightly higher velocity flow, however, this will be a relatively small increase.

C) The final option is to move the strut downstream by 60 mm (strut leading edge is at x/h = 1.35) so that the duct acceleration and diffusion are unaffected by the presence of the struts (see figure 8.9). In this position, the strut leading edge acceleration and subsequent diffusion would not worsen the already rapidly diffusing casing diffusion. The strut would be in a position of lower average velocity and hence lower total pressure would be lost due to the strut surface frictional losses, however, this would be a relatively small affect. The disadvantage of this position is that the wake created by the strut has less distance in which to diffuse and will therefore be stronger as it enters the downstream turbine stage.

8.3 New Strut CFD Predicted Results

The three new strut positions modelled using M.E.F.P. are the three cases just discussed and will be referred to as strut minus 15mm for case A, strut minus 95 mm for case B and strut plus 60 mm for case C.

8.3.1 Strut Minus 15 mm

Figure 8.1, a meridional view of the J plane grid, shows the new strut shifted upstream by 15 mm. It was hoped that in this position, the additional strut losses would be minimised due to countering out of the duct diffusion with strut leading edge acceleration. Unfortunately, since the code fails to predict accurately the position and

appears to be the worst case tried in terms of total pressure loss. The I plane total pressure contours for the critical part of the duct are shown in figure 8.2. The development of total pressure is similar to that of the original strut position with the separation suppressed on the far side of the strut due to the inlet wake, and a low total pressure core developing on the near side strut casing interface due to the high rates of diffusion and hence flow separation. From the scale in figure 8.3 and the velocity vector plot of figure 8.4 it can be concluded that the predicted casing separation is worse for this strut position compared to the original. This will be shown later quantitatively in the form of a duct total pressure loss graph.

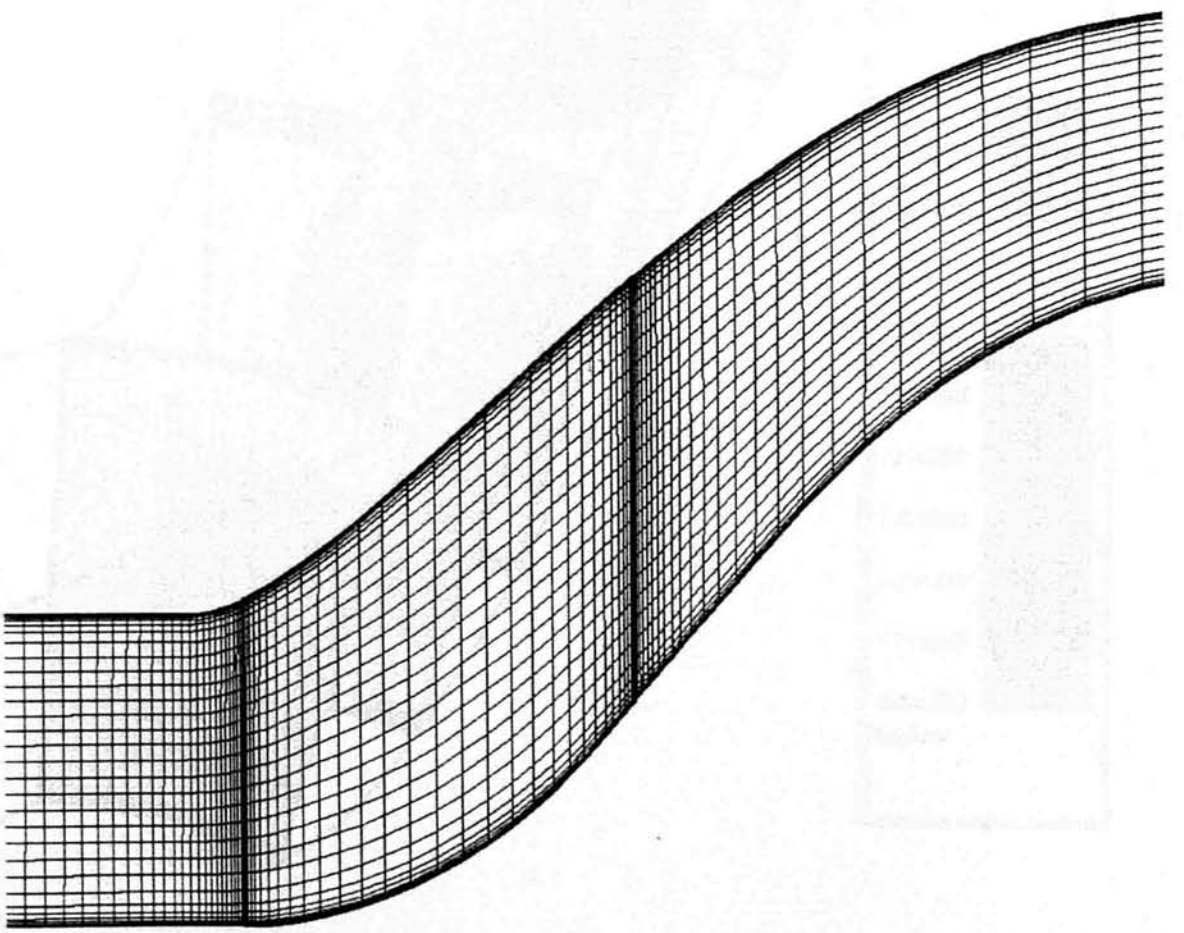

Figure 8.1 - J Plane Grid, Strut Minus 15 mm

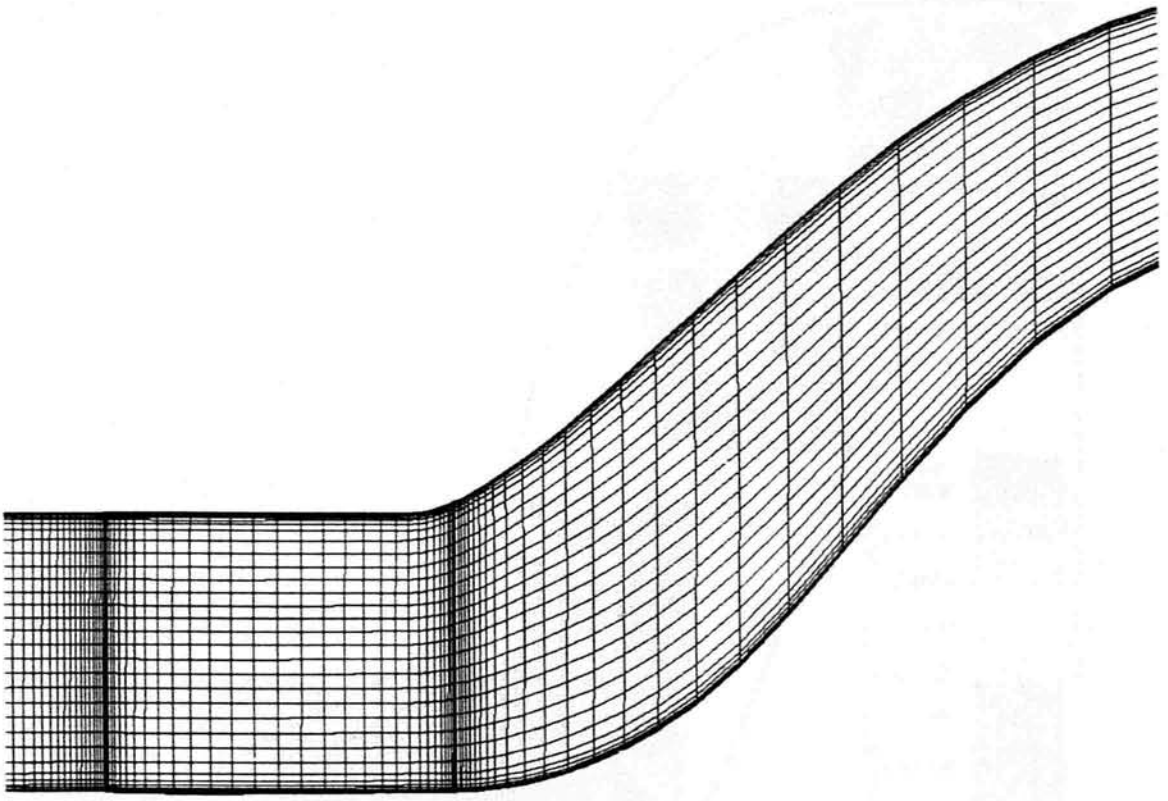

Figure 8.5 - J Plane Grid for Strut Minus 95 mm

8.3.3 Strut Plus 60 mm

Figure 8.9 shows the J plane grid when the strut is moved downstream by 60 mm. This position will later be shown quantitatively to be the best position out of the three tried in terms of total pressure loss coefficient. This is because with no strut present, the code fails to predict casing flow separation, and with the strut in this new position (i.e. shifted downstream by 60mm), the casing surface flow immediately down stream of the first bend behaves almost as if there is no strut present. Then, by the time the casing flow reaches the strut, the diffusion rate has reduced to a level at which the addition of the strut diffusion causes very little flow separation. This may be observed in figures 8.10 - 8.12.

For this reason, in practice, this may not be the best of the three tried strut positions, however, in view of the experimental loss results with and without struts, it seems likely that moving the strut downstream will reduce the loss, since the casing separation is significantly worsened when the struts are added at their original position.

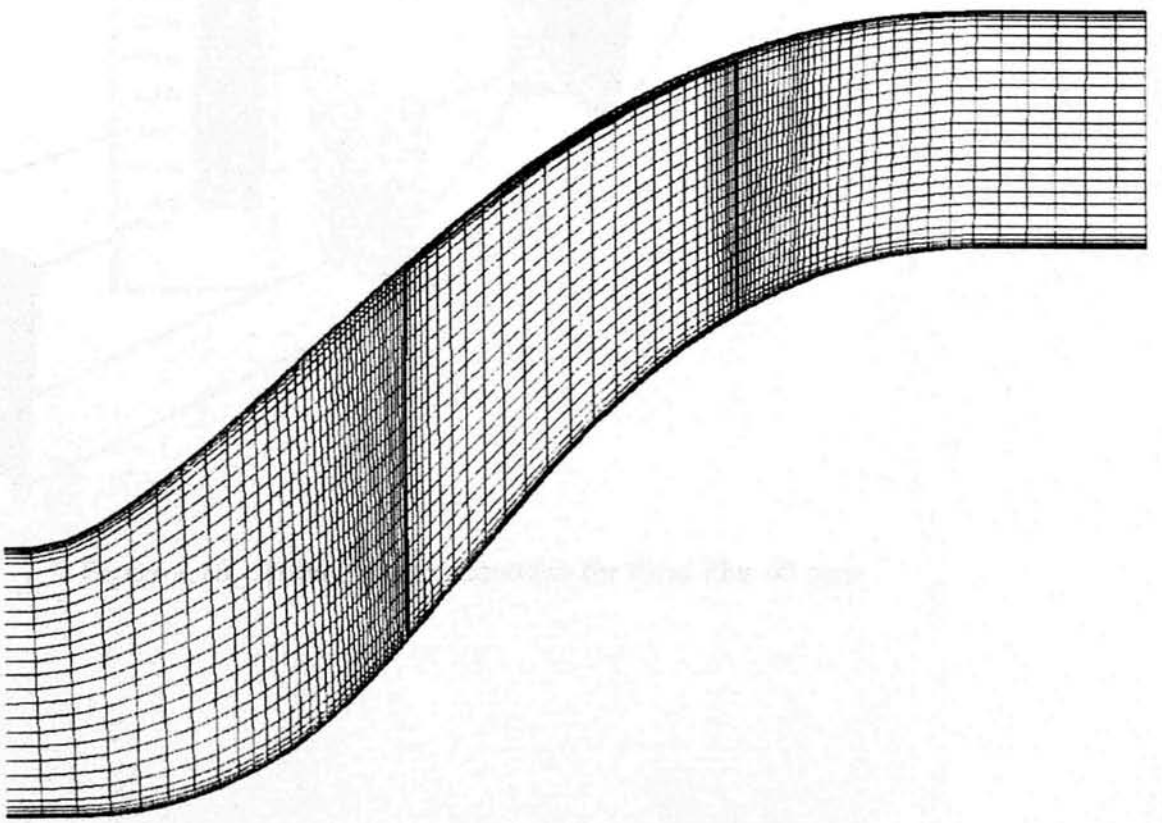

Figure 8.9 - J Plane Grid for Strut Plus 60 mm

case. Once separation occurs at approximately x/h = 1, for the minus 15 case, the flow fails to recover static pressure at the rate it does for both the measured and predicted original position cases, see figure 8.14, due to the worsened casing flow separation. The effect of the casing separation is also clearly observed on the hub flow since the effective flow area is reduced and hence the peak recovery on the hub surface is reduced from 0.45 to 0.3. This has the detrimental effect of reducing the overall Cp recovered from 0.37 to 0.23 which equates to a reduction in effectiveness from 66% to 41%.

The minus 95 case predicts an overall static pressure recovery of 0.33 (59% effectiveness) which is a 7% decrease compared to the original strut position. This is due to the flow separation which is predicted both on the near hub surface of the strut indicated by a small change in gradient at x/h = -0.4, and also on the casing surface from approximately x/h = 0.6 onwards due to the rapidly diffusing flow. The casing surface flow which is first accelerated by the strut blockage, momentarily diffuses at x/h = -0.7 before being accelerated by the convex casing bend and reaching a peak Cp value of -1.34.

The best position tried in terms of overall static pressure recovery is the plus 60 case which recovers 43% of the inlet dynamic head (77% effectiveness), an 11% increase in effectiveness compared to the original position. This is because the strut blockage relieves the casing surface diffusion in the part of the duct where flow separation would otherwise occur (x/h ≈ 1). This allows the hub surface to recover more static pressure, since the otherwise separated flow would reduce the effective area available for diffusion, shown by the higher peak in figure 8.13.

	Cp	ε
Original Position	0.37	66%
Minus 15	0.23	41%
Minus 95	0.33	59%
Plus 60	0.43	77%

Table 8.1 - Phase 2 Duct Overall Predicted Cp and ε Values for New Strut Positions

	Cp_o
Original Position	0.122
Minus 15	0.227
Minus 95	0.175
Plus 60	0.090

Table 8.2 - Phase 2 Duct Overall Predicted Cpo Values for New Strut Positions

Chapter 9

Conclusions

A comprehensive experimental and numerical study was successfully performed to investigate the flow development and structures within two annular s-shaped, inter-turbine diffusers.

Measurements of total and static pressures using 5 and 3 hole probes at various locations within the duct allowed both the performance of the two ducts, in terms of total pressure loss and static pressure recovery to be assessed as well as the flow structure in terms of secondary flow development.

These results were used to validate the Rolls-Royce CFD code M.E.F.P., which was then used to predict the performance of the phase 2 duct with the struts in 3 new axial positions.

Experimental Conclusions

Measurements taken on the phase 1 duct at varying swirl angles, shows that the total pressure loss coefficient is lowest at a swirl angle of approximately 15 degrees, at which angle, the mass averaged stagnation pressure coefficient is at least 50 % less than was measured at 0 and 30 degrees swirl angles.
At this angle however, the static pressure recovery coefficient was reduced from 0.46 at 0 degrees, to a value of 0.43. Increasing the swirl angle to 30 degrees only reduced this value to 0.42.

Measurements taken on the more severe phase 2 duct, shows the total pressure loss coefficient was reduced by 15% when IGV's were added to the duct for both cases, with and without struts. This was attributed to secondary flows within the low energy wakes, which re-energised the casing surface boundary layer, therefore reducing the size of the flow separation.

The addition of inlet wakes only changed the local static pressure distribution through the duct. The overall static pressure recovery of the two ducts was unchanged when IGV's were added. The phase 1 duct recovered 46% of the inlet dynamic head (83% effective), whereas the phase 2 duct only recovered 42% for the unstrutted case, giving an effectiveness of 76%. The strutted phase 2 duct recovered even less dynamic head, 31% (56% effective); the differences were attributed to increased diffusions causing larger separations to occur which not only reduced the overall static pressure recovered, but also increased the total pressure loss coefficient.

It can therefore be concluded from the experimental results that the diffusion rates locally within both phase 1 and phase 2 ducts and therefore also the phase 2 duct with struts, are too high for flow separation to be avoided. In particular, the radius of curvature of the first casing bend, particularly in the phase 2 duct, needs to be increased in order to reduce the magnitude of peak acceleration and hence diffusion rates immediately downstream of the bend.

Computational Conclusions

Dawes BTOB3D proved a quick and useful alternative code to M.E.F.P. in order to assess the effect of adding struts to the phase 2 duct. It predicted reasonable static pressures along the duct and strut surfaces however it failed to predict flow separation for the unstrutted case and only a small separation for the strutted case. This caused an underestimation of the predicted total pressure loss coefficient compared to the measured loss.

M.E.F.P. predicted reversed flow for the phase 2 duct with struts which manifests as a reduction in the static pressure recovered and an increase in total pressure loss coefficient compared to the unstrutted case. The code failed to predict reversed flow for the unstrutted case, however, it did predict almost stagnant flow in the region of measured flow separation. The code's failure to predict accurate flow separation was attributed to the mixing length turbulence model used and also possibly due to a too coarse mesh size. Although a finer mesh would not guarantee a more accurate flow

prediction, it would improve the confidence of the predicted solution. This was also the reason why the flow separation for the strutted case was poorly predicted both in terms of position and magnitude.

Chapter 10

Future Work

Recommendations for Future Work

Experimentally there are a number of further pieces of experimental work which should be carried out in order to gain a more comprehensive understanding of the flow in the phase 2 duct. It has been shown that the IGV wakes help suppress the casing separation when they are stationary relative to the struts. A useful but not necessarily straight forward investigation would be to add a rotating inlet wake facility.

Based upon Va/U = 0.5 and Va = 85 m/s, the rotational speed, ω, of the inlet wakes would need to be 974 rad/s (9303 rpm). With an IGV pitch = 0.18 radians and say at least 10 points needed within a pitch, an absolute minimum logging frequency would have to be 54 kHz. It is usual to log at 10 times the actual frequency to ensure all frequencies are fully captured, therefore implying a logging frequency of 540 kHz which is not impossible but would certainly be expensive, requiring highly sensitive, fast response pressure transducers.

Although the addition of a rotating upstream stage would be relatively straight forward, the instrumentation required for instantaneous unsteady measurements may need to be fully designed. This investigation would give useful information as to whether rotating inlet wakes, which are present in the real inter-turbine diffuser, actually suppress the casing suppression entirely in a severely diffusing duct such as the phase 2.

If a transitional turbulence model is to be used to predict the flow separation more accurately, such a study would have to be supported by measurements of turbulent structure of boundary layers, especially in regions of strong accelerations and diffusions.

Computationally it would be beneficial to make the mesh finer, particularly in the part of the flow which is separating. This would however compromise computational

efficiency and therefore a multi-grid strategy which time marching solvers such as the Dawes code can implement, would be the way forward. Multi-gridding uses an initial grid size which can have two or three levels of multi-gridding, e.g. can be halved and halved again to produce a coarse, medium and fine (original) grids. One such scheme performs a time step on the coarse grid, then a time step on the medium and finally one on the fine, and then back to the coarse grid to perform a second time step, and so on. Although this scheme increases cpu time due to swapping from grid to grid, compared to using only a fine grid, the overall convergence time is typically reduced to one third, since the time saving on using a coarse grid outweighs the increased swap time.

Due to the unsteady nature of the flow, an unsteady solver would provide more accurate predictions of the unsteady flow behaviour, e.g. period of unsteadiness.

Appendix A

Duct Static Tapping Locations

A1 Phase 1 Duct

Table A1.1 contains the phase 1 duct, hub and casing static tapping locations in terms of non dimensional axial position, x/h, where x is the axial distance from the datum and h, the inlet passage height (63.02mm).

Casing Tapping No.	x/h	Hub Tapping No.	x/h
1	-1.977	1	-1.977
2	-0.413	2	-0.459
3	-0.26	3	-0.341
4	-0.106	4	-0.251
5	0.039	5	-0.151
6	0.193	6	-0.07
7	0.446	7	0.039
8	0.536	8	0.156
9	0.889	9	0.247
10	0.98	10	0.898
11	1.441	11	0.989
12	1.531	12	1.423
13	1.983	13	1.513
14	2.083	14	1.956
15	2.526	15	2.363
16	2.617	16	2.825
17	3.323	17	3.25
18	3.883	18	3.756
19	4.462	19	4.308
20	4.968	20	4.923
21	5.71	21	5.565

Table A1.1 - Phase 1 Duct Static Tapping Locations

A2 Phase 2 Duct

Table A1.1 below contains the non-dimensional static tapping locations for the phase 2 duct when struts are in situ in the duct. The only difference between with and without struts is that additional tappings were later added to the duct casing in and around the strut passage to increase resolution.

Casing Tapping No.	x/h With Struts	Hub Tapping No.	x/h With Struts
1	-2.856	1	-2.856
2	-0.587	2	-0.587
3	-0.27	3	-0.27
4	-0.111	4	0.27
5	-0.071	5	0.587
6	0.048	6	1.095
7	0.182	7	1.317
8	0.206	8	1.539
9	0.286	9	1.745
10	0.333	10	1.968
11	0.436	11	2.19
12	0.563	12	2.38
13	0.682	13	2.65
14	0.793	14	2.856
15	0.912	15	3.158
16	1.031	16	3.412
17	1.158	17	3.729
18	1.254	18	4.078
19	1.381	19	4.395
20	1.619	20	4.745
21	1.968	21	5.062
22	2.253		
23	2.682		
24	2.999		
25	3.412		
26	3.729		
27	4.078		
28	4.395		
29	4.745		
30	5.062		

Table A1.1 - Phase 2 Duct Static Tapping Locations With Struts

Table A1.2 contains the non-dimensional axial locations of the phase 2 duct static tappings when struts are not present in the duct. These positions are those used in figure 4.14 for example.

Casing Tapping No.	x/h Without Struts	Hub Tapping No.	x/h Without Struts
1	-2.856	1	-2.856
2	-0.587	2	-0.587
3	-0.27	3	-0.27
4	-0.111	4	0.27
5	0.206	5	0.587
6	0.333	6	1.095
7	0.587	7	1.317
8	0.825	8	1.539
9	1.063	9	1.745
10	1.381	10	1.968
11	1.619	11	2.19
12	1.968	12	2.38
13	2.253	13	2.65
14	2.682	14	2.856
15	2.999	15	3.158
16	3.412	16	3.412
17	3.729	17	3.729
18	4.078	18	4.078
19	4.395	19	4.395
20	4.745	20	4.745
21	5.062	21	5.062

Table A1.2 - Phase 2 Duct Static Tapping Locations Without Struts

Appendix B

Strut Static Pressure Tapping Locations

The strut static pressure tappings have been labelled in terms of columns and rows as defined in figure B1 below. Tables B1-B3 contain the x and y co-ordinates of all 180 strut static tappings.

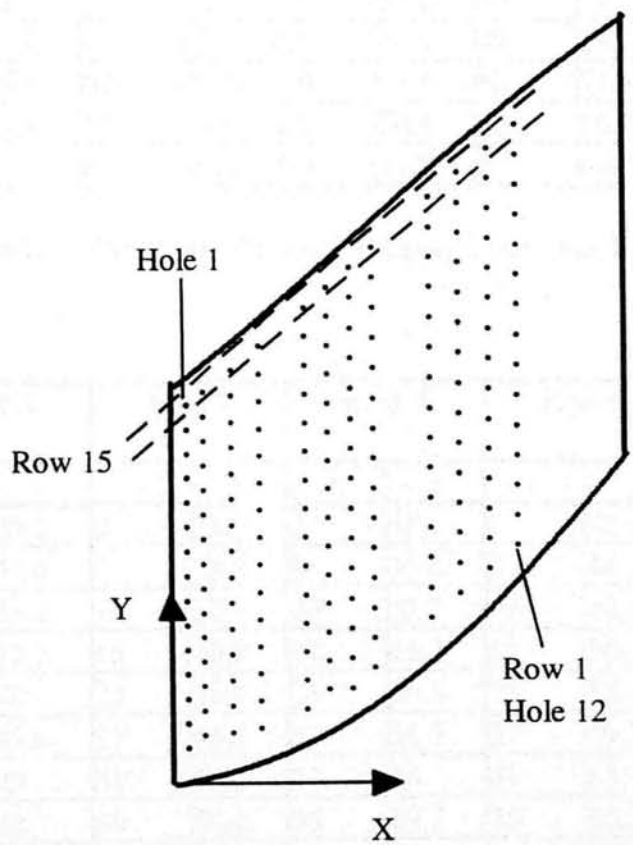

Figure B1 - Strut Static Pressure Tapping Nomenclature

	Row 1		Row 2		Row 3		Row 4		Row 5	
Hole No.	x	y	x	y	x	y	x	y	x	y
1	2	6.6	2	11.1	2	15.6	2	20.1	2	24.6
2	5	8.9	5	13.4	5	17.9	5	22.4	5	26.9
3	10	9.4	10	14.2	10	18.9	10	23.7	10	28.4
4	15	10.2	15	15.2	15	20.2	15	25.2	15	30.2
5	23	13.7	23	19	23	24.2	23	29.5	23	34.7
6	27	17.3	27	22.6	27	27.8	27	33.1	27	38.3
7	31	17.5	31	23	31	28.5	31	34	31	39.5
8	35	21.2	35	26.7	35	32.2	35	37.7	35	43.2
9	45	30.4	45	35.9	45	41.4	45	46.9	45	52.4
10	50	34.9	50	40.4	50	45.9	50	51.4	50	56.9
11	55	39.4	55	44.9	55	50.4	55	55.9	55	61.4
12	60	43.7	60	49.2	60	54.7	60	60.2	60	65.7

Table B1.1 - Strut Static Pressure Tapping Locations, Rows 1-5

	Row 6		Row 7		Row 8		Row 9		Row 10	
Hole No.	x	y	x	y	x	y	x	y	x	y
1	2	29.1	2	33.6	2	38.1	2	42.6	2	47.1
2	5	31.4	5	35.9	5	40.4	5	44.9	5	49.4
3	10	33.2	10	37.9	10	42.7	10	47.4	10	52.2
4	15	35.2	15	40.2	15	45.2	15	50.2	15	55.2
5	23	40	23	45.2	23	50.5	23	55.7	23	61
6	27	43.6	27	48.8	27	54.1	27	59.3	27	64.6
7	31	45	31	50.5	31	56	31	61.5	31	67
8	35	48.7	35	54.2	35	59.7	35	65.2	35	70.7
9	45	57.9	45	63.4	45	68.9	45	74.4	45	79.9
10	50	62.4	50	67.9	50	73.4	50	78.9	50	84.4
11	55	66.9	55	72.4	55	77.9	55	83.4	55	88.9
12	60	71.2	60	76.7	60	82.2	60	87.7	60	93.2

Table B1.2 - Strut Static Pressure Tapping Locations, Rows 6-10

	Row 11		Row 12		Row 13		Row 14		Row 15	
Hole No.	x	y	x	y	x	y	x	y	x	y
1	2	51.6	2	56.1	2	60.6	2	65.1	2	69.6
2	5	53.9	5	58.4	5	62.9	5	67.4	5	71.9
3	10	56.9	10	61.7	10	66.4	10	71.2	10	75.9
4	15	60.2	15	65.2	15	70.2	15	75.2	15	80.2
5	23	66.2	23	71.5	23	76.7	23	82	23	87.2
6	27	69.8	27	75.1	27	80.3	27	85.6	27	90.8
7	31	72.5	31	78	31	83.5	31	89	31	94.5
8	35	76.2	35	81.7	35	87.2	35	92.7	35	98.2
9	45	85.4	45	90.9	45	96.4	45	101.9	45	107.4
10	50	89.9	50	95.4	50	100.9	50	106.4	50	111.9
11	55	94.4	55	99.9	55	105.4	55	110.9	55	116.4
12	60	98.7	60	104.2	60	109.7	60	115.2	60	120.7

Table B1.3 - Strut Static Pressure Tapping Locations, Rows 11-15

References

ADENUBI, S.O.
Performance and Flow Regime of Annular Diffusers with Axial Turbomachine Dischrge Inlet Conditions
Journal of Fluids Engineering, vol. 98, series 1, no. 2, June 1976

ADKINS, R.C., WARDLE, M.H.
A Method for the Design of Optimum Annular Diffusers of Canted Configuration
ASME paper no. 90-GT-52

ADKINS, R.C., YOST, J.O.
A compact Diffuser System for Annular Combustors
ASME paper no. 83-GT-43

AMANN, C.A., NORDENSON, G.E., RAZINSKI, E.H.
The Turbine Interstage Diffuser
GMR-1083, SAE meeting, Montreal, Canada, June 7-11, 1971

ANDERSON, B.H., REDDY, D.R., KAPOOR, K
Study on Computing Separating Flows Within a Diffusing Inlet S-Duct
Journal of Propulsion and Power, vol. 10, no.5, 1994

AZAD, R.S., KASSAB, S.Z.
Turbulent Flow in a Conical Diffuser
Phys. Fluids A ,Vol. 1 , No. 3, pp 564-573, March 1989

BAINES, W.D., PETERSON, E.G.
An Investigation of Flow Through Screens
Iowa City, Iowa, ASME, July 1951

BAILEY, W.D., BRITCHFORD, K.M., CARROTTE, J.F., STEVENS, S.J.
Performance Assessment of an Annular S-Shaped Duct
Journal of Turbomachinery, Jan. 97, Vol. 119, pp 149-156

BAILEY, W.D., CARROTTE, J.F.
The influence of Swirl on the Flow within an Annular S-Shaped Duct
ASME, paper 96-GT-60

BARLOW, R.S., JOHNSTON, J.P.
Structure of a Turbulent Boundary Layer on a Concave Surface
Journal of Fluid Mech. vol. 191. pp 137-176, 1988

BRADSHAW, P
Effects of Streamline Curvature on Turbulent Flow
AGARDograph, AG-169, 1973

BRAG, G.M., SUK, J.K,
Arbitrary Mean Flow in Adverse Pressure Gradients
Journal of Basic Engineering, vo. 93, pp 495-500, 1971

BRIGHTON, J.A., JONES, J.B.
Fully Developed Turbulent Flow in Annuli
Journal of Basic Engineering, pp 835-844, Dec. 1964

BRITCHFORD, K.M., MANNERS, A.P., McGUIRK , J.J., STEVENS , S.J.
Blade Wake Effects On Turbulent Flow In Annular S-Shaped Ducts - Experiments and Computations
Dept. of Transport Technology, Loughborough University, UK, Abstract for paper for '2nd International Symposium on Engineering Turbulence Modelling and Measuring', 1993, Florence, Italy

BRITCHFORD, K.M., MANNERS, A.P., McGUIRK, J.J., STEVENS,S.J.
Measurement and Prediction of Flow in Annular S-Shaped Ducts
Engineering Turbulence Modelling and Experiments 2, Dept. of Transport Technology, Loughborough University, UK, 1993

BRITCHFORD, K.M., CARROTTE, J.F. STEVENS,S.J., McGUIRK, J.J.
The Development of the Mean Flow and Turbulence Structure in an Annular Diffuser
ASME, paper 94-GT-457

CHIMA, R.V., GIEL, P.W., BOYLE, R.J.
An Algebraic Turbulence Model for Three-Dimensional Viscous Flows
AIAA 93-0083, 31st Aerospace Sciences Meeting and Exhibition, Reno, NV, Jan 11-14, 1993

C.I.T. (CRANFIELD INSTITUTE OF TECHNOLOGY)
MSc. Course Lecture Notes
1993

CONCENTRATED HEAT AND MOMENTUM LTD. (C.H.A.M.)
Phoenics Reference Manual Parts A & B
C.H.A.M. TR200 A & B

COCKRELL, D.J., MARKLAND, E.
A Review of Incompressible Diffuser Flow
Aircraft Engineering, vol. 35, pp 286-292, 1963

COLADIPIETRO, R., SCHNEIDER, J.H., SRIDHAR.
Effects of Inlet Flow Conditions on the Performance of Equiangular Diffusers
Trans. CSME. vol. 3, No. 2, pp 75-82

COLEHOUR, J.L., FARQVHAR, B.W.
Inlet Vortex
Journal of Aircraft, vol. 1, No. 8, 1st Jan 1971, pp 39-43

DAWES, W.N.
Application of a Three-Dimensional Viscous Compressible Flow Solver to a High-Speed Centrifugal Compressor Rotor - Secondary Flow and Loss Generation
IMechE Conference on Turbomachinery Efficiency, Prediction and Improvement, Robinson College, University of Cambridge, paper C261/87, 1987

DEBRUGE, L.L.
The aerodynamic Significance of Fillet Geometry in Turbocompressor Blade Rows
ASME paper 80-GT-41, 1980

DE SIERVI, F., VIGUIER, H.C., GREITZER, E.M., TAN, C.S.
Mechanisms of Inlet-Vortex Formation
Journal of Fluid Mechanics, vol. 124, pp 173-207, 1982

DEVENPORT, W.J., AGARWAL, N.K., DEWITZ, M.B., SIMPSON, R.L., PODDAR, K.
Effects of a Fillet on the Flow Past a Wing-Body Junction
AIAA Journal, vol. 28, no. 11, pp 2017-2024, 1990

DOMINY, R.G., HODSON, H.P.
An Investigation of Factors Influencing the Calibration of 5-Hole Probes for 3-D Measurements
ASME paper, 92-GT-216, 1992

DOMINY, R.G., KIRKHAM, D.A.
The Influence of Blade Wakes on the Performance of Inter-Turbine Diffusers
ASME paper no. 84-GT-207, June 13th-16th, 1994

DOMINY, R.G., KIRKHAM, D.A.
The Influence of Swirl on the Performance of Inter-Turbine Diffusers
VDI BERICHTE NR. 1186, 1995

DOMINY, R.G., KIRKHAM, D.A., SMITH, A.D.
Flow Development Through Inter-Turbine Diffusers
ASME paper no. 96-GT-139, June 10th-13th 1996

DOVZHIK, S.A., KARTAVENKO, V.M.
Measurement of the Effect of Flow Swirl on the Efficiency of Annu;ar Ducts and Exhaust Nozzles of Axial Turbomachines
Fluid Mechanics-Soviet Research, vol. 4, No. 4, July-August 1975

ESDU
Introduction to Design and Performance Data for Diffusers
ESDU 76027, 1976

FOX, R.W., KLINE, S.J.
Flow Regimes in Curved Subsonic Diffusers
Journal of Basic Engineering, September 1962

GIBSON, A.H.
On the Resistance to Flow of Water Through Pipes or Passages Having Divergent Boundaries
Trans. R. Soc. Edinburgh, vol. 48, pt 1, No. 5, pp. 97-116, 1911

GILLIS, J.C., JOHNSTON, J.P.
Turbulent Boundary-Layer Flow and Structure on a Convex Wall and its Redevelopment on a Flat Wall
Journal of Fluid Mechanics, vol. 135, pp. 123-153, 1983

HILL, P.G., SCHAUB, U.W., SENOO, Y,
Turbulent Wakes in Pressure Gradient
Journal of Applied Mechanics, vol. 30, no. 1, pp 518-524, 1963

HARLOFF, G.J., SMITH, C.F., BRUNS, J.E., DeBONIS, J.R.
Navier-Stokes Analysis of Three-Dimensional S-Ducts
Journal of Aircraft, vol. 30, no. 4, 1993

HARLOFF, G.J., REICHERT, B.A., WELLBORNE, S.R.
Navier-Stokes Analysis and Experimental Comparison of Compressible Flow in a Diffusing S-Duct
AIAA Paper 92-2699

HOFFMANN, J.A., GONZALEZ, G.
Effects of Small-Scale, High Intensity Inlet Turbulence on Flow in a Two-Dimensional Diffuser
Journal of Fluids Engineering, vol. 106, pp 121-124, June 1984

HOFFMANN, P.H., MUCK. K.C., BRADSHAW, P
The Effect of Concave Surface Curvature on Turbulent Boundary Layers
Journal of Fluid Mechanics, vol. 161, pp. 371-403, 1985

HENDERSON, F.D.
The Effect of Profile and Length on the Efficiency of Pump Diffusers
TN 181, Rocket Propulsion Establishment, Westcott, UK, September 1959

HOADLEY, D., HUGHES, D.W.
Swirling Flow in an Annular Diffuser
Rep. CUED/A-Turbo/TR5, Dept Energy, Univ. Cambridge, UK, 1969

IRWIN, H.P.A.H., COOPER, K.R., GIRARD, R
Correction of Distorted Effects Caused by Tubing Systems in Measurements of Fluctuating Pressures
Journal of Industrial Aerodynamics, 5, pp 93-107, 1979

KIRKHAM, D.A.
Investigation of the Flow in a Swan Neck Duct
Univ. Durham, Internal Report, July 1993

KLINE, S.J., ABBOTT, D.E., FOX, R.W.
Optimum Design of Straight Walled Diffusers
Journal of Basic Engineering, September 1959

KLINE, S.J., MORKOVIN, M.V., SOVRAN, G. COCKRELL, D.J.
Methods, Predictions, Evaluation, and Flow structures
Proceedings, computation of turbulent boundary layers, AFOSR-IFP-Stanford conference, Stanford University, Stanford, California, 1968

KUMAR, D.S., KUMAR, K.L.
Effect of Swirl on Pressure Recovery in Annualr Diffusers
Journal of Mechanical Engineering Science, vol. 22, No. 6, pp. 305-313

LOHMANN, R.P., MARKOWSKI, S.J., BROOKMAN, E.T.
Swirling Flow Through Annular Diffusers with Conical Walls
Trans. ASME., vol 101, pp. 224-229, 1979

LOUGHNEY, C.E.
Boeing 737 Engine Gravel Protection
Journal of Aircraft, vol. 8, No. 10, pp 792-794, 1971

MASSEY, B.S.
Mechanics of Fluids
Van Nostrand Reinhold (International) Co. Ltd, Sixth edition, 1989

McDONALD, A.T., FOX, R.W.
Incompressible Flow in Conical Diffusers
International Journal of The Mechanical Sciences, Vol. 8, No. 2, Feb 1966, pp 125-139

McDONALD, A.T., FOX, R.W., Van DEWOESTINE, R.V.
Effects of Swirling Inlet Flow on Pressure Recovery in Conical Diffusers
AIAA, Journal, vol. 9, No. 10, pp.2014-2018, 1971

MOORE, J., MOORE, J.G.
Performance Evaluation of Linear Turbine Cascades using Three-Dimentional Viscous Flow Calculations
Journal of Engineering for Gas Turbines and Power, vol. 107, No. 4, pp 969-975, 1985

MOORE, J.G.
An Elliptic Calculation Procedure For 3D Viscous Flow
AGARD-LS-140, 1985

MUCK, K.C., HOFFMANN, P.H., BRADSHAW, P.
The Effect of Convex Surface Curvature on Turbulent Boundary Layers
Journal of Fluid Mechanics, vol. 161, pp. 347-369, 1985

NORRIS, G., DOMINY, R.G.
Diffusion Rate Influences on Inter-Turbine Diffusers
IMechE. Journal of Power and Energy, vol. 211, No. A3, pp 235-242, 1997

PARSONS, D.J, HIL, P.G.
Effects of Curvature on Two-Dimentional Diffuser Flow
Journal of Fluids Engineering, pg 349-360, Sept. 1973

PATANKAR, S.V., SPALDING, D.B.
Heat and Mass Transfer in Boundary Layers
Morgan Grampian, London, 1967.

SHIN, H.W., CHENG, W.K., GREITZER, E.M., TAN, C.S.
Inlet Vortex Formation due to Ambient Vorticity Intensification
AIAA Journal, vol. 24, No. 4, April 1986

SIMS-WILLIAMS, D.B., DOMINY, R.G.
Experimental Investigation into Unsteadiness and Instability in Passenger Car Aerodynamics
SAE paper no. 98B-34, SAE International Congress and Exhibition, Detroit, Feb 23-26, 1998

SMITH, A.D.
Turbine Technology Report
Rolls-Royce plc internal report TRE90149, 1991

SMITH, S.F.
A Simple Correlation of Turbine Efficiency
Journal of the Royal Aero. Society, 69, 467, 1965

SONADA, T., ARIMA, T., OANA, M
The Influence of Downstream Passage on the Flow within an Annular S-Shaped Duct
ASME paper 97-GT-83, Orlando, Florida, June 2-5, 1997

STEVENS, S.J., WILLIAMS, G.J.
The Influence of Inlet Conditions on the Performance of Annular Diffusers
Journal of Fluids Engineering, vol. 102, pp. 357-363, sept. 1980

THAYER, E.B.
Evaluation of Curved-Wall Annular Diffusers
ASME, 71-WA/FE-35, Wasington D.C., Nov. 28 - Dec. 2, 1971

TREASTER, A.L., YOCUM, A.M.
The Calibration and Application of Five-Hole Probes
ISA Transactions, vol. 18, No. 3, 1979

TYLER, R.A., WILLIAMSON, R.G.
Diffuser Performance with Distorted Inflow
Paper 11, Institute of Mechanical Engineers Symposium, Subsonic Fluid Flow Losses in Complex Passages and Ducts, Proc. Inst. Mech. Engrs., vol. 182, Pt 3D, pp. 115-125, 1967

WINTERNITZ, F.A.L., RAMSAY, W.J.
Effects of Inlet Boundary Layer on Pressure Recovery, Energy Conversion and Losses in Conical Diffusers
Journal of the Royal Aeronautical Society, vol. 61, pp 116-124, 1957

WELLBORN, S.R., REICHERT, B.A., OKIISHI, T.H.
Study of the Compresible Flow in a Diffusing S-Duct
Journal of Propulsion and Power, vol. 10, no. 5, 1994

ZIERER, T
Experimental Investigation of the Flow in Diffusers Behind an Axial Flow Compressor
ASME 93-GT-347, May 1993